NOVA SCHOOL OF SCIENCE & TECHNOLOGY

DEPARTAMENTO DE CIÊNCIAS DOS MATERIAIS

DUARTE NUNO BOTELHO DOS SANTOS

Licenciado em Ciências de Engenharia dos Materiais

DEVELOPMENT OF NEW MATERIALS FOR CO_2 CAPTURE: EVALUATION OF MATERIAL'S MORPHOLOGY

MESTRADO EM ENGENHARIA DOS MATERIAIS

Universidade NOVA de Lisboa
Novembro, 2021

DEVELOPMENT OF NEW MATERIALS FOR CO_2 CAPTURE: EVALUATION OF MATERIAL'S MORPHOLOGY

DUARTE NUNO BOTELHO DOS SANTOS

Licenciado em Ciências de Engenharia dos Materiais

Orientador: Doutora Marta Corvo, Investigadora,
NOVA School of Science and Technology, Portugal

Coorientador: Doutora Marcileia Zanatta, Investigadora,
NOVA School of Science and Technology, Portugal
& Institute of Advanced Materials,Universitat Jaume I,
Spain (current address)

Júri:

Presidente: Doutor Alexandre Velhinho, Professor Auxiliar,
NOVA School of Science and Technology

Arguente: Doutor Ricardo Chagas, Diretor Científico e Técnico,
CoLAB Food4Sustainability

Vogal: Doutora Marta Corvo, Investigadora,
NOVA School of Science and Technology

MESTRADO EM ENGENHARIA DE MATERIAIS

Universidade NOVA de Lisboa
Novembro, 2021

Development of new materials for CO_2 capture: Evaluation of material's morphology

ACKNOWLEDGMENTS

Primeiramente, gostaria de começar por agradecer à minha orientadora Doutora Marta Corvo e à minha co-orientadora Doutora Marcileia Zanatta por todo o acompanhamento contínuo, dedicação e exigência, que contribuiram para a dissertação tomasse a direção certa. Foram incansáveis. De igual modo, agradeço a todos os meus colegas de mestrado e doutoramento, também pertencentes ao projeto GREEN PILS FOR CO_2 (PTDC/QUI-QFI/31508/2017), por todo o vosso apoio e disponibilidade.

Não posso deixar de agradecer ao Doutor João Paulo Borges e ao Doutor Alexandre Velhinho que prontamente me ajudaram para que pudesse elaborar a dissertação nestes tempos de pandemia. Agradecer também ao CENIMAT|i3N, DCM e a NOVA School of Science and Technology, por me oferecerem todas as condições necessária para a realização da dissertação, bem como à Rede Nacional de Ressonância Magnética Nuclear (RNRMN) pelo acesso aos espectrómetros, parcialmente apoiados pelo Projeto PINFRA/22161/2016.

Quero agradecer ainda a todos os amigos que conheci e me acompanharam ao longo destes cinco anos de faculdade, relembrando não só todas as aventuras, mas também todos os desafios e barreiras que ultrapassámos. Por fim, gostaria de agradecer à minha família, que como sempre, estiveram presentes ao longo deste processo, facilitando todo o meu trabalho através de conselhos, sacrifícios e brincadeiras. Obrigado a todos!

“Motivation is what gets you started.
Commitment is what keeps you going."
(Jim Rohn)

ABSTRACT

Carbon dioxide (CO_2) is known as one of the major greenhouse gases responsible for the ongoing global warming, causing extreme weather patterns and natural calamities that affect today's society. During the last century, the concentration of CO_2 in the atmosphere has increased drastically, due to the growing fossil fuel utilization and industrial activities. Therefore, mitigating CO_2 emissions and the implications they bring to the ecosystems has become an emergency.

Over the last few years, carbon capture and utilization (CCU) technologies have been the focus of attention, as they represent a potential solution not just to reduce the CO_2 emissions by capturing it directly from the industrial facilities, but also to convert the captured CO_2 into other value-added products and useful substances (such as cyclic carbonates) to face the ever-growing energy supply-demand.

In the field of CCU, ionic liquids (ILs), materials that present unique properties that can be adjusted by changing the combination of cation/anion pairs, have been reported to exhibit promising results. Furthermore, the development of IL-derived materials through the introduction of functional groups (such as amines) or the integration with solid sorbents (like polymers) can address some drawbacks inherent to ILs, namely their limited CO_2 uptake capacity and production costs, resulting in materials with novel properties and optimized performance for carbon capture and conversion.

Based on this, the main goal of this work was to develop chitosan@IL-derived composites to use in CCU applications, as chitosan is an abundant natural polymer, with ease of processability and CO_2-philic groups in its structure. Hence, with the assistance of polyelectrolyte complexation and freeze-drying methodologies, porous cryogel beads based on chitosan@IL-derived composites have been produced. Several experimental parameters have been modified to assess their effect on the beads' morphology, which were characterized by techniques such as BET, FTIR, NMR, and SEM. Furthermore, the CO_2 sorption capacity of the beads, as well their catalytic activity in the cycloaddition reaction of CO_2 to styrene oxide to produce styrene carbonate were evaluated through FTIR and ^{1}H NMR, respectively. The results show that the chitosan@IL-derivatives are promising materials for CO_2 capture under environmental conditions (1 bar, 20^{o}C). Additionally, when used as a catalyst, it was possible to achieve a conversion of 72% and a selectivity >99% for the styrene carbonate in just 4h at a CO_2 pressure of 5 bar, temperature of 80^{o}C, and in the presence of TBA.Br as co-catalyst.

Keywords: Ionic Liquids, IL-derivatives, Chitosan, CO_2 Capture, Catalysis

RESUMO

O dióxido de carbono (CO_2) é um dos principais gases de efeito de estufa responsável pelo aquecimento global, provocando alterações climáticas dramáticas e desastres naturais sem precedentes que afetam a sociedade dos dias de hoje. Durante o último século, a concentração de CO_2 na atmosfera aumentou drasticamente devido ao uso crescente de combustíveis fósseis e atividades industriais. Neste sentido, mitigar as emissões de CO_2, bem como reduzir o seu impacto nos ecossistemas tornou-se uma emergência.

Nos anos recentes, as tecnologias de captura e utilização de carbono (CCU) tornaram-se o foco das atenções por representarem uma solução potencial, não só para reduzir as emissões de CO_2 através da sua captura direta da indústria, mas também para converter o CO_2 capturado noutros produtos de valor acrescentado e substâncias úteis (como carbonatos cíclicos) para enfrentar as necessidades progressivas de recursos energéticos.

Dentro do campo das CCU, os líquidos iónicos (ILs), materiais que apresentam propriedades únicas que podem ser ajustadas alterando a combinação do par catião/anião, têm vindo a demonstrar resultados promissores. Além disso, o desenvolvimento de materiais derivados de líquidos iónicos, através da introdução de grupos funcionais (como aminas) ou a integração com sorventes sólidos (como polímeros), permite ultrapassar algumas das barreiras inerentes aos ILs, nomeadamente a capacidade de captura de CO_2 e os custos associados ao processo, resultando então em materiais com novas propriedades e desempenho otimizado na captura e conversão de CO_2.

Neste contexto, o presente trabalho teve como principal objetivo desenvolver um material compósito à base de quitosano e derivados de líquidos iónicos (*chitosan@IL-derivative*), para ser utilizado nos processos de CCU, uma vez que o quitosano é um polímero abundante de origem natural, com boa processabilidade e grupos CO_2-fílicos na sua estrutura. Assim, recorrendo a metodologias como complexação polieletrolítica e liofilização, foram produzidas esferas porosas de criogeis, constituídos pelos compósitos de *chitosan@IL-derivative*. Diversos parâmetros experimentais foram variados, de modo a verificar o seu efeito na morfologia das esferas, que por sua vez foram caracterizadas por técnicas como FTIR, NMR, SEM e BET. De destacar ainda que, a capacidade de captura de CO_2 das esferas e a sua atividade catalítica na reação de cicloadição de CO_2 a óxido de estireno, para produzir carbonato de estireno, foram avaliadas através de FTIR e ^{1}H NMR, respetivamente. Os resultados obtidos demonstram que as esferas de *chitosan@IL-derivatives* são materiais promissores para a captura de CO_2 em condições ambientais (1 bar, 20^{o}C). Adicionalmente, ao serem utilizadas como catalisador permitiram alcançar uma conversão de 72% e seletividade >99% relativamente ao carbonato de estireno, em apenas 4h, a uma pressão de CO_2 de 5 bar, temperatura de 80^{o}C e na presença de TBA.Br como co-catalisador.

Palavras-chave: Líquidos Iónicos, Derivados de Líquidos Iónicos, Quitosano, Captura de CO_2, Catálise

TABLE OF CONTENTS

LIST OF FIGURES

LIST OF TABLES

LIST OF ABBREVIATIONS

$[BMIM]^+$ – 1-butyl-3-methylimidazolium
CC – Carbon Capture
CCU – Carbon Capture and Utilization
CCUS – Carbon Capture, Utilization and Storage
CHI – Chitosan
$[EMIM]^+$ – 1-ethyl-3-methylimidazolium
FTIR – Fourier-transform Infrared Spectroscopy
ILs – Ionic Liquids
IPOPs – Ionic Porous Organic Polymers
MDEA – Methyl Diethanolamine
MEA – Monoethanolamine
MIPs - Molecularly Imprinted Polymers
MOFs – Metal-Organic Frameworks
NMR – Nuclear Magnetic Resonance
PEC – Polyelectrolyte Complexation
PEs – Polyelectrolytes
Pebax 1657 – Polyether block amide
PILs – Polymeric Ionic Liquids or Poly(ionic liquids)
P[MATMA][BF_4] – Poly[2-(methacryloyloxy)ethyl trimethyl ammonium tetrafluoroborate]
PPNs – Porous Polymer Networks
P[VBBI][TF_2N] – Poly[1-(p-vinylbenzyl)-3-butylimidazolium bis(trifluoromethylsulfonyl)imide]
P[VBP][BF_4] – Poly[1-(p-vinylbenzyl) pyridinium tetrafluoroborate]
RTILs – Room Temperature Ionic Liquids
S_{BET} – Brunauer-Emmett-Teller Specific Surface Area
SEM – Scanning Electron Microscopy
TGA – Thermal Gravimetric Analysis
THMAMS- Tris(2-hidroxyethyl)methylammonium methylsulfate
TSILs – Task Specific Ionic Liquids
TBA.Br - Tetrabutylammonium Bromide

1. INTRODUCTION

1.1. The problem of carbon dioxide

It is known that global warming and climate change are mainly a consequence of the greenhouse gases such as CO_2, N_2O, and CH_4, which are trapping the heat in the Earth's atmosphere [1]. As a result of the growing fossil fuel utilization and industrial activities, the average atmospheric concentration of CO_2 has increased drastically, ranging from 172-300 ppm before the latest industrial age, to 415 ppm in 2020 [2]. It is then imperative to reduce such anthropogenic CO_2 emissions. Furthermore, due to the increasing world population, it is equally important to invest in new and renewable energy sources, which will be required to meet the associated growing energy supply-demand of societies [3].

Carbon capture and utilization (CCU), which is an emerging approach encompassing several methodologies to better manage CO_2 concentration that includes the capture and conversion into value-added products, has gained a lot of attention in the research field as it can provide a solution to both emissions control and energy-supply challenges [1]. In fact, carbon capture (CC) technologies have already started being employed in industrial facilities that tend to generate CO_2 through the combustion of fuels. The most common processes used to capture CO_2 from these sectors are pre-combustion, post-combustion, and oxy-combustion, depending on the source of CO_2 [4]. Despite that, post-combustion CC is currently the most mature process, requiring minimal retrofitting on existing facilities contrary to the other processes [5]. It involves the removal of CO_2 from flue gases produced after burning the fuel in the presence of air, which usually are at atmospheric pressure, in temperature ranges between 320–400 K, and contain low CO_2 concentration (3 –15 %). Even though flue gases present these unfavorable conditions, several methods can efficiently separate CO_2 from the post-combustion gas stream, such as absorption, adsorption, membrane separation, and cryogenic separation [6].

1.2. Absorption

Absorption is the most commonly used CO_2 separation method owing to its higher efficiency and lower cost [7]. In this process, a liquid sorbent is used to separate CO_2 from the flue gas [5]. Due to their advantages as chemical absorbents, such as high reactivity with CO_2 molecules, large CO_2 capacity, high absorption rate, high selectivity, and low viscosity, aqueous amines are the main and most efficient absorbent used for CC [2]. Monoethanolamine (MEA), and tertiary amines such as methyl diethanolamine (MDEA) are the most commonly used CO_2 absorbents among all amine groups [1]. Although they are effective, the application of amines faces some drawbacks, such as thermal and chemical stability (volatilization and

oxidative degradation of the amine), high energy required to operate the separation process, equipment corrosion, and consequent increase in production costs [7].

Recently, ionic liquids (ILs) have emerged as a potential alternative to aqueous amines solutions[8]. ILs can be defined as liquid electrolytes composed entirely of ions with typical melting points below 100°C [9] and unique properties such as negligible vapor pressure, high thermal stability, non-volatility, and recyclability [1]. Furthermore, the physical and chemical properties of ILs can be adjusted by altering the combination of cation/anion pairs, as well as by functionalizing the alkyl chains [10]. Hence, we can promote relevant properties to make ILs more suitable for CC, such as high CO_2 solvation and high CO_2 selectivity [11]. Some common cation/anion moieties found in ILs are represented in Figure 1.

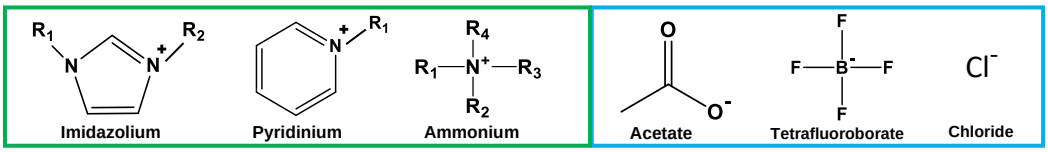

Figure 1 - Common cations (green) and anions (blue) found in ILs structures

ILs can capture CO_2 via physical or chemical absorption [12]. In physical absorption, changes of the cation/anion pair influence the CO_2 solubility. For instance, Yang et al.[13] reported that the CO_2 dissolving capacities of four representative ILs decreased as it follows: [BMIM][BF_4] > [BMIM][Cl] > [EMIM][BF_4] > [EMIM][Cl]. However, conventional ILs or room-temperature ionic liquids (RTILs) like the previous ones and several others have a low CO_2 capture capacity in comparison with amine-based solvents. To overcome this challenge task-specific ionic liquids (TSILs) have been developed. TSILs are compounds in which the anion, cation, or both covalently incorporate CO_2-philic functional groups (such as amines) as a part of the ion structure, hence promoting chemical absorption and increasing the CO_2 capture capacity of conventional ILs [9], [12]. Experimental results described elsewhere in the literature show that the carbon capture of TSILs is comparable to alkanoamines [1], [14]. Bates et al.[15] synthesized an amine-functionalized IL and observed that CO_2 reacts with the amine on the IL, and then, this intermediate reacts with another amine forming an ammonium carbamate double salt, resulting in one CO_2 molecule captured for every two IL molecules which is similar to the mechanism between organic amines and CO_2.

Even though the CC capacity is improved by the introduction of functional groups, TSILs present some drawbacks such as higher viscosity and hence slower CO_2 diffusion/absorption rate than conventional ILs. Furthermore, additional challenges like their high production costs and complicated synthesis need to be faced in order to make TSILs more suitable for industrial CC [1], [6].

1.3. **Adsorption**

Alternatively to the absorption processes, in adsorption, a solid sorbent is used to bind CO_2 on its surface. The main criteria for sorbent selection are the specific surface area, CO_2 selectivity, and regeneration ability by increasing the temperature or pressure, which allow the adsorbent to be recycled and the adsorption process to be reversible and efficient. Thus, porous solid materials offer a promising approach to capture CO_2 from the gas stream due to

their unique characteristics such as high surface area, high porosity, and versatility, being their properties and applications mainly dependent on Brunauer-Emmett-Teller Specific Surface Area (S_{BET}), pore-volume, and pore size distribution [16]. To date, several highly porous adsorbents, which operate mainly via physical adsorption, have been developed. These materials, also defined as low-temperature adsorbents, cover conventional porous materials such as zeolites, carbon-based materials, metal-organic frameworks (MOFs), and porous polymer networks (PPNs) [3], [5]. Notably, in a study conducted by Hedin et al.[17] at a partial pressure of 0.1 bar of CO_2 and temperature ranges between 273-303K, among several zeolites, MOFs, PPNs, and microporous carbons, the highest values for CO_2 sorption were obtained when using the zeolite NaX (4.0 $mmol.g^{-1}$) and Mg-MOF-74 (5.8 $mmol.g^{-1}$).

Additionally, the formation of composites from these materials with ILs or amines, which work mainly via chemical adsorption, has been reported to improve their CC capacity. As highlighted by Newhold et al.[6], ILs which have been immobilized in mesoporous silica and porous polymers attained faster adsorption at lower pressures compared to the individual solid sorbents. Kinik et al. [18] observed as well an increase in the CO_2 uptake of several MOFs after the incorporation of distinct ILs. Moreover, Mengdie et al. [19] developed several composites containing the polymer Pebax 1657 and different imidazolium-based ILs reporting an increase in CO_2 selectivity. Furthermore, amine-based adsorbents, that like ILs, commonly use silicas, MOFs, carbons, polymers, and zeolites substrates as supports, have also been reported to optimize CO_2 selectivity in comparison to the previous solid sorbents [12].

Although adsorption-based separation technologies exhibit good results in capturing CO_2, no large-scale operation has been fully deployed yet. In addition, the technologies proposed so far are not cost-effective at their current stages of development. Hence, it is still necessary to keep on studying and developing high-performance sorbents to optimize the CC process [3].

1.4. IL-based materials

As it has been reported throughout this work, the formation of IL-based materials such as TSILs or IL@solid sorbent composites can result in promising materials with novel properties and optimized performance for CO_2 absorption or adsorption. Following that line, during the last decade, polymeric ionic liquids (PILs), an innovative class of polyelectrolytes (PEs) composed of polymeric backbones with IL species in each repeating unit have gained considerable interest in CCU, due to their broad range of physicochemical properties, and the possible chemical structure designs that can be obtained using different IL monomers (such as the ones found in Figure 1) and polymeric backbones combinations. PILs not only present some of the unique polymer's features, such as easy processability, mechanical stability, and shape durability but also owing to the IL species in their repeating unit, PILs have adjustable properties that can be defined by tuning the cation/anion pair [16], [20],[21]. Additionally, despite ILs generally being liquid over a wide temperature range, most PILs are amorphous solids or gel-like materials, typically with low glass transition temperatures [6], and hence are suitable for both CO_2 absorption and adsorption processes.

Several studies have highlighted the increased CO_2 sorption capacity of PILs when compared to their IL monomers [10] but this was first introduced by Tang et al. [22] through the examination of distinct PILs and ILs. For instance, the authors observed that ammonium-based PILs absorbed about seven times more CO_2 than their corresponding RTIL monomers. Furthermore, they also reported that the PILs showed a totally reversible and faster CO_2 sorption/desorption capacity compared to RTILs.

According to the literature, several factors can influence the CO_2 sorption of PILs, such as the cation, anion, backbone, and porosity [6], [22]–[28]. Special attention should be given to this latter parameter. Within the PILs class, porous PILs which cover essentially all nano-, micro-, meso-, and macropores have emerged as promising materials for gas sorption applications [29] as they possess optimized properties when compared to other porous sorbents, namely, the enhanced mechanical stability, easy processability, higher durability, and controllability over the porous structures [16]. Despite that, porous PILs CO_2 uptake is still lower than the main technologies used in adsorption (zeolites and MOFs) as highlighted by Zulficar et al.[4] and in absorption (amines) according to Yuan et al.[30]. Additionally, the application of porous PILs in industrial levels requires further investigation regarding the scale-up possibility, stability, and porosity control. Recent advances and strategies to refine and develop differentiated porous materials from PILs have mainly focused on ionic porous organic polymers (IPOPs), molecularly imprinted polymers (MIPs), and aerogels, which have been reviewed in detail by Barrulas et al. [16].

1.5. Conversion of CO_2 using IL-based materials

CO_2 is an abundant resource and a valuable energy source, presenting the advantages of being biorenewable, non-toxic, non-flammable, and having low cost [31]. Despite that, few industrial processes use it as raw material because of the large energy input required to transform it [32]. Thus, it is important and necessary to use highly reactive catalysts to carry out the reaction between the CO_2 and several materials including epoxides, hydrogen, alcohols, acetals, oxetanes, amines, and carbon-carbon unsaturated compounds to obtain products such as carbonates, formic acids, formamides, methanol, carbamic acid esters, lactones, carboxylic acids, and other value-added products [33].

In this regard, the development of an efficient catalyst to overcome the low reactivity under mild reaction conditions of the CO_2 cycloaddition with epoxides (Figure 2) is of major importance and interest due to the great applicability of the resulting cyclic carbonates, that can be used as polar aprotic solvents in the chemical industry, raw material in pharmaceutical and fine chemical production, electrolytes in secondary batteries and polymeric materials precursors [34].

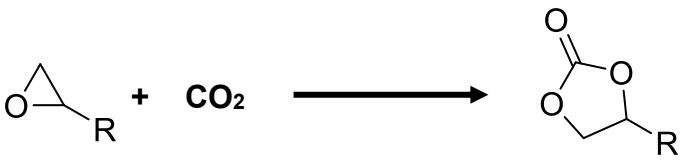

Figure 2 - Cycloaddition of CO_2 to epoxides to produce cyclic carbonates

There are two types of catalysts, homogeneous and heterogeneous, that can be distinguished by whether the catalyst occupies the same phase as the reaction mixture (typically liquid or gas) or not. Homogeneous catalysts (for example, transition metal complexes, alkali metal halides, imidazolium ionic liquids) also known as high-activity catalysts, are widely used and very efficient. However, they are hard and expensive to isolate from the reaction systems and require a high investment to be produced. On the other hand, heterogeneous catalysts, being the great majority solid (including zeolites, polymers, silicas, MOFs) which present easy product/catalyst separation, reusability, and higher stability, have emerged as an alternative to solve problems inherent to homogeneous catalysts. Despite that, they also have some disadvantages such as lower efficiency, selectivity, and the need for higher pressure/temperature conditions [6], [16], [31]. Additionally, there is a current trend to obtain heterogenized systems, where homogeneous catalysts are used with heterogeneous catalysts, to develop the ideal catalytic system that allows the reusability of catalysts, with high conversion and selectivity, together with easy isolation of the desired final product [32]–[34]. Peng et al. [35], published the first successful synthesis of cyclic carbonate using imidazolium and pyridinium RTILs as homogenous catalysis, obtaining >99% yield under optimal conditions (110 ^{o}C, 6 h, 25 bar of CO_2). From there on, several ILs have been studied as homogeneous catalysts for the cycloaddition of CO_2 [8]. Nevertheless, considering their application at industrial levels, ILs are expensive and their recycling as well product purification processes are complex. To overcome these drawbacks, ILs have been used on solid supports such as polymers, zeolites, silicas, and MOFs [36]. For instance, Martínez-Ferraté et al.[37] immobilized several ILs on commercial porous SiO_2 to efficiently produce cyclic carbonates. The best system reached 99% conversion in just 30 minutes under 80^{o} C and 5 bar of CO_2. Similarly, Taheri et al.[38] tested several ILs immobilized on chitosan through crosslinking and reported a maximum conversion of 96% with 100% selectivity (5 h, 120 ^{o}C, 20 bar of CO_2), as well as the possibility to reuse the catalyst up to five times with no losses in selectivity.

1.6. Chitosan@IL-derivatives composites

Chitosan (CHI) is a polysaccharide resulting from the deacetylation of chitin that commonly exists in the exoskeletons of crabs and shrimp shells, being one of the most abundant natural polymers. It is seen as a renewable and environmentally friendly resource and due to the presence of reactive hydroxyl and amino groups in its structure, as well as its chemical stability, versatility, and the possibility to introduce porosity, CHI is considered an interesting option for CCU [39], [40]. Additionally, its integration with ILs may create advanced functional composites exhibiting intriguing characteristics and improved performance for CCU application in comparison to the individual components [21], addressing some challenges regarding the scale-up possibility, namely their cost and control over the final structure. Therefore, it is here proposed the development of CHI@IL-derivates microporous gel beads prepared by polyelectrolyte complexation and freeze-drying, which are explained further. The variation of several synthesis parameters offers a guideline that assists researchers and engineers to understand how these factors affect the beads' morphology, and consequently the impact it has on the CO_2 capture and catalysis processes.

2. MATERIALS AND METHODS

2.1. Materials and reagents

Chitosan (degree of deacetylation 76%, low molecular weight, Lot #STBH7664), Sodium Polyacrylate (SPA) (45 wt% in H_2O, Lot #MKCL9199), Tris(2-hidroxyethyl)methylammonium methylsulfate (THMAMS) (≥95.0%, Lot #STBJ9066), Styrene Oxide (97.0%, Lot #MKCG4166), Glutaraldehyde (GLU) (50% in H_2O) were obtained from Sigma Aldrich. Acetic Acid (≥99.8%, Lot No.K2740) was obtained from Panreac. Ethanol (96.0%) was obtained from Honeywell. chloroform-*d* and deuterium oxide were obtained from Eurisotop, Carbon Dioxide (CO_2) (>99.9%), and liquid Nitrogen (>99.9%) were obtained from Air Liquide. Triethanolamine (TEA) (Lot: 1D009896) was obtained from BioChem. *Tert*-butanol (CAS# 75-65-0) from Merck Schuchardt. Tetrabutylammonium Bromide (TBA.Br) (>99.0%, Lot. SJQQI-NF) was obtained from Tokyo Chemical Industry (TCI). Whenever water was used, Millipore water was always employed.

2.2. Equipment

For the production of beads the chitosan solutions were introduced in a 20 mL syringe with an inside diameter of 19.05 mm, and a tip external diameter of 4 mm, and dropped into the sodium polyacrylate bath using a programmable syringe pump NE-1000. The pH of the solutions was controlled using an LLG Universal indicator paper pH 1-14. Beads' lyophilization was performed in a freeze-drier Zirbus VaCo 2-E.

The characterization tests were done as follows: The diameter of the beads was measured using the Image J Software (v1.53e). Scanning electron microscope (SEM) analysis were outsourced to CENIMAT | i3N at NOVA School of Science and Technology to evaluate beads' morphology. SEM images of the cryogel beads were obtained using a Carl Zeiss Auriga cross-beam (SEM–focus-ion-beam) workstation instrument. The samples were previously sputter-coated (Q150T ES Quorum sputter coater) with a thin layer of iridium to improve the contrast. The Braunauer–Emmett–Teller (BET) surface area analysis by N_2 sorption at 77.35 K was outsourced to the Analytical Laboratory of the Chemistry Department at NOVA School of Science and Technology, using a Gas Porosimeter Micromeritics ASAP 2010 (Accelerated Surface Area and Porosimetry System) to evaluate the textural properties of the synthesized beads. Fourier Transform Infrared (FTIR) spectrometry assisted by an attenuated total reflectance (ATR) accessory was performed at room temperature using a Perkin-Elmer Spectrum Two spectrometer, to analyze the beads and crosslinkers' structure. The FTIR-ATR spectra were acquired using 16 scans per spectrum, from 4000 to 400 cm^{-1}. NMR analysis ^{1}H-NMR and ^{13}C-NMR were obtained using a Bruker Avance III spectrometer, operating at a frequency of 400.15 MHz and 100.61 MHz for hydrogen and carbon, respectively, using deuterium oxide and chloroform-*d* as solvents. The spectra were analyzed with the assistance of the Top Spin

4.1.1 Software to evaluate the crosslinkers' structures and the beads' catalytic activity. For the catalysis test at a non-ambient pressure, a 22 mL Parr 4700 General Purpose Pressure Vessel homogeneous reactor was used.

2.3. Experimental Procedure

2.3.1. Synthesis of the crosslinkers

2.3.1.1. Triethanolammonium acetate (TEA.OAc)

An equimolar amount of triethanolamine (1.03 g, 6.9 mmol) and acetic acid (395 µL, 6.9 mmol) were initially introduced in a 100 mL round bottom flask. Subsequently, 20 mL of methanol were added, and the mixture was then refluxed with constant stirring (450 rpm), at 75 °C for 1 h. After this period, methanol was evaporated under vacuum pressure using a rotary evaporator, and the resulting product was vacuum dried at 55 °C. The yield of this synthesis was 71%.

The structural characterization of synthesized TEA.OAc was performed using FTIR and NMR techniques (Figures E1, G1, and G2 of the Appendix). The FTIR spectra shows a band centered at 3101 cm^{-1} corresponding to the N-H vibration of triethanolammonium. The absorption peaks at 2850 cm^{-1} and 1393 cm^{-1} were ascribed to the CH_2 asymmetric stretching and bending vibration, respectively. The bands at 1490-1120 cm^{-1} range were assigned to C-C and C-N stretching vibrations. The absorption band at 1058 cm^{-1} was attributed to the C-O vibration and the peak at 759 cm^{-1} was ascribed to the rocking vibration of CH_2 groups. Furthermore, characteristic bands of the acetate anion also appear in the spectra. The peak at 2847 cm^{-1} was ascribed to the C-H stretching vibration. The bands at 1557 cm^{-1} and 1436 cm^{-1} were attributed to the C=O asymmetric and symmetric stretching, respectively. The absorption peak at 1340cm^{-1} might be assigned to the CH_3 deformation vibration [41]–[44].

The ^{1}H and ^{13}C NMR spectra were obtained using D_2O as solvent. In the former, the signals at 3.79 (O-CH_2) and 3.19 ppm (N-CH_2) were assigned to the CH_2 groups, and the signal at 1.81 ppm was ascribed to the -CH_3 of the acetate ion. On the other hand, in the ^{13}C NMR spectra, the signals at 55.3 ppm (N-CH_2) and 56.0 ppm (O-CH_2) were attributed to the CH_2 groups, while the signal at 181.4 ppm and 23.2 ppm were assigned to the carbonyl and CH_3 group of the acetate, respectively.

2.3.1.2. Triethanolammonium chloride (TEA.Cl)

An aqueous solution of HCl (7.37 mL, 7.37 mmol, 1.1 molar equivalent) was slowly added to 1.0 g of triethanolamine (6.7 mmol) in a 50 mL round bottom flask, in an ice-water bath, under constant stirring (100 rpm), protected from the light during the whole preparation procedure. After the addition, the reaction mixture was further stirred for 0.5 h at ambient temperature. Afterwards, the mixture was evaporated under vacuum pressure using a rotary evaporator, forming a white precipitate. The white solid was filtered, washed with ethanol, and dried under vacuum at 45 °C for 48 h. The yield of this was 78%.

The structural characterizations of synthesized TEA.Cl was performed using FTIR and NMR techniques (Figures E1, G3, and G4 of the Appendix). The band centered at 3157 cm^{-1} was assigned to the N-H vibration of triethanolammonium. The band around 3450-3200 cm^{-1} was attributed to the O-H stretching vibration of branched terminals. The absorption peaks at 2939 cm^{-1} and 1401 cm^{-1} were ascribed to the CH_2 asymmetric stretching and bending vibration, respectively. The bands at 1490-1137 cm^{1} were assigned to C-C and C-N stretching vibrations. The absorption band at 1100 cm^{-1} was attributed to the C-O vibration and the peak at 761 cm^{-1} peaks was ascribed to the rocking vibration of CH_2 groups [41], [45].

The ^{1}H and ^{13}C NMR spectra were obtained using D_2O as solvent (. In the former, the signals at 3.92 ppm (O-CH_2) and 3.45 ppm (N-CH_2) were assigned to the CH_2 groups. On the other hand, in the ^{13}C NMR spectra, the signals at 55.3 ppm (O-CH_2) and 55.0 ppm (N-CH_2) were attributed to the CH_2 groups.

2.3.2. Preparation of the solutions

2.3.2.1. CHI solutions

Chitosan solutions with two different concentrations were prepared by mixing 1.0 wt% (0.5 g) or 2.5 wt% (1.25 g) of chitosan powder in 50 mL of distilled water and 1.0 v/v% (0.47 mL) of acetic acid. The resulting solution was stirred using a magnetic stirrer at 600 rpm for 24 h to dissolve the chitosan powder and form a homogeneous aqueous solution.

In some cases, a previously prepared solution of a crosslinking agent (1.0 wt%) was added to 20 mL of the CHI solution, in 0.13 or 0.26 wt%, and mixed gently to avoid the formation of bubbles before the beginning of the polyelectrolyte complexation.

2.3.2.2. SPA solutions

Aqueous solutions of sodium polyacrylate, 1.11 and 2.22 g, were further diluted in distilled water to produce 1.0 wt% and 2.0 wt% SPA solutions, respectively.

2.3.2.3. Crosslinker solutions

Crosslinker solutions were prepared by adding 1.0 wt% of each crosslinker (GLU, THMAMS, TEA.OAc, and TEA.Cl) to distilled water, in 1 mL volumetric flasks.

2.3.3. Production of porous gel beads

The CHI solution (15 mL, 1.0 or 2.5 wt%) was transferred to a syringe and dropped into a coagulation bath of SPA solution (50 mL, 1.0 or 2.0 wt%) under constant stirring (200 rpm), using an automated syringe pump. The distance from the syringe tip to the surface of the SPA solution was kept constant (11 cm).

After the addition of the desired volume of CHI solution, the CHI beads were left in the coagulation bath at a stirring speed of 200 rpm for 4h, forming hydrogel beads due to polyelectrolyte complexation. Then, the SPA bath was changed to an alcohol-based solvent and stirred for another 4h at 200 rpm. Subsequently, the beads were left with no agitation for one day in a 50 mL falcon containing a renewed alcohol solution, forming alcohol gel beads. After

this period, for a correct freeze-drying process most of the solvent was removed by decantation and the beads were immersed in a liquid nitrogen bath to freeze for one day. Lastly, the frozen beads were dried under freeze-drier conditions for one day at -50 ºC and 1 mbar to form the desired porous cryogel beads.

To optimize the beads production methodology, three distinct generations of beads were prepared by varying several parameters according to the scheme in Figure 3.

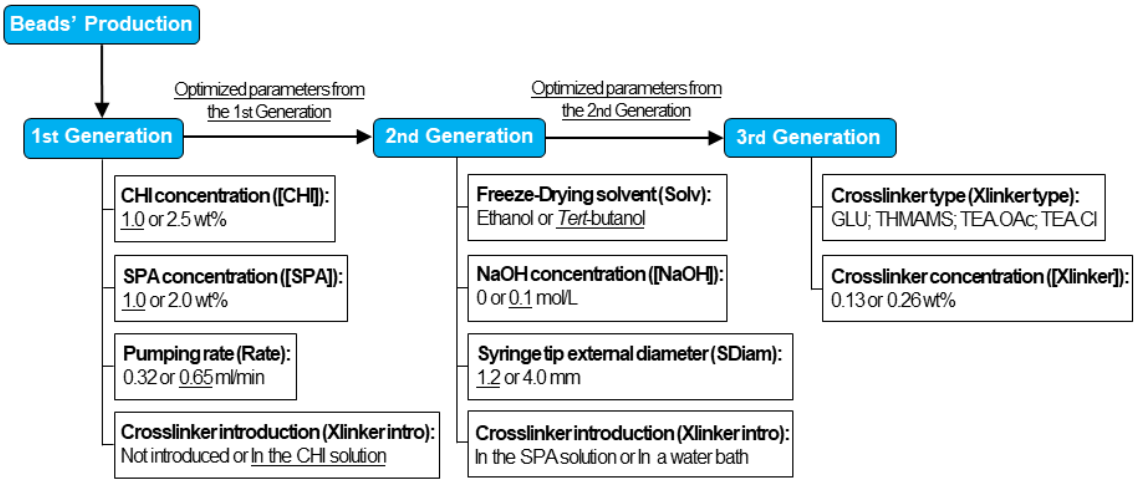

Figure 3 - Parameters tested during the beads' production

The first generation of beads was prepared to decide the best approach to produce chitosan beads. The second generation of beads was developed to optimize their stability, testing individual parameters separately and comparing the beads' shrinking. The introduction of IL-derived materials as crosslinkers in the chitosan beads was tested in the third generation, as well as their capacity to capture and convert CO_2.

2.3.4. CO_2 Capture

To test the CO_2 capture capacity of the produced beads, a flux of 77 mL/min of CO_2 was passed through 4 mg of beads in a reaction vessel for 5, 10, and 20 minutes, as depicted in the scheme of Figure 4. Afterwards, the CO_2 sorption was evaluated using FTIR spectroscopy.

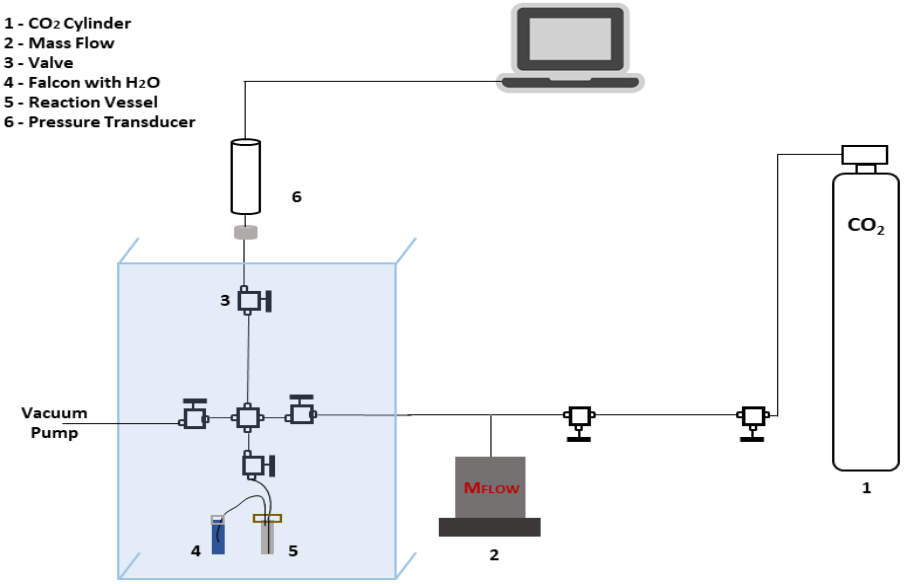

Figure 4 – CO_2 flow apparatus@i3N|CENIMAT@FCT/UNL

2.3.5. Catalysis tests

The catalytic activity of the synthesized beads in the cycloaddition reaction of CO_2 to styrene oxide to produce styrene carbonate was evaluated by varying some parameters in the presence and absence of co-catalyst (TBA.Br), as described in Figure 5. This reaction will be further discussed in section 3.8.

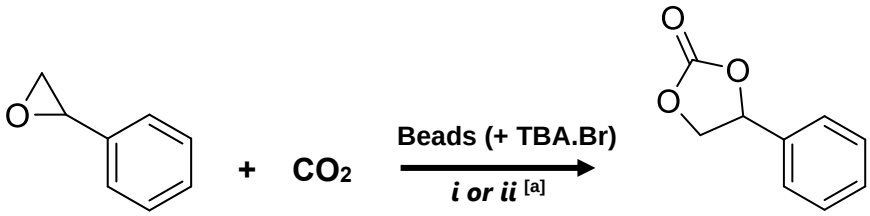

Figure 5 - CO_2 cycloaddition reaction to styrene oxide to produce styrene carbonate.
[a] Reaction conditions: *i)* 80 °C, 1 bar, 72h; *ii)* 80 °C, 5 bar, 4h

Typically, 8.3 w/w% (20 mg) of beads in the presence or absence of 26.7 w/w% (64 mg) of TBA.Br was added to a 1.92 mmol (240 mg) of styrene oxide and charged into a flask (condition *i*) or the reactor vessel (condition *ii*), depending on the desired CO_2 pressure.

For reaction condition *i*, the flask was purged three times with CO_2 to gradually evacuate the air inside the equipment. The flask was then connected to a CO_2-filled balloon to maintain a CO_2 enriched atmosphere at ambient pressure throughout the whole duration of the reaction. After setting the pressure, the reaction was stirred at 400 rpm during the pre-defined reaction time, using a magnetic stirrer with a thermoblock heated at the specified temperature. After the end of the set reaction period, the flask was air-cooled to room temperature and the resulting products were removed to be analyzed by ^{1}H NMR.

The process was similar when using the reactor vessel, reaction condition *ii*. Initially, the reactor was also purged three times with CO_2, being subsequently pressurized to 5 bar of CO_2. Thereafter, the reactor was heated to the desired temperature with an oil bath and kept at a stirring speed of 600 rpm for a designated period. After completion of the reaction predefined time, the reactor was cooled to room temperature in an ice-water bath and depressurized slowly to atmospheric pressure. Lastly, the obtained products were removed to be analyzed by ^{1}H NMR.

3. RESULTS AND DISCUSSION

3.1. General overview

Regarding the preparation strategy, the formation of beads can be divided into three major steps, as described below:

1) Preparation of the polyelectrolyte (PE) solutions – Polyelectrolytes, also known as polymeric electrolytes, are defined as polymer chains with charged monomer units that can be dissolved using a polar solvent into a solution of charged macroion and small counterions that tend to preserve the electroneutrality. Positively charged polymers are often referred to as polycations, negatively charged polymers as polyanions, and polyelectrolytes that bear both cationic and anionic repeat groups are called polyampholytes. Furthermore, polyelectrolytes can be also classified according to their strength, which is based on the charge density. The charge of weak polyelectrolytes varies with the pH, while the charge of strong ones is independent of the pH [20], [43], [44]. Additional classifications depending on the origin and matrix have been reviewed in more detail by Nikolaeva et al. [20].

In this work, chitosan (1.0 or 2.5 wt%) was dissolved in an aqueous solution of acetic acid (1.0 v/v %), becoming a cationic polyelectrolyte with a high density of positive charges [45] at low pH due to the protonation of the amines, forming quaternary ammonium groups as shown in Figure 6.

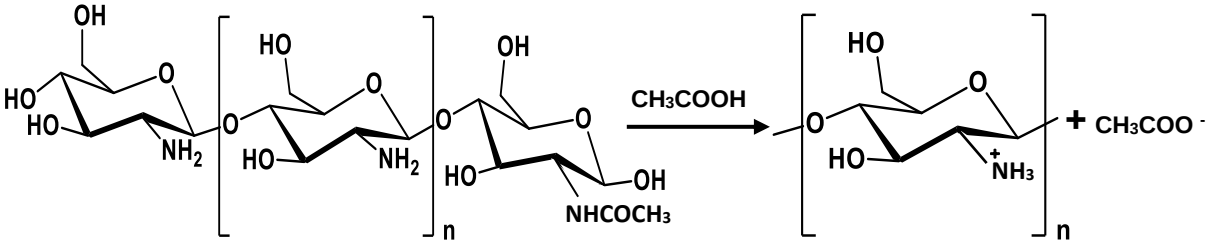

Figure 6 - Chitosan protonation with acetic acid

On the other hand, the aqueous solution of sodium polyacrylate was further diluted (1.0 and 2.0 wt%) forming an anionic polyelectrolyte with negatively charged carboxylic groups (Figure 7) at basic pH.

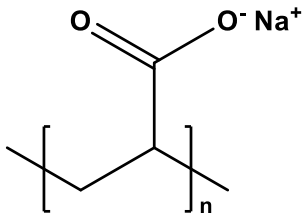

Figure 7 - Sodium polyacrylate structure

2) **Polyelectrolyte complexation –** Commonly used as a synthetic route to produce IPOPs [16], in this methodology polyelectrolyte complexes are mainly formed through cooperative electrostatic forces between polycations and polyanions mixed in aqueous solutions, and by a lowering of total Gibbs free energy. This can be explained by the fact that polyelectrolyte molecules in aqueous solution form an electrical double layer (i.e a zone with an increased concentration of counterions) surrounding them, which restricts the motion of counterions to some extent, as they remain in the vicinity of the polyelectrolyte ionic sites. However, when the complexation takes place, the negative and positive ionic groups of the opposite polyelectrolytes interact, leading to the destruction of the double layer. Therefore, the counterions are released, and consequently the entropy increases [46]. Notably, despite the occurrence of either negative or positive changes in enthalpy, leading to exothermic or endothermic processes, respectively, caused mainly by electrostatic interactions and other factors such as hydrogen bonding, van der Waals forces, dipole and hydrophobic interactions in a smaller extent, the entropy gain typically exceeds the changes in enthalpy and drives the complexation phenomena by reducing the total Gibbs free energy [47]–[49].

The stability of polyelectrolyte complexes can be affected by several factors, including the concentration of polyelectrolytes, nature, and position of the ionic groups, molecular weight, ionic strength, pH of the reaction medium, mixing ratio, and drying process [45], [49]. Additional conditions imposed by our methodology such as pumping rate and crosslinker presence were also shown to influence the complexation process and will be later discussed in more detail.

The PECs formation mechanism commonly accepted in the literature can be subdivided into three stages (as shown in Figure 8). [44], [50]

i) Primary complexes: Formed initially and almost instantly after mixing the oppositely charged PE solutions due to Coulomb's interactions.

ii) Intracomplexes: This intermediate step usually takes 1-2 h from the time of mixing, and can involve the formation of new electrostatic bonds, and/or alteration in the polymeric chains within the complex to define a new conformation that favors charge compensation.

iii) Intercomplexes: This step occurs mainly through hydrophobic interactions. The previous secondary complexes aggregate and form the final polyelectrolyte complexes, which tend to be water-insoluble. However, the complexation conditions influence the final characteristics of the aggregates obtained in this last stage.

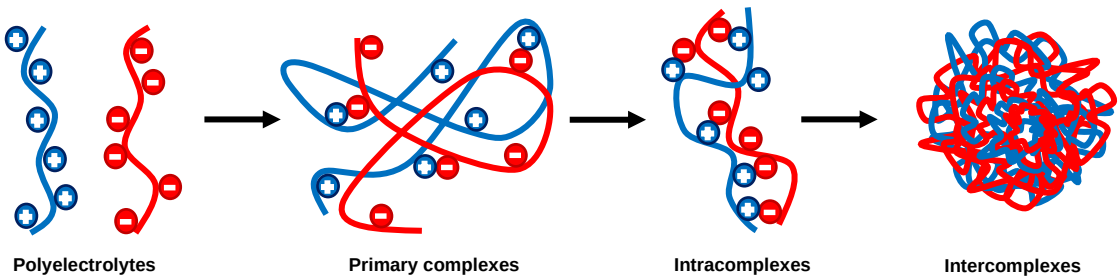

Figure 8 - Polyelectrolyte complexation stages

3) **Freeze-drying** -The initial step of this process consists of freezing our solution/gel, in a solvent that will act as a porogen, typically by immersing the suspension of the sample in a liquid nitrogen bath. During this freezing stage, solvent crystals will grow and exclude solute molecules from the frozen solvent until the sample is completely frozen. Several freezing parameters such as the freezing temperature, solute concentration, solvent type, and direction of freezing can affect the desired pore structure of the materials. The frozen sample is then placed in a freeze dryer with temperature-controlled shelves, to remove the frozen solvent by sublimation under vacuum pressure. This drying step is usually the most time-consuming and is dependent on factors such as solvent sublimation rate, sample size, level of vacuum, and shelf temperature. In some cases, secondary drying is carried out to desorb the unfrozen solvent bound to the polymer and for this process, a lower vacuum level is used [50].

3.2. Beads' production: 1st Generation

While preparing the 1.0 wt% CHI solutions these exhibited higher viscosity than the pure water solution, a transparent yellowish color, and a pH value between 3-4. When the concentration was increased to 2.5 wt% CHI, the solution became more yellow, yet transparent, the viscosity increased, as well the pH shifted to values between 4-5. No filtration or further alterations to the solutions was required.

On the other hand, both 1.0 and 2.0 wt% SPA solutions were completely homogeneous, colorless, and changes in the viscosity were insignificant. The pH intervals of the solutions were between 7-8.

When adding glutaraldehyde to the CHI solutions some bubbles could be formed if the stirring process was too intense. Bubbles should be avoided and expelled out from the syringe before the pumping starts so that they don't end up in the drop and weaken the formation of beads.

As mentioned previously, ideally the beads would go from a hydrogel to an alcohol gel, and then to a final cryogel state. However, due to the variations in the experimental parameters, the beads had different behaviors during the polyelectrolyte complexation, solvent change, and freeze-drying processes, resulting in either spherical beads or non-spherical beads. The latter included beads that partially/fully degraded and/or had a wrinkled appearance resembling a raisin as illustrated by Figure 9.

Figure 9 - Different outcomes of hydrogel beads' formation: wrinkled, partially degraded and, spherical, from the left to the right, respectively

In this 1st generation of beads, 16 experiments were performed according to the conditions described in Table 1, to set the best production parameters.

The non-spherical beads (Table 1, entry 1-8 and 12-16) did not go through a freeze-drying process, as their loss of shape and degradation could be an indicator that the complexation was compromised. On the other hand, experiments $G1_{1\text{-}1\text{-}Ø\text{-}0.65}$ (where the designation stands for "Beads' Generation (G#) and in subscript: PE concentrations([CHI]-[SPA])-Crosslinker Introduction (Xlinker Intro)-Pumping rate (Rate))", $G1_{1\text{-}1\text{-}CHI\text{-}0.65}$, and $G1_{1\text{-}2\text{-}Ø\text{-}0.65}$ (Table 1, entry 9, 10 and 11, respectively) resulted in the preferred cryogel beads, and hence are highlighted. Furthermore, it should be noted that these beads also exhibited a rigid and brittle character, as well as whitish color, after being freeze-dried.

Table 1 - 1st generation experiments

1st Generation Parameters						Results
Entry	**Experiment[a]**	**[CHI] (wt%)**	**[SPA](%wt)**	**Xlinker intro[b]**	**Rate (mL/min)**	**Bead shape**
1	$G1_{1\text{-}1\text{-}Ø\text{-}0.32}$	1.0	1.0	Ø	0.32	Non-spherical
2	$G1_{1\text{-}1\text{-}CHI\text{-}0.32}$	1.0	1.0	CHI solution	0.32	Non-spherical
3	$G1_{1\text{-}2\text{-}Ø\text{-}0.32}$	1.0	2.0	Ø	0.32	Non-spherical
4	$G1_{1\text{-}2\text{-}CHI\text{-}0.32}$	1.0	2.0	CHI solution	0.32	Non-spherical
5	$G1_{2.5\text{-}1\text{-}Ø\text{-}0.32}$	2.5	1.0	Ø	0.32	Non-spherical
6	$G1_{2.5\text{-}1\text{-}CHI\text{-}0.32}$	2.5	1.0	CHI solution	0.32	Non-spherical
7	$G1_{2.5\text{-}2\text{-}Ø\text{-}0.32}$	2.5	2.0	Ø	0.32	Non-spherical
8	$G1_{2.5\text{-}2\text{-}CHI\text{-}0.32}$	2.5	2.0	CHI solution	0.32	Non-spherical
9	**$G1_{1\text{-}1\text{-}Ø\text{-}0.65}$**	**1.0**	**1.0**	**Ø**	**0.65**	**Spherical**
10	**$G1_{1\text{-}1\text{-}CHI\text{-}0.65}$**	**1.0**	**1.0**	**CHI solution**	**0.65**	**Spherical**
11	**$G1_{1\text{-}2\text{-}Ø\text{-}0.65}$**	**1.0**	**2.0**	**Ø**	**0.65**	**Spherical**
12	$G1_{1\text{-}2\text{-}CHI\text{-}0.65}$	1.0	2.0	CHI solution	0.65	Non-spherical
13	$G1_{2.5\text{-}1\text{-}Ø\text{-}0.65}$	2.5	1.0	Ø	0.65	Non-spherical
14	$G1_{2.5\text{-}1\text{-}CHI\text{-}0.65}$	2.5	1.0	CHI solution	0.65	Non-spherical
15	$G1_{2.5\text{-}2\text{-}Ø\text{-}0.65}$	2.5	2.0	Ø	0.65	Non-spherical
16	$G1_{2.5\text{-}2\text{-}CHI\text{-}0.65}$	2.5	2.0	CHI solution	0.65	Non-spherical

[a] Experiment designation = "Beads' Generation (G#) and in subscript: PE concentrations([CHI]-[SPA]) and - Crosslinker Introduction (Xlinker Intro) -Pumping Rate (Rate)";
[b] Ø= Not introduced. When introduced [Xlinker]= 0.13 wt% of the CHI solution.

Because little is known about the mechanisms behind the formation of polyelectrolyte complexes, an approach to understanding the influence of the selected factors is of great interest and major relevance.

It was observed that 1.0 wt% CHI solutions generated drops that started to coagulate near the surface of the SPA bath. After a short period, the bead immersed in the solution due to its densification, most certainly caused by the complexation process. However, if the CHI solution was dropped in the center of the bath, a tendency for initial agglomeration of beads was noticed. To avoid that the syringe pump was placed at a specific position so that the drops would fall away from the center of agitation, describing a larger circular motion and reducing the tendency for agglomeration. Due to the increase of CHI concentration, drops with 2.5 wt%

CHI did not exhibit this problem, most likely because they were dense enough to immediately sink in the SPA bath.

The **influence of the polycation concentration** can be further observed by comparing experiments $G1_{1\text{-}1\text{-}Ø\text{-}0.65}$ and $G1_{1\text{-}1\text{-}CHI\text{-}0.65}$ with the experiments $G1_{2.5\text{-}1\text{-}Ø\text{-}0.65}$ and $G1_{2.5\text{-}1\text{-}CHI\text{-}0.65}$ (Table 1, entries 9, 10, 13, and 14, respectively) which were only distinct in CHI concentration. The former produced spherical hydrogel beads, while the latter formed raisin-like beads, as shown by Figures A1.9, A1.10, A1.13, and A1.14 of the Appendix. In fact, all the experiments containing 2.5 wt% CHI concentration generated this wrinkled type of beads, which could be related to pH, charge density, and conformational changes.

At pH values below 3, CHI depolymerization occurs via hydrolysis. At neutral and basic pH conditions above its pKa of 6.5, CHI can precipitate becoming insoluble. Between 3 and 6.5, CHI becomes soluble due to the protonation of the amine groups. [51] According to Sæther et al. [52], the pH determines the degree of protonation of the CHI amino groups. This conclusion was further supported by Chavasit et al. [53] reporting that at pH values of 3, 4, and 5 the degree of ionization of CHI was about 1.0, 0.95, and 0.85, respectively. In other words, as expected, the protonation of the amine groups decreases with an increase of the pH in the studied range.

Along this line, we can expect that the 1.0 wt% CHI solutions present a higher density of positive charges than the 2.5 wt% solutions, due to their corresponding pH of 3.5 and 4.5, respectively. As PEC formation depends on the charge neutralization achieved, the electrostatic interactions, and conformational changes [54],[55], a high charge density promotes electrostatic interactions, and therefore a more stable complex is obtained when using 1.0 wt% CHI instead of 2.5 wt% CHI. Additionally, as a polycation with a high density of positive charges tends to uncoil or expand its chains and have a more open conformation due to electrostatic repulsion [56], we assume that this facilitates the electrostatic interaction with the polyanion because the positively charged sites become more accessible. With 2.5 wt% CHI, as the charge density is lower and due to conformational constraints, these binding sites are not so accessible, and the complexation may be weaker.

It was also observed that during the polyelectrolyte complexation, the 2.5 % CHI beads would go through 3 stages. Initially, when they were dropped into the SPA solution, they were transparent. As coagulation proceeds, they turn whiter. And at the final stages of complexation, they would have the appearance of a yellow hollow raisin. To explain this behavior, we suppose that the complexation wasn't effective enough not only due to reduced electrostatic interactions but also due to a lack of charge complementarity, caused by an excess of CHI positive charges in comparison to the negative ones of SPA. The latter resulted in an excess of non-complexed CHI that ended up precipitating and forming the wrinkled yellow shell observed when the solution media achieved its final pH values in the range of 6 to 6.5.

This excessiveness and formation of a precipitated CHI shell were observed when dropping 2.5 wt% CHI solution in 1.0 and 2.0 wt% SPA bath, but not when using just 1.0 wt% CHI. From here, it is possible to suppose that despite having a lower charge density, 2.5 wt% CHI possesses a higher global charge than the 1.0 wt% CHI. Therefore, not just due to the reduced chances to form electrostatic interactions caused by its lower charge density, but also

due to the lack of charge complementarity resulting from its higher global charge, the 2.5 wt% CHI solution is more prone to form a precipitate shell of non-complexed CHI when in both 1.0 and 2.0 wt% SPA bath, than the 1.0 wt% CHI solution.

As we were able to produce spherical beads using both 1.0 and 2.0 wt% SPA solutions but only when using a 1.0 wt% CHI solution, it is fair to assume that the concentration of the polycation had a more significant impact than the concentration of the polyanion in the formation of beads, at least in the conditions explored in this work. The reasons behind this behavior might be related to the experimented range of the **concentration of the SPA solution**, and consequently its charge. As the pH of both 1.0 and 2.0 wt% SPA solutions was approximately 8, they were considered to have similar charge densities. On the other hand, the global charge was higher when using 2.0 wt% instead of 1.0 wt% SPA, because the concentration of carboxyl groups increased. Hence, based on the obtained results, we suggest that the values of charge density and global charge of both 1.0 and 2.0 wt% SPA were enough to form spherical and stable complexes with a 1.0 wt% CHI solution (Figures A1.9, A1.10, and A1.11 of the Appendix), but not enough when using a 2.5 wt% CHI solution (Figures A1.5-A1.8 and A1.13-A1.16 of the Appendix). Despite that, when complexing with 2.5 wt% CHI, the 2.0 wt% SPA solution resulted in more spherical and not so wrinkled beads than the ones obtained when using just 1.0 wt% SPA, which can be attributed to the increase of global charge in the SPA. This can be observed by comparing for instance figure A1.5 to A1.7 of the Appendix.

However, the polyelectrolyte concentrations are not the only factors decisive in the formation of beads. By comparing experiments $G1_{1\text{-}1\text{-}Ø\text{-}0.65}$, $G1_{1\text{-}1\text{-}CHI\text{-}0.65,}$ and $G1_{1\text{-}2\text{-}Ø\text{-}0.65}$ to experiences $G1_{1\text{-}1\text{-}Ø\text{-}0.32}$, $G1_{1\text{-}1\text{-}CHI\text{-}0.32,}$ and $G1_{1\text{-}2\text{-}Ø\text{-}0.32}$, respectively (Table 1, entries 9-11, and entries 1-3) it is observed that the last three didn't produce the desired spherical beads. As the only difference between them was the drop rate, it is logical to accept that it impacted the beads' formation.

To explain the **influence of the drop rate**, we suggest that the beads' formation is mainly driven by electrostatic interactions that occur in the first moments, between the drop and the solution, while the pH of the system hasn't significantly changed. During this time, CHI (being still in acidic pH, hence highly protonated) and SPA (being still in a basic pH, hence highly deprotonated) present the highest charge density of the entire complexation process, thus electrostatic interactions are easier to establish, and a more stable complex is obtained. After this initial time, the pH of the system will start to change, lowering the charge densities of both polyelectrolytes. If the drops enter the solution before this pH alteration, stable beads can be formed. If they only enter after, the formation of electrostatic interactions is not so effective, therefore producing weaker complexes. Knowing that the time necessary to completely inject the CHI drops into the SPA solution is inversely proportional to the dropping rate and hence, the higher the dropping rate, the lower the time, we suppose then, that contrary to what happens at a drop rate of 0.65 mL/min, a 0.32 mL/min rate is not sufficient to drop all the CHI solution into the SPA bath before the pH of the system starts to change, which leads to the formation of unstable beads.

The effects of the pH on the media of CHI-SPA complexation have also been studied by Takahashi et al. [57] with a view to the application of CHI for drug delivery formulations.

The authors reported that the unit molecular binding ratio of the CHI-SPA complex was greatly affected by pH, showing a change from 1:4 to 1:1.7 (CHI-SPA) with an increase in pH from 3.7 to 4.7. With increasing pH values, the degree of ionization in SPA tends to increase, while the tendency toward ionization of CHI molecules tends to decrease, supporting our idea that the pH of the system plays a major role in the complex formation.

Focusing now on the **influence of the crosslinker**, as we were able to produce beads with (experiment $G1_{1\text{-}1\text{-}CHI\text{-}0.65}$, Table 1, entry 10) and without glutaraldehyde (experiment $G1_{1\text{-}1\text{-}Ø\text{-}0.65}$, Table 1, entry 9), it is reasonable to accept that the formation of polyelectrolyte complexes was not dependent on this parameter, at least in the 1st Generation tested conditions. However, different shrinking behaviors were observed. As depicted in Figure 11 in the following section, while the beads in experiment $G1_{1\text{-}1\text{-}Ø\text{-}0.65}$ presented a 42.7% shrink from the hydrogel to the cryogel state, in experiment $G1_{1\text{-}1\text{-}CHI\text{-}0.65}$ the beads only shrank 37.1%, thus indicating that crosslinked beads tend to shrink less than the not cross-linked ones. This can be attributed to the establishment of covalent imine bonds between the amino groups of chitosan and the aldehyde groups of the crosslinker [58], resulting in the formation of a denser and more reticulated structure and a non-porous surface as illustrated in Figure 10.

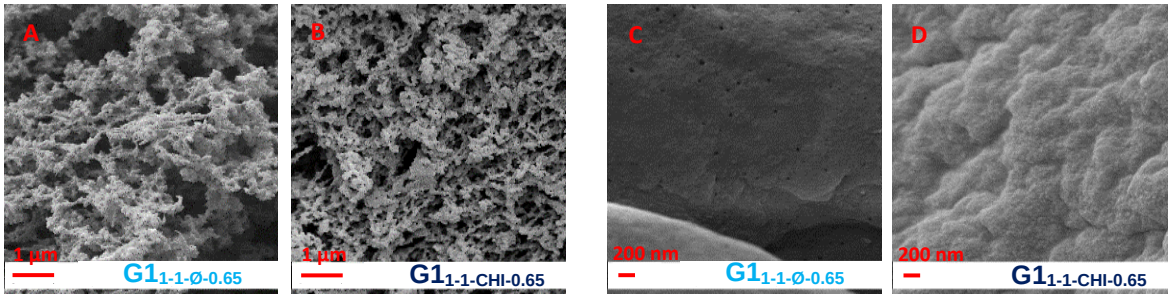

Figure 10 – Experiments $G1_{1\text{-}1\text{-}Ø\text{-}0.65}$ and $G1_{1\text{-}1\text{-}CHI\text{-}0.65}$ inner (A and B) and outer surface (C and D) SEM images

Because of that, the glutaraldehyde crosslinked beads are less prone to absorb water during polyelectrolyte complexation [59], and thus will shrink less during the solvent exchange and freeze-drying processes. Nevertheless, the study of the crosslinking influence in the beads' morphology will be further discussed in section 3.3 of the present work.

According to the data obtained, for the following beads' generations, it was decided to set the parameters of 1.0 wt% CHI and 0.65 mL/min rate, as the experiments that formed spherical beads had these values in common. The concentration of 1.0 wt% instead of 2.0 wt% SPA was also fixed following a lower production cost criterion. Additionally, it was shown to be possible to introduce a crosslinker and obtain the desired beads.

3.3. Beads' Production: 2nd Generation

Instead of testing all the possible combinations of the chosen variables as in the previous generation, our approach was different during the 2nd generation. Only one parameter at a time was varied, and the shrinking of the beads obtained from the experiments described in Table 2 and experiments $G1_{1\text{-}1\text{-}Ø\text{-}0.65}$ and $G1_{1\text{-}1\text{-}CHI\text{-}0.65}$ (Table 1, entries 9 and 10) from the 1st generation was compared to evaluate their stability.

Table 2 - 2nd Generation experiments

2nd generation					
Entry	**Experiments[a]**	**Sdiam (mm)**	**[NaOH] (mol/L) [b]**	**Xlinker Intro[c]**	**Solv**
17	**G2P1-4-0-Ø-t.but**	**4.0**	**0**	**Ø**	***tert*-butanol**
18	**G2P1-1.2-0-Ø-t.but**	**1.2**	**0**	**Ø**	***tert*-butanol**
19	G2P1-1.2-0-SPA-xxx	1.2	0	SPA solution	----------
20	G2P1-1.2-0-water-xxx	1.2	0	Water bath	----------
21	**G2P1-1.2-0.1-Ø-t.but**	**1.2**	**0.1 mol/L**	**Ø**	***tert*-butanol**

[a] Experiment designation = "Beads' Generation (G#) -P1- syringe tip external diameter (Sdiam)-[NaOH]-Xlinker introduction- alcohol gel solvent (Solv)", where P1=1.0 wt% CHI, 1.0 wt% SPA and 0.65 mL/min.
[b] Added to the SPA solution before coagulation.
[c] Ø= Not introduced. When introduced [Xlinker]= 0.13 wt% of the CHI solution.

The measurement of the beads' diameter allowed the assessment of the respective shrinking. This shrinking is illustrated in Figure 11 and was calculated based on the percentual diameter reduction between distinct gel states. The beads' diameter in each gel form can be found in Figure C1.1 of the Appendix. Experiment G2P1-1.2-0-SPA-xxx and G2P1-1.2-0-water-xxx (Table 2, entries 19 and 20, respectively) were not included in these graphs because the beads completely degraded during polyelectrolyte complexation, forming a white precipitate as shown in Figure A2.3 of the Appendix, and hence didn't go through solvent exchange or freeze-drying. We suspect that in the former case, CHI tended to escape from the interior of the beads to react with the GLU in the SPA bath, which could have caused the loss of form and stability of the beads. On the other hand, in the latter experiment the beads might have been immersed in a water bath with the crosslinker too soon (as they were only 2 h in the SPA solution instead of the usual 4 h), not giving enough time for charge compensation via electrostatic forces and rearrangements to occur, thus possibly resulting in an unstable complex that ended up degrading in the water bath due to the lack of prior effective complexation.

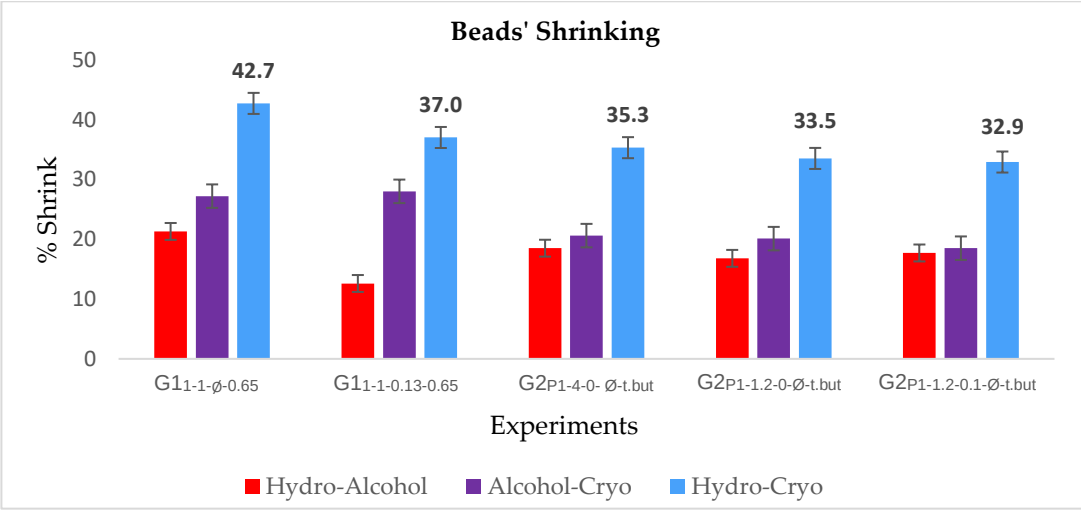

Figure 11 - Percentual shrinking of CHI beads obtained from different batches, in hydrogel to alcohol gel (red), alcohol gel to cryogel (purple), and hydrogel to cryogel (blue)

The **introduction of a needle at the end of the syringe pipe**, with the respective external diameter resulted in beads with a smaller diameter and less shrinking, as we can conclude by comparing experiments $G2_{P1\text{-}4\text{-}0\text{-}Ø\text{-}t.but}$ to $G2_{P1\text{-}1.2\text{-}0\text{-}Ø\text{-}t.but}$ (Table 2, entries 17 and 18, sequentially). By reducing the tip diameter, the drops' size also decreases. The CHI solution concentration didn't vary, so the charge density is constant. However, as the beads' size diminished, the global charge decreased as well. Thus, we hypothesize that charge neutralization occurs faster, and the beads complex better, forming a denser structure. Due to this, water diffusion into the complex is hampered and the water content inside the bead is reduced, leading to a smaller shrinking during solvent exchange and freeze-drying. The needle's influence on the size and shape of gel beads has been reported in several studies [60], [61] and the density's effect on CHI hydrogels has also been highlighted by Berger et al.[58], reporting that by increasing the density, the water content and swelling of the hydrogels decreased.

By comparing experiments $G2_{P1\text{-}1.2\text{-}0\text{-}Ø\text{-}t.but}$ (Table 2, entry 18) to $G2_{P1\text{-}1.2\text{-}0.1\text{-}Ø\text{-}t.but}$ (Table 2, entry 21), it was observed that the **introduction of NaOH** into the SPA bath resulted in bigger hydrogel beads and also less shrinking during the solvent exchange and freeze-drying processes (Figure C1 of the Appendix). To explain this, it is important to highlight that the addition of NaOH into the SPA bath (before coagulation) increased the solution pH to 11, and consequently led to an increased negative charge density of the polyanion. Thus, we assume that at the beginning of the polyelectrolyte complexation, the SPA solution had a higher charge density in experiment $G2_{P1\text{-}1.2\text{-}0.1\text{-}Ø\text{-}t.but}$ than in $G2_{P1\text{-}1.2\text{-}0\text{-}Ø\text{-}t.but}$, which facilitated the establishment of electrostatic interactions with the polycation. Additionally, the polycation extended its chains [56] to accommodate more polyanion, which resulted in bigger and more SPA enriched CHI beads, as will be later demonstrated in the FTIR analysis. However, as shown by Sakiyam et al. [62] hydrogels can exhibit different swelling behaviors according to their global charge. If they get negatively charged even slightly, OH^- may be excluded from the gel, reducing thus the water content inside the bead. Furthermore, the same authors reported that an excess of Na^+ can shield the electrostatic repulsion between the negative charges. This way, we hypothesize that the electrostatic repulsion between the carboxylate groups present in excess in the CHI beads was hindered by the addition of NaOH, hampering the water diffusion into the bead for steric reasons. Having a lower water content but a higher SPA content, the beads shrank less.

Morphological differences between these two experiments were also observed as depicted in Figures B2.2 and B2.3 of the Appendix, where the beads with NaOH exhibit a more reticulated structure on the inside and a grainy surface in comparison to experiment $G2_{P1\text{-}1.2\text{-}0\text{-}Ø\text{-}t.but}$ (Table 2, entry 18). Furthermore, the beads from experiment $G2_{P1\text{-}1.2\text{-}0.1\text{-}Ø\text{-}t.but}$ (Table 2, entry 21) exhibited some static electricity and plasticity.

The **influence of the solvent** can be also noticed when comparing experiments $G1_{1\text{-}1\text{-}Ø\text{-}0.65}$ and $G2_{4\text{-}0\text{-}Ø\text{-}t.but}$, where it is visible that the use of *tert*-butanol instead of ethanol led to a smaller shrinking of the beads. To understand that several factors should be considered. Subrahmanyam et al.[63] reported that the shrinkage behavior can be attributed to changing the solvent-matrix interactions when the pore-liquid gets less polar during the solvent exchange. The bigger the polarity difference, the more the gel will shrink. Additionally, as our

matrix is polar, solvents with higher polarity will have a bigger affinity to establish favorable interactions, thus shrinking less. This tendency has also been highlighted elsewhere in the literature [64], [65]. Between water, ethanol, and *tert*-butanol, water is the most polar and *tert*-butanol the less polar [66], we could expect that the beads would shrink less when exchanging from water to ethanol than from water to *tert*-butanol, but that was not the case. To explain this, we assume that the molar volume of the solvent, calculated by dividing its density by its molar mass, affects the shrinking as well. Because during solvent exchange water molecules are being replaced by solvent molecules, the size reduction of the bead caused by the volume of water diffusing out should be compensated by the volume of solvent diffusing in to reduce the shrinking. Therefore, despite having a lower affinity than the water and ethanol molecules, *tert*-butanol molecules are bigger (i.e possess a larger molar volume), and hence can provoke a smaller shrinking of the CHI beads. In addition, there is another parameter that plays a major role, which is the concentration gradient of the solvent. When using ethanol, we did a one-step solvent exchange, meaning that the CHI beads were changed to a pure ethanol bath after PEC. On the other hand, when using *tert*-butanol a two-step solvent exchange was done, immersing the beads first in a *tert*-butanol/water mixture (50.0 v/v%) during the first 4h and then renewing it with a 100% *tert*-butanol bath. As reported in the previously mentioned study by Subrahmanyam et al. [63] when the gel is subjected to an initial concentration gradient of 100% (i.e pure solvent) a huge driving force is generated from the exchange between water and solvent molecules, resulting in a severe shrinking of the beads. However, when the gradient is lowered by using solvent/water mixtures, the driving force is reduced along with the shrinkage, due to a slower and gentler exchange between molecules. Hence, the smaller shrinking verified when using *tert*-butanol instead of ethanol during solvent exchange can be related to the concentration gradient applied in the former case.

Furthermore, the type of solvent also influences the beads shrinking during freeze-drying. According to Prostredný et al.[67] solvents can cause strong stresses that act on the pore wall resulting in increased shrinking. These stresses can be caused by volume variation of the solvent due to solidification and sublimation processes [68]. Therefore, we suppose that the beads' shrinking during freeze-drying was smaller in experiment $G2_{P1\text{-}4\text{-}0\text{-}Ø\text{-}t.but}$ (Table 2, entry 17) in comparison with experiment $G1_{1\text{-}1\text{-}Ø\text{-}0.65}$ (Table 1, entry 9) because the volume changes of ethanol are more pronounced than of *tert*-butanol. It should be also taken into account that ethanol possesses a lower melting point (-114.5ºC) than *tert*-butanol (25.6ºC), which can result in incomplete solidification during the freezing process. Due to that, the unfrozen solvent may evaporate instead of sublimating during the drying process, leading to the loss of structure and degradation of the beads.[69]

In addition to volume shrinkage, the solvents also affect other properties of the gels. Beads produced from experiment $G2_{P1\text{-}4\text{-}0\text{-}Ø\text{-}t.but}$ (Table 2, entry 17) were brittle but less rigid than the beads obtained from experiment $G1_{1\text{-}1\text{-}Ø\text{-}0.65}$ (Table 1, entry 9). Different structure morphologies can also be observed in Figures B1.1 and B2.1 of the Appendix.

Summing all the previously obtained data, the utilization of a needle, introduction of NaOH, the addition of the crosslinker in the CHI solution, and the use of *tert*-butanol as solvent were fixed for the 3rd generation, as these parameters resulted in reduced shrinking and hence, higher stability of the beads.

3.4. Beads' Production: 3rd Generation

Having set the best parameters resulting from the previous experiments, this third and last generation of beads was performed to introduce several types of IL derivatives as crosslinkers (Figure I.1 of the Appendix) according to the conditions shown in Table 3. Additionally, the obtained beads would be tested in the capture and conversion of CO_2.

Table 3 - 3rd Generation experiments

	3rd generation		
Entry	**Experiment[a]**	**[Xlinker](%wt)[b]**	**Xlinker type**
22	**G3P2-0.13-GLU**	**0.13**	**GLU**
23	G3P2-0.26-GLU	0.26	GLU
24	**G3P2-0.13-TEA.OAc**	**0.13**	**TEA.OAc**
25	G3P2-0.26-TEA.OAc	0.26	TEA.OAc
26	**G3P2-0.13-THMAMS**	**0.13**	**THMAMS**
27	**G3P2-0.26-THMAMS**	**0.26**	**THMAMS**
28	**G3P2-0.13-TEA.Cl**	**0.13**	**TEA.Cl**
29	G3P2-0.26-TEA.Cl	0.26	TEA.Cl
30	**G3P2-0.13-THMAMS-60ºC**	**0.13**	**THMAMS[c]**
31	**G3P2-0.26-THMAMS-60ºC**	**0.26**	**THMAMS[c]**

[a] Experiment designation = "Beads' Generation (G#) - P2- [Xlinker]-Xlinker type", where P2=1.0 wt% CHI, 1.0 wt% SPA, 0.65 mL/min, Xlinker introduced in de CHI solution, syringe tip external diameter (Sdiam) of 1.2mm, 0.1 mol/L NaOH, and *tert*-butanol as alcohol gel solvent.
[b] [Xlinker]= 0.13 or 0.26 wt% of the CHI solution.
[c] The beads were left for 3h in the SPA solution plus 1h in a water bath at 60ºC to activate the THMAMS.

All the crosslinkers produced stable beads when the respective concentration was 0.13 wt%. However, when this concentration was increased to 0.26 wt%, only the experiments that used THMAMS formed the desired cryogel beads. The remaining experiments resulted in complete or partial degradation of the beads as depicted in Figures A3.2, A3.4, and A3.8 of the Appendix. Thus, it can be assumed that there is a critical crosslinker ratio, that when exceeded hampers the polyelectrolyte complexation and that this critical ratio might vary with the type of crosslinker used.

Similar conclusions were reported by Figueiredo et al. [70] highlighting that there is an optimum ratio between poly(vinyl alcohol) and glutaraldehyde that favors the crosslinking of the polymer and that a low glutaraldehyde concentration promotes a higher crosslinking density. A very low glutaraldehyde content might not be enough to crosslink effectively, whereas higher amounts of the aldehyde can lead to the branching of PVA, possibly due to

the increase of viscosity in comparison to the more diluted solution, which compromised the diffusivity of the molecules. The branching increases the space among chains and leads to higher solubility in water. This effect of branching rather than further crosslinking has also been described by Hoti et al. [71] attributing the existence of a maximum degree of crosslinking to steric effects.

Following this line and according to the data obtained, we can assume that the crosslinking density tended to increase while the crosslinker content was increasing until the value of 0.13 wt% for all the crosslinkers tested. On the other hand, from 0.13 to 0.26 wt% it only increased for THMAMS, decreasing for the other crosslinkers. Furthermore, the shrinking behavior of the beads (Figure C1.2 of the Appendix) can also be a measure of the crosslinking density, as higher crosslinking densities promote a more packed network, reducing the free volume of material, and thus impeding the access of water molecules. Therefore, the higher the crosslinking density, the less will the beads shrink.

To try to explain why values above a certain crosslinking critical ratio interfere in polyelectrolyte complexation several factors should be understood. First, it must be considered that if the crosslinking concentration is above the critical ratio, and the crosslinking density is low, then the crosslinker added to the chitosan did not react correctly and might be causing instability in the beads. Additionally, the reacted crosslinker molecules might inhibit chain rearrangements and hinder electrostatic interactions between polyelectrolytes which are the main driving force in the formation of stable complexes. Lastly, by introducing SPA and these hydroxyl enriched crosslinkers, the hydrophilic character of the CHI beads increases, and hence more water can be absorbed. Given that, we suppose that the experiments that exceeded the respective crosslinking critical ratio ($G3_{P2\text{-}0.26\text{-}GLU}$, $G3_{P2\text{-}0.26\text{-}TEA.OAc}$, and $G3_{P2\text{-}0.26\text{-}TEA.Cl}$, Table 3, entries 23,25, and 29, respectively) absorbed too much water due to the increased hydrophilicity and reduced crosslinking density, surpassing the water capacity of the beads, hence leading to their degradation.

Furthermore, to make sure that the energy needed to activate the crosslinkers was being achieved and thus to optimize the introduction of the IL-derivatives, experiments $G3_{P2\text{-}0.13\text{-}THMAMS\text{-}60^{o}C}$ and $G3_{P2\text{-}0.26\text{-}THMAMs\text{-}60^{o}C}$ (Table 3, entry 30 and 31, sequentially) were performed in similar conditions of experiments $G3_{P2\text{-}0.13\text{-}THMAMS}$ and $G3_{P2\text{-}0.26\text{-}THMAMs}$, but instead of being 4 h in the SPA solution for polyelectrolyte complexation, they remained only 3 h in the SPA solution, plus 1 h in a water bath at 60 ºC. As it can be seen by comparing Figures B3.3 to B3.6 and B3.4 to B3.7 of the Appendix, this increase in temperature activated the crosslinker more effectively, causing notable changes in the beads' structure.

Interestingly, all the experiments resulted in beads with some static electricity, plasticity, and a whitish color. However, depending on the concentration and type of crosslinker, different structures of the complexes can be produced [71], [72], as is illustrated in Figures B3.1 to B3.7 of the Appendix. Experiment $G3_{P2\text{-}0.13\text{-}TEA.OAc}$ (Table 3, entry 24) stands out because contrary to the rest, its outer surface is not so grainy, reminding instead of the appearance of seaweed leaves. Furthermore, experiments $G3_{P2\text{-}0.13\text{-}THMAMS\text{-}60^{o}C}$ and $G3_{P2\text{-}0.26\text{-}THMAMs\text{-}60^{o}C}$ should also be highlighted, as they appear to have a more reticulated structure in comparison to the rest.

3.5. Textural properties

BET analysis was conducted to evaluate the impact of the assigned experimental parameters on the surface area, pore volume, and pore size of the beads, as depicted below in Table 4. Furthermore, these surface area properties are of great interest for the CO_2 capture and catalysis fields and will be further addressed in sections 3.7 and 3.8.

Table 4 - Physical parameters of beads samples measured by N_2 adsorption-desorption isotherms

Entry	Experiment	Surface Area (m^2/g)	Pore Volume (cm^3/g)	Pore Size (nm)
1	$G1_{1\text{-}1\text{-}Ø\text{-}0.65}$	56.219 ± 0.503	0.271	19.302
2	$G1_{1\text{-}1\text{-}CHI\text{-}0.65}$	61.547 ± 0.642	0.299	19.455
3	$G2_{P1\text{-}4\text{-}0\text{-}Ø\text{-}t.but}$	38.482 ± 0.648	0.234	24.355
4	$G2_{P1\text{-}1.2\text{-}0\text{-}Ø\text{-}t.but}$	64.728 ± 0.847	0.345	21.366
5	$G2_{P1\text{-}1.2\text{-}0.1\text{-}Ø\text{-}t.but}$	41.285 ± 0.851	0.187	18.160
6	$G3_{P2\text{-}0.13\text{-}GLU}$	51.109 ± 0.383	0.200	15.687
7 [a]	~~$G3_{P2\text{-}0.13\text{-}TEA.OAc}$~~	~~24.026 ± 0.462~~	~~0.082~~	~~13.683~~
8	$G3_{P2\text{-}0.13\text{-}THMAMS}$	42.776 ± 0.691	0.206	20.653
9	$G3_{P2\text{-}0.13\text{-}THMAMS\text{-}60ºC}$	56.296 ± 0.633	0.242	17.191
10	$G3_{P2\text{-}0.26\text{-}THMAMS}$	46.430 ± 0.784	0.224	18.308
11	$G3_{P2\text{-}0.26\text{-}THMAMS\text{-}60ºC}$	86.716 ± 0.897	0.421	19.405
12	$G3_{P2\text{-}0.13\text{-}TEA.Cl}$	41.849 ± 0.323	0.205	19.571

[a] The measurements in entry 7 were strikethrough as they were considered invalid according to the contrasting results obtained in section 3.8 and the data from Table I.1 of the Appendix.

Firstly, it is important to highlight that by analyzing the experiments' SEM images (Figures B1.1-B3.7 of the Appendix), and their isotherms, which are mainly either type II or III [73](as it can be seen in Figures D1-D12 of the Appendix), our material seems to be macroporous. However, the pore size of all the experiments described in Table 4 is in the mesoporosity range (2-50 nm). The reason behind these opposite values might lie in the fact that although the nitrogen porosimetry can qualitatively indicate the presence of macropores through isotherms, it cannot measure quantitatively them. Thus, for the calculation of the pore size, the program uses a model that fits for mesoporosity but that is not sensible to macroporosity. Nevertheless, the data obtained can mean that the synthesized beads have both mesoporosity and macroporosity or that their porosity is so insignificant that the material could be considered non-porous. Further studies would be required to evaluate the pore size distribution and to better understand what kind of porous material the produced beads are. As the nitrogen porosimeter is not sensible enough to do so, this section discussion is more focused on the effect of the tested parameters in the surface area and pore volume, rather than in the pore size.

Starting by comparing experiment $G1_{1\text{-}1\text{-}ø\text{-}0.65}$ (Table 4, entry 1) to experiment $G2_{P1\text{-}4\text{-}0\text{-}ø\text{-}t.but}$ (Table 4, entry 3), the influence of the solvent can be observed. The surface area and pore volume decreased in the former, but the pore size increased. This might be a consequence of the pore size distribution. As reported by Tamon et al. [68] freeze-drying with water gives a sharper pore size distribution and smaller pore size than freeze-drying with *tert*-butanol.

Hence, due to its dispersion in terms of pore size, we suppose that *tert*-butanol formed several large and small pores (both in the mesoporosity range). However, during the freeze-drying process, most of the smaller pores must have collapsed, while the larger ones held their shape better. Consequently, this resulted in an increment of the pore size, but a decrease in both surface area and pore volume.

On the other hand, by comparing experiment $G2_{P1\text{-}4\text{-}0\text{-}Ø\text{-}t.but}$ with experiment $G2_{P1\text{-}1.2\text{-}0\text{-}Ø\text{-}t.but}$ (Table 4, entries 3 and 4, respectively) it is possible to notice the impact of using a needle at the end of the syringe tip. The latter had a sharp increase in terms of surface area and pore volume, but a decrease in pore size. We suggest that the needle led to the formation of a denser, yet more porous bead. Due to their density, the beads exhibited a reduced shrinking behavior, holding better their final structure.

The NaOH introduction resulted in a decrease in the surface area, pore volume, and pore size, as can be seen by comparing experiment $G2_{P1\text{-}1.2\text{-}0\text{-}Ø\text{-}t.but}$ (Table 4, entry 4) to experiment $G2_{P1\text{-}1.2\text{-}0.1\text{-}Ø\text{-}t.but}$ (Table 4, entry 5). To explain this, we hypothesize that due to the fact the NaOH was hampering the water diffusion into the beads as explained previously, the solvent exchange might also have been restricted. This possibly led to the loss of pores during freeze-drying, resulting in a surface area and pore volume decrease.

Additionally, the effect of the crosslinker can be observed by comparing experiment $G2_{P1\text{-}1.2\text{-}0.1\text{-}Ø\text{-}t.but}$ (Table 4, entry 5) with experiments $G3_{P2\text{-}0.13\text{-}THMAMS}$, $G3_{P2\text{-}0.13\text{-}THMAMS\text{-}60ºC}$, $G3_{P2\text{-}0.26\text{-}THMAMS}$, $G3_{P2\text{-}0.26\text{-}THMAMS\text{-}60ºC}$, and $G3_{P2\text{-}0.13\text{-}TEA.Cl}$ (Table 4, entries 8-12, respectively). In a general way, an increase in both surface area and pore volume was verified when using a crosslinker. We suppose that the crosslinker helps the beads hold their structure by reducing their shrinking behavior. Thus, more pores will remain open or at least tend to close less during the beads' shrinking, which results in a higher surface and pore volume.

It is also important to note that the influence of the crosslinker depends on its type and concentration, both affecting how effectively the IL-derivative can crosslink. Despite no significant changes being noticed when comparing the surface properties of the beads with 0.13 wt% THMAMS or TEA.Cl, we were expecting an increase in both surface area and pore volume when using 0.13 wt% TEA.OAc. Although, the opposite occurred as can be seen in experiment $G3_{P2\text{-}0.13\text{-}TEA.OAc}$ (Table 4, entry 7), these BET values were reported as invalid, considering they were completely different from the rest and contradictory to the catalysis results obtained in section 3.8. Furthermore, we should take into consideration Table I.1 of the Appendix, with complementary information about the batches.

An increase in the crosslinker concentration ($G3_{P2\text{-}0.13\text{-}THMAMS}$ vs $G3_{P2\text{-}0.26\text{-}THMAMS}$) and the use of higher temperatures during complexation ($G3_{P2\text{-}0.26\text{-}THMAMS}$ vs $G3_{P2\text{-}0.26\text{-}THMAMS\text{-}60ºC}$) led to an increment in surface area and pore volume. Notably, this effect was more prominent in the latter. Despite the pore size being comparable, experiment $G3_{P2\text{-}0.26\text{-}THMAMS\text{-}60ºC}$ (Table 4, entry 11) had a surface area and pore volume more than double of the experiment $G3_{P2\text{-}0.26\text{-}THMAMS}$ (Table 4, entry 10). The reason behind this can be attributed to the increased interactions between the THMAMS and the beads caused by the crosslinker activation with temperature, which promoted a more effective crosslinking that allowed the beads to hold better their structure and hence resulted in a sharper increase of the pore volume and surface area.

3.6. **FTIR**

FTIR analysis was performed to investigate the structural composition of the beads, and possible interactions between CHI, SPA, and other reactants involved in the beads' preparation, as the appearance of a peak at a specific wavenumber is representative of specific chemical bonds. Figure 12 shows the FTIR spectra of pure CHI (blue) and pure SPA (red), as well as experiments $G1_{1\text{-}1\text{-}Ø\text{-}0.65}$ (Table 1, entry 9) (yellow), $G2_{P1\text{-}1.2\text{-}0.1\text{-}Ø\text{-}t.but}$ (Table 2, entry 21)(pink), $G3_{P2\text{-}0.13\text{-}TEA.OAc}$ (Table 3, entry 24) (green) and $G3_{P2\text{-}0.26\text{-}THMAMS}$ (Table 3, entry 27) (brown). Complementary FTIR spectra of the remaining experiments and crosslinkers can be found in section E of the Appendix.

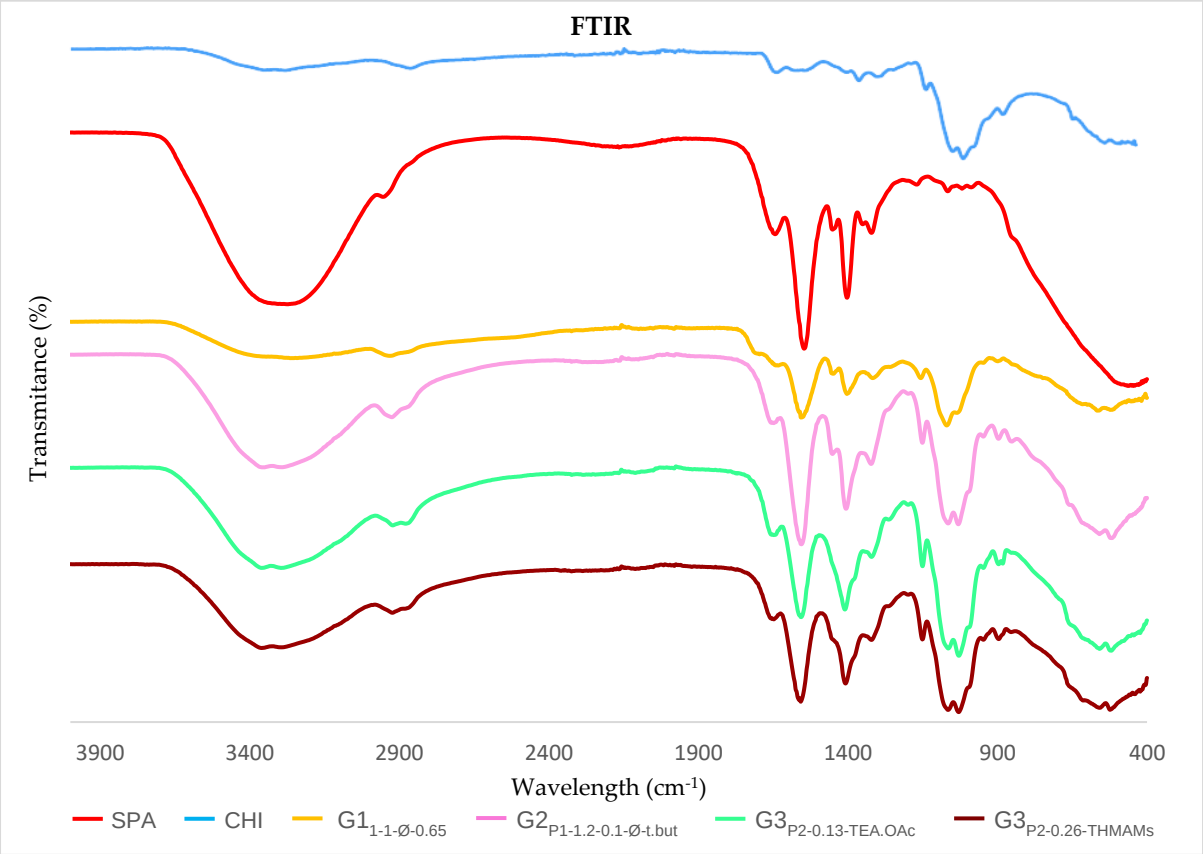

Figure 12 - FTIR spectra of several experiments from the three generations

Illustrated in blue, the spectrum of chitosan exhibited a characteristic band between 3500-3200 cm^{-1} which was assigned to the typical O-H and N-H stretching vibrations on the polysaccharide backbone. At 2871 cm^{-1}, the peak was attributed to the CH_2 stretching vibration of the pyranose ring. Peaks at 1646 cm^{-1} and 1559 cm^{-1} were ascribed to the vibration of amide I (C=O stretching) and amide II (NH bending), respectively. Bands identified at 1414 cm^{-1} belong to bending methylene groups and at 1374 cm^{-1} was associated with amide II groups bending. The vibration at 1308 cm^{-1} corresponded to $-CH_3$ stretch in acetyl groups, while the band at 1258 cm^{-1} was related to C-O-H groups. Bands at 1151, 1062, and 1027cm^{-1} were attributed to the symmetric and asymmetric stretches of C-O-C bonds. The band at 890 cm^{-1} was attributed to C-H wagging of anomeric carbon in the saccharide structure [74]–[76].

On the other hand, in the SPA spectrum (red), a wide band corresponding to stretching vibrations of the hydroxyl group appears in the range of wave number 3700-2980 cm^{-1}. The band with a peak at 2946 was ascribed to the C-H stretching vibrations. Characteristic bands 1641 cm^{-1} were assigned to deformation vibrations of C-O-H groups. The two bands at 1547 cm^{-1} and 1321 cm^{-1} were attributed to the symmetrical stretching vibrations of carboxyl anions -COO, while the band at 1401 cm^{-1} was assigned to asymmetrical stretching of the same anions. The band at 1246 cm^{-1} was associated with the stretching vibrations of C-O bond and deformation vibrations of C-O-H group [77]–[79].

In the FTIR spectra of mixed oppositely charged polyelectrolytes, we observed changes in some bands' placement and disappearance/appearance of new peaks in comparison to pure SPA or CHI. For experiments represented in Figures E2 and E3 of the Appendix, new peaks appearing near 1708 cm^{-1} and 1550 cm^{-1}, were assigned to the carboxyl groups of SPA bound with CHI and amino groups of CHI bound with SPA, respectively, which indicates that the COO^- groups were able to complex with protonated amino groups through electrostatic interactions, thus forming a polyelectrolyte complex. Furthermore, a pH increase in the media of complexation leads to a decrease in the peak near 1708 cm^{-1} and to an increase in that near 1550 cm^{-1} [57]. Hence, the former can only be observed in the FTIR spectra of experiments $G1_{1\text{-}1\text{-}Ø\text{-}0.65}$ and $G1_{1\text{-}1\text{-}CHI\text{-}0.65,}$ while the latter is more intense in the FTIR spectra of experiments $G2_{P1\text{-}1.2\text{-}0.1\text{-}Ø\text{-}t.but}$ to $G3_{P2\text{-}0.13\text{-}TEA.Cl}$ (Figures E2 and E3 of the Appendix), which were made in higher pH, due to the addition of NaOH. In fact, the introduction of NaOH also led to a more pronounced increase of the wideband centered near 3400 cm^{-1} resulting from additional hydroxyl groups, as can be seen by comparing experiments $G1_{1\text{-}1\text{-}Ø\text{-}0.65}$ (yellow) vs $G2_{P1\text{-}1.2\text{-}0.1\text{-}Ø\text{-}t.but}$ (pink), for example. Lastly, the crosslinking influence was difficult to observe using FTIR, as the spectrum of the experiment without crosslinker (pink) is very similar to spectra of the experiments that involved crosslinking (green or brown) in similar conditions. This was expected due to the low crosslinking concentrations utilized. Despite that, in experiments $G3_{P2\text{-}0.13\text{-}THMAMS\text{-}60^oC}$ (white blue) and $G3_{P2\text{-}0.26\text{-}THMAMS\text{-}60^oC}$ (yellow) (Figure E3 of the Appendix), a small peak possibly ascribed to C-N stretching appeared at 1380 cm-1, which might be an indicator that an increase in temperature favors the crosslinker activation, thus increasing the IL-derivates concentration inside the beads. On the other hand, characteristic peaks of SPA near 1550 cm^{-1} and 1424 cm^{-1} were more pronounced in experiment $G2_{P1\text{-}1.2\text{-}0.1\text{-}Ø\text{-}t.but}$ (pink) than in $G3_{P2\text{-}0.13\text{-}TEA.OAc}$ (green) or $G3_{P2\text{-}0.26\text{-}THMAMS}$ (brown), which can be indicative that crosslinking competes for and can hinder complexation sites between polyelectrolytes, thus hampering polyelectrolyte complexation.

3.7. CO_2 Capture

To test the CO_2 capture capacity of the beads, a CO_2 flow with increasing duration was made pass through several bead batches (entries 24, 26-28, 30-31, from Table 3), which were subsequently analyzed through FTIR to evaluate possible structural changes. The spectra are focused in the range from 1800 to 800 cm^{-1} where the main variations in the peaks were noticed but complementary spectra information can be found in Section F of the Appendix. The spectra of experiment $G3_{P2\text{-}0.26\text{-}THMAMS\text{-}60^oC}$ at different CO_2 flux times is depicted in Figure 13.

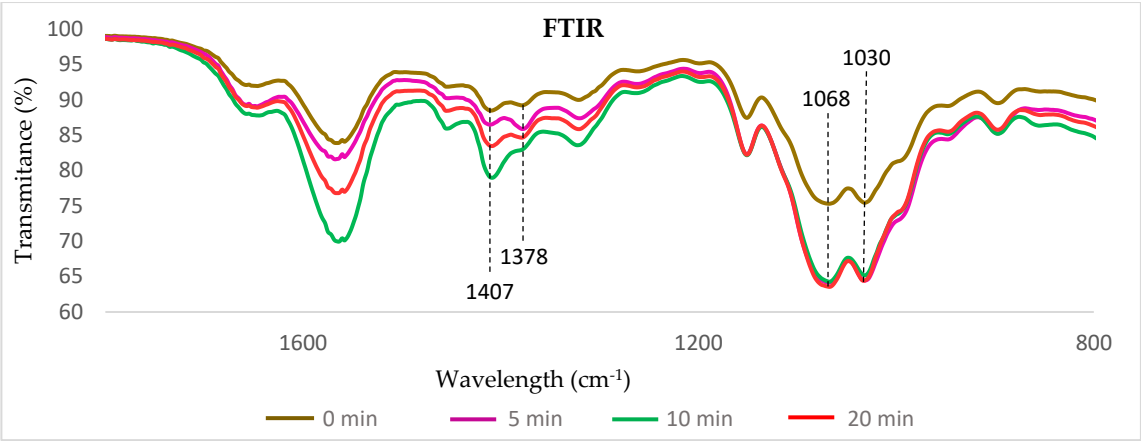

Figure 13- Experiment $G3_{P2\text{-}0.26\text{-}THMAMS\text{-}60^{o}C}$ FTIR after 0, 5, 10, and 20 min of CO_2 flux time

As it can be seen, the bands at 1068 cm^{-1} and 1030 cm^{-1}, ascribed to C-N and C-O stretching [80], [81], became more intense for CO_2 flux times of 5, 10, and 20 min. Furthermore, the bands at 1407 cm^{-1} and 1378 cm^{-1} tend to shift, increasing and decreasing their intensity with time. These bands might be attributed to carbonate and bicarbonate formation, respectively [80], [82]. Despite being difficult to precisely assign their contributions, as the bands of carbonate and bicarbonate are close to each other and/or overlapping [80], [81], [83], if we compare the FTIR spectra of experiments that have an IL-derivative (Figures F2-F7 of the Appendix) to the one that doesn't (Figure F1 of the Appendix), only the former show similar variations in the absorption bands, which might be indicative of the formation of new species.

3.8. Catalysis

The beads crosslinked with IL-derivates obtained in the 3rd generation (i.e experiments $G3_{P2\text{-}0.13\text{-}TEA.OAc}$, $G3_{P2\text{-}0.13\text{-}THMAMS}$, $G3_{P2\text{-}0.26\text{-}THMAMS}$, $G3_{P2\text{-}0.13\text{-}TEA.Cl}$, $G3_{P2\text{-}0.13\text{-}THMAMS\text{-}60^{o}C}$, and $G3_{P2\text{-}0.26\text{-}THMAMS\text{-}60^{o}C}$ corresponding to Table 3, entries 24,26,27,28,30, and 31, respectively) were tested as a catalyst for the synthesis of cyclic carbonate from the cycloaddition of CO_2 and styrene oxide, as exemplified in Figure 14. Furthermore, TBA.Br was used as a co-catalyst, and no catalytic activity was detected in the absence of it. The role of the co-catalyst during cyclic carbonate formation is to provide a nucleophile (commonly a halide anion) that facilitates the ring-opening of the epoxide. Thus it is desired that it possesses a good catalytic activity resulting from a balance between nucleophilicity and the leaving group ability of the halide anion [84].

However, tetrabutylammonium halides are not the best choice to be used alone as catalysts for cyclic carbonate formation as generally, they need harsh reaction conditions due to the lack of a hydrogen bond donor group required for the activation of an epoxide [85]. In this work, the hydrogen bonds were provided by chitosan@IL-derived beads enriched with hydrogen bond donors groups (–OH, –COOH, $–NH_2$) capable of activating the epoxide.

The catalytic activity of beads was evaluated in terms of conversion and selectivity, which were calculated through NMR integration of the ^1H NMR signals of the crude mixture as shown in figure 15.

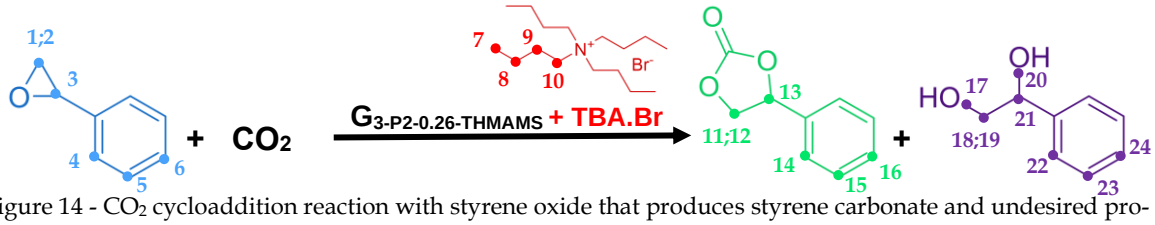

Figure 14 - CO_2 cycloaddition reaction with styrene oxide that produces styrene carbonate and undesired propane-1-2-diol, using experiment $G_{3P2\text{-}0.26\text{-}THMAMS}$ as catalyst, TBA-Br as co-catalyst, at 80ºC, 1 bar, and 72h

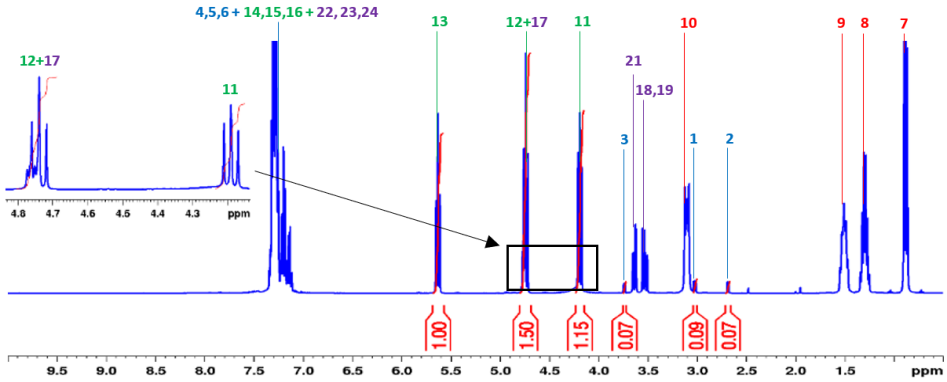

Figure 15 - ^{1}H-NMR spectrum integration and peaks identification from the reaction described in Figure 14

In ^{1}H-NMR spectroscopy, the signals can be characterized by an integral value proportional to the number of hydrogens to which each peak corresponds. This way, the conversion and selectivity of the reaction can be calculated by using Equations 1 and 2, respectively:

$$Conversion = \frac{\int \text{Styrene Carbonate} + \int \text{Diol}}{\int \text{Styrene Oxide} + \int \text{Styrene Carbonate} + \int \text{Diol}} \quad (1) \qquad Selectivity = \frac{\int \text{Styrene Carbonate}}{\int \text{Styrene Carbonate} + \int \text{Diol}} \quad (2)$$

In an initial phase, to check the feasibility in an industrial context and evaluate the possibility to use mild conditions, the catalytic performance of the beads was tested at 80 ºC, CO_2 pressure of 1 bar, and 72 h reaction time, as depicted in Figure 16.

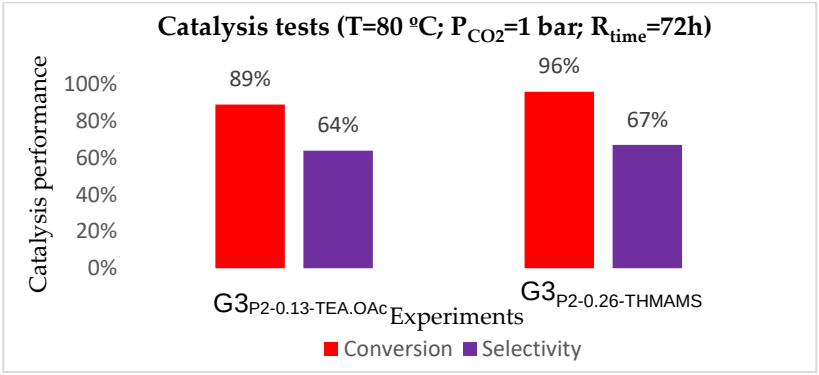

Figure 16 - Catalytic activity of $G3_{P2\text{-}0.13\text{-}TEA.OAc}$ and $G3_{P2\text{-}0.126\text{-}THMAMS}$ batches with 72h reaction time, under 80ºC and a CO_2 pressure of 1 bar, (no catalytic activity observed with the same batches in the absence of co-catalyst)

According to the literature, the reaction time is an important factor that needs to be optimized to obtain the best results in the catalysis reaction. If the time is too short the reaction might not occur completely and hence the conversion rates will be low. In contrast, if the reaction time is too long it might be not beneficial for the reaction system, as the catalytic

activity can be compromised by the formation of undesired secondary products or degradation of the cyclic carbonates [86].

Initially, the reaction time was set to 72 h so that the reaction would be completed after that period. It was possible to achieve conversions of 89% and 96%, for experiments $G3_{P2\text{-}0.13\text{-}TEA.OAc}$ and $G3_{P2\text{-}0.13\text{-}THMAMS}$, respectively. However, the selectivities obtained were only in the range of 60-70%, which can be ascribed to the formation of undesired secondary products (diol) (Figures H2.2 and H2.3 of the Appendix). Xiong et al. [86] achieved similar conclusions using 0.08g of polymer-supported quaternary phosphonium salt as a catalyst at 150 ºC and 50 bar of CO_2 pressure, reporting an increase in the yield/selectivity with the reaction time and maximum conversion of 98,6% within 6 h. Above that time limit, both yield and selectivity decreased. Several other researchers support this conclusions [38], [87], [88].

In an attempt to study the effect of chitosan@IL-derived beads' formulation, while simultaneously trying to be more time-efficient due to experimental constrictions, CO_2 pressure and reaction time were varied, as shown in Table 5.

Table 5 - Catalytic activity of several batches after 4h reaction time under 80ºC and a CO_2 pressure of 5 bar. The same batches registered no catalytic activity in the absence of co-catalyst.

Entry	Catalyst	Co-catalyst	Conversion	Selectivity
1	$G2_{P1\text{-}1.2\text{-}0.1\text{-}0\text{-}t.but}$	TBA.Br	48%	>99%
2	**$G3_{P2\text{-}0.13\text{-}TEA.OAc}$**	**TBA.Br**	**69%**	**>99%**
3	$G3_{P2\text{-}0.13\text{-}THMAMS}$	TBA.Br	45%	>99%
4	$G3_{P2\text{-}0.13\text{-}THMAMS\text{-}60}$	TBA.Br	49%	>99%
5	**$G3_{P2\text{-}0.26\text{-}THMAMS}$**	**TBA.Br**	**63%**	**>99%**
6	**$G3_{P2\text{-}0.26\text{-}THMAMS\text{-}60}$**	**TBA.Br**	**72%**	**>99%**
7	$G3_{P2\text{-}0.13\text{-}TEA.Cl}$	TBA.Br	48%	>99%

The effect of CO_2 pressure on cyclic carbonates preparations has been extensively studied resulting in an increased reaction rate with an increase in pressure up to a certain limit, and a decrease in the rate above that limit. As an example of that, Xiong et al.[86] in the previous study reported a yield of 77.5% at a CO_2 pressure of 20 bar, which increased up to 98% when the pressure was 50 bar, but decreased to 92% when it was at 55 bar. According to Webb et al.[89] this can be explained by the pressure effect on the concentration of two phases: top phase enriched with CO_2 (gas) and bottom phase enriched with epoxides (liquid). First, at low CO_2 pressures, the concentration of CO_2 in the liquid phase is little. With increasing pressure, the solubility of CO_2 in the epoxides increases, favoring the cycloaddition reaction. At higher pressures, however, the concentration of epoxides and catalyst is too low, reducing thus the reaction rate and the product yield. On the other hand, if the CO_2 is below the optimal value it could lead to the formation of side products and loss of selectivity [32].

In our experiments, by increasing the CO_2 pressure, an improvement in conversion would be expected. However, the opposite occurred. To explain this, we hypothesize that the reaction time reduction was substantial enough to restrict and overcome the benefits of increasing the pressure, thus lowering the conversion instead. In addition, as an increment in selectivity up to >99% was also verified, this possibly reflects that the catalysis reaction needed

more time to be completed. Despite that, the reaction conditions tested still allowed us to study the catalytic performance of several experiments. According to the data obtained in Table 5, three major factors might have been responsible for the variation of the catalytic activity. These are: the type and concentration of crosslinker, as well as its surface properties.

The influence of the first factor can be directly seen by comparing experiment $G3_{P2\text{-}0.13\text{-}THMAMs}$ to $G3_{P2\text{-}0.26\text{-}THMAMS}$ (Table 5, entries 3 and 5, respectively). Despite both achieving >99 % selectivity, the conversion of the former was 45%, while the latter had a conversion of 63%. As the only difference between them is the amount of crosslinker used it is fair to assume that an increase in the crosslinker concentration led to higher conversion. To explain this we suppose that by increasing the concentration of the THMAMS, the concentration of the -OH groups (which are present on tris(2-hydroxyethyl)methylammonium cation) also increase. Thus, there was an increment in the amount of hydrogen bond donors, which facilitates the ring-opening of epoxides (rate-determining step) by reducing its energy barrier through the formation of hydrogen bonds, resulting consequently in higher conversion. Furthermore, it should be also considered that in this case, by increasing the crosslinker concentration, the CO_2 sorption via THMAMs might have been facilitated, and hence the energy barrier to activate the CO_2 was reduced, promoting a better catalytic activity. Additionally, it should not be discarded that due to conformational changes caused by an increased crosslinker concentration, both hydrogen bond donor and CO_2-philic groups present in the CHI beads could be more exposed, and consequently should result in higher CO_2 adsorption.

It must be highlighted as well that, by increasing the temperature to activate the IL-derivative during the beads' synthesis, we were favoring the interactions and the crosslinking of THMAMS inside the beads. Thus, a higher concentration of THMAMs became available inside our material, resulting in higher conversions for the reasons proposed in the previous paragraph. Experiments $G3_{P2\text{-}0.13\text{-}THMAMS\text{-}60^{o}C}$ and $G3_{P2\text{-}0.26\text{-}THMAMS\text{-}60^{o}C}$ (Table 5, entries 4 and 6, respectively) are an example of that, achieving higher conversions (from 45% at room temperature to 49% at 60 ^{o}C and from 63% to 72%, respectively) than their analogous experiments without temperature (i.e $G3_{P2\text{-}0.13\text{-}THMAMS}$ and $G3_{P2\text{-}0.26\text{-}THMAMS}$).

The type of crosslinker might also have played an important role in the catalysis reaction. According to Table 5, experiments $G3_{P2\text{-}0.13\text{-}TEA.OAc,}$ $G3_{P2\text{-}0.13\text{-}THMAMS,}$ and $G3_{P2\text{-}0.13\text{-}TEA.Cl}$ (entries 2, 3, and 7), all with the same crosslinker concentration but distinct IL-derivatives, resulted in conversions of 68%, 50%, and 48%, respectively. Even though acetate, sulfate, and chloride have different nucleophilicities, the conversion variation cannot be attributed to the anion substituent of the crosslinker, since no catalytic activity was observed without using TBA-Br as a co-catalyst. In fact, the bromide anion on the co-catalyst might have had a bigger influence on the ring-opening nucleophilic attack. Furthermore, this attack is more probable to be caused by the halide anion on the co-catalyst rather than by the IL-derivative anion, as the concentration of the former is much higher than the latter. Another hypothesis might be the effective crosslinking density possibly varying according to the type of crosslinker used, as reported previously in this work. This implies that, for the same theoretical crosslinker concentration of TEA.Cl, TEA.OAc or THMAMS (in this case, 0.13 wt%), we can have distinct effective crosslinkers concentration inside the beads. Consequently, even though one

TEA.OAc molecule possesses the same -OH groups as one TEA.Cl or THMAMS molecule, the former might have been able to interact and crosslink more effectively with our beads, remaining in a larger amount inside them than the other IL-derivatives. The SEM images of experiment $G3_{P2\text{-}0.13\text{-}TEA.OAc}$ also reflects this idea, as they depict a distinctive structure in comparison to experiments $G3_{P2\text{-}0.13\text{-}THMAMS}$ and $G3_{P2\text{-}0.13\text{-}TEA.Cl}$ (Figures B3.2, B3.3, and B3.5 e of the Appendix, respectively). Furthermore, this hypothesis can also be sustained by the catalytic activity of experiment $G2_{P1\text{-}1.2\text{-}0.1\text{-}Ø\text{-}t.but}$ (Table 5, entry 1), which had no crosslinker but was still able to achieve a similar conversion value (48%) compared with experiments $G3_{P2\text{-}0.13\text{-}THMAMS}$ and $G3_{P2\text{-}0.13\text{-}TEA.Cl}$, that had a crosslinker (45% and 48%, respectively). Thus, these results might be indicative that the IL-derivatives didn't crosslink effectively in the mentioned experiments. As a consequence, experiment $G3_{P2\text{-}0.13\text{-}TEA.OAc}$ might have had more hydrogen bond donors available than experiments $G3_{P2\text{-}0.13\text{-}THMAMS}$ and $G3_{P2\text{-}0.13\text{-}TEA.Cl}$, which led to higher conversion for the same reason proposed in the former paragraph. In addition, it should be also taken into account that the CO_2 sorption capacity of experiment $G3_{P2\text{-}0.13\text{-}TEA.OAc}$ might be superior to the other experiments, due to a potential stronger presence of the IL-derivative), which could have facilitated the CO_2 activation. Moreover, possible conformational changes caused by the TEA.OAc might have led to increased exposure and availability of hydrogen bond donors, as well CO_2–philic groups, which promote the epoxide and CO_2 activation processes.

Even though we were not able to test the influence of the quantity of catalyst due to experimental limitations, both type and quantity of catalyst have been reported to have an impact on the catalytic activity of the cycloaddition reaction [87]. Taheri et al. [38] varied the amount of IL@Chitosan catalyst used in the range of 100-200 mg to react with 8.73 mmol of styrene oxide at reaction conditions of 120 ^{o}C, 5h, and 20 bar of CO_2, highlighting that when using 100mg the conversion was only 77% with >99% selectivity. When it was increased to 150mg the conversion also increased to 98%, while the selectivity remained constant. However, a further increase to 200 mg led to a small decrease in the conversion to 96%. Similar conclusions were highlighted by Xiong et al. [86] reporting that a yield and selectivity of 75% were achieved by using 0.06 g of catalyst. An increase in both the yield and selectivity to 99% and >99%, respectively, when the amount was increased to 0.08 mg. But a decrease in both yield and selectivity when that limit value was exceeded. This was assigned to the fact that the excess catalyst was not well dispersed in the reaction mixture and thus was limiting the mass diffusion between active sites and reactants, which then reflects in the yield and selectivity of the reaction [90]. Liu et al. [41] measured the activities of distinct protonated amine in the coupling reaction of propylene oxide and CO_2 and reported increasing catalytic activity in terms of yield and selectivity when the anion substituent was I^- instead of F^-, Cl^- and Br^- anions and when TEA instead of MEA or DEA as the former was able to form more hydrogen bonds with the epoxide. In addition, Martínez-Ferraté et al.[37] equally tested the use of different amounts of 1-methyl-3-n-butylimidazolium halide (BMIm.X) ILs with commercial porous SiO_2 and reported that porosity favored the mass transfer and a catalytic performance increasing in the order of the anion substituent: $Cl^- < Br^- < I^-$.

The textural properties of our material might as well be a major factor influencing the catalytic activity. By increasing the surface area and/or the porosity of the catalyst, more active sites become available to adsorb the CO_2, promoting hence more contacts between the reactants, and resulting in an increment of the reaction rate and catalytic performance. As explained before in section 3.5, the synthesized beads might possess both meso- and macroporosity, and further studies in terms of pore size distribution would be required to assess the influence of the porosity in the catalytic activity. Despite that, as shown also in Table 4 from that section, the surface area changes depending on the crosslinker used. The surface area of experiments $G2_{P1\text{-}1.2\text{-}0.1\text{-}Ø\text{-}t.but}$, $G3_{P2\text{-}0.13\text{-}THMAMS}$, and $G3_{P2\text{-}0.13\text{-}TEA.Cl}$ is comparable, which possibly contributes to their similar lower catalytic activity. Oppositely, experiments $G3_{P2\text{-}0.26\text{-}THMAMS}$ and $G3_{P2\text{-}0.26\text{-}THMAMS}$-60ºC possess higher surface areas, which might have led to increased catalytic activity. Furthermore, we suppose that the beads from experiment $G3_{P2\text{-}0.13\text{-}TEA.OAc}$ used in the catalysis test (see Table I.1 from the Appendix) had a higher surface and was more porous too, as this experiment achieved one of the highest conversions (69%) under 4h at 80ºC and 5 bar. However, this might be just a possibility, as the catalytic performance depends on a balance between surface area, porosity, and effective IL-derivative concentration inside the beads.

Notably, despite the beads from experiment $G3_{P2\text{-}0.13\text{-}TEA.OAc}$ showed improved conversion in comparison to the beads from experiment $G3_{P2\text{-}0.26\text{-}THMAMS}$ at the reaction conditions described in Table 5, by analyzing Figure 16 it is possible to observe that the latter exhibited better selectivity and conversion than the former. We suspect that the reaction kinetics are faster when using experiment $G3_{P2\text{-}0.13\text{-}TEA.OAc}$ as a catalyst than experiment $G3_{P2\text{-}0.26\text{-}THMAMS}$, resulting in higher conversion during the first hours. However, along the time the beads from the latter experiment promote a larger conversion increment than the former, achieving a higher conversion maximum as well.

Lastly, despite the reaction mechanism of cyclic carbonates synthesis assisted by IL-based catalysts having already been addressed in the literature [85], [91], [92], we can propose a similar mechanism pathway with the following steps based on our results:

i) Epoxide activation by interaction hydrogen bond donor groups (–OH, –COOH,–NH_2) present in the catalyst with an oxygen atom of the epoxide via hydrogen bonding;

ii) Ring-opening of activated epoxide by the nucleophilic attack of the co-catalyst (TBA-Br) anion, as no catalytic activity was detected in the absence of a co-catalyst. The Br attack occurs on the less hindered carbon atom of the epoxide to form an oxy-anion species (alkoxide intermediate). The stability of this ring-opened epoxide is provided by the counter cation and also by the H-bond species;

iii) The subsequent CO_2 insertion is achieved by a nucleophilic attack of negatively charged oxygen (oxy-anion) on an electrophilic carbon atom of CO_2 to form a carbonate intermediate. Porosity and CO_2-philic groups (for instance, –NH_2) present in the catalyst could facilitate the sorption and activation of CO_2 to reduce the energy barrier;

iv) The resulting open-chain carbonate further undergoes intramolecular cyclic elimination and finally, a five-membered cyclic carbonate is formed by the displacement of the nucleophile, being the catalyst and co-catalyst regenerated.

4. CONCLUSIONS

In this work, a chitosan@IL-derived composite material was developed to face the CO_2 capture and conversion barriers, namely the costs and efficiency of these processes. Through polyelectrolyte complexation and freeze-drying methodologies, we were able to produce porous cryogel beads. Several experimental parameters have been varied across three generations, namely: CHI, SPA, crosslinker and NaOH concentrations, solvent and crosslinker type, the process of introducing the crosslinker, as well the syringe tip diameter, to study their effects on the beads' morphology, and consequently on their CO_2 capture capacity and catalytic activity. SEM and BET analysis was performed to evaluate the beads' textural properties, while FTIR and NMR spectrometry were acquired to analyze the beads and crosslinker's structure. Furthermore, FTIR measurements were also used to assess the CO_2 capture capacity qualitatively, while NMR allowed additionally the evaluation of the beads' catalytic activity in the cycloaddition reaction of CO_2 to styrene oxide to produce styrene carbonate. The data obtained shows the chitosan@IL-derived beads might have been able to capture CO_2 under environmental conditions (1 bar, 20^{o}C), and that when using the beads as a catalyst in the cycloaddition reaction, it was possible to achieve a conversion of 72% and a selectivity >99%, in just 4h at a CO_2 pressure of 5 bar, temperature of 80^{o}C and in the presence of TBA.Br as co-catalyst. Indeed, the results achieved show that the introduction of IL-derivatives inside the beads improved their CO_2 capture capacity and catalytic activity, possibly due to the addition of CO_2-philic groups and morphological changes caused by these materials.

The present thesis not only gives new insights about the factors affecting the synthetic routes used to prepare the beads but also opens new opportunities to control and develop new materials with optimized performance in CO_2 capture and conversion. Furthermore, we anticipate that in future works it would be interesting to try to introduce higher concentrations of IL-derivatives in the CHI beads, evaluate how that concentration impacts their properties as well to study quantitatively the CO_2 capture capacity of the beads. Lastly, it would be also relevant to optimize the catalysis conditions and to test the recyclability of these catalysts, in order to access if these materials would be efficiently and economically viable to apply at industrial levels.

5. BIBLIOGRAPHY

[1] M. Aghaie, N. Rezaei, and S. Zendehboudi, "A systematic review on CO2 capture with ionic liquids: Current status and future prospects," *Renew. Sustain. Energy Rev.*, vol. 96, no. December 2017, pp. 502–525, 2018, doi: 10.1016/j.rser.2018.07.004.

[2] W. Gao *et al.*, "Industrial carbon dioxide capture and utilization: state of the art and future challenges," *Chem. Soc. Rev.*, 2020, doi: 10.1039/d0cs00025f.

[3] A. Al-Mamoori, A. Krishnamurthy, A. A. Rownaghi, and F. Rezaei, "Carbon Capture and Utilization Update," *Energy Technol.*, vol. 5, no. 6, pp. 834–849, 2017, doi: 10.1002/ente.201600747.

[4] S. Zulfiqar, M. I. Sarwar, and D. Mecerreyes, "Polymeric ionic liquids for CO2 capture and separation: Potential, progress and challenges," *Polym. Chem.*, vol. 6, no. 36, pp. 6435–6451, 2015, doi: 10.1039/c5py00842e.

[5] D. Y. C. Leung, G. Caramanna, and M. M. Maroto-Valer, *An overview of current status of carbon dioxide capture and storage technologies*, vol. 39. Elsevier, 2014.

[6] T. Newholm, A. Laing, and G. Hogg, *Polymerized Ionic Liquids*, vol. 40, no. 9–10. 2017.

[7] N. M. Simon, M. Zanatta, F. P. dos Santos, M. C. Corvo, E. J. Cabrita, and J. Dupont, "Carbon Dioxide Capture by Aqueous Ionic Liquid Solutions," *ChemSusChem*, vol. 10, no. 24, pp. 4927–4933, 2017, doi: 10.1002/cssc.201701044.

[8] S. K. Shukla, S. G. Khokarale, T. Q. Bui, and J. P. T. Mikkola, "Ionic liquids: Potential materials for carbon dioxide capture and utilization," *Front. Mater.*, vol. 6, no. March, pp. 1–8, 2019, doi: 10.3389/fmats.2019.00042.

[9] R. L. Vekariya, "A review of ionic liquids: Applications towards catalytic organic transformations," *J. Mol. Liq.*, vol. 227, p. 44, 2017, doi: 10.1016/j.molliq.2016.11.123.

[10] M. Zanatta, M. Lopes, E. J. Cabrita, C. E. S. Bernardes, and M. C. Corvo, "Handling CO2sorption mechanism in PIL@IL composites," *J. CO2 Util.*, vol. 41, no. June, p. 101225, 2020, doi: 10.1016/j.jcou.2020.101225.

[11] X. Zhang, X. Zhang, H. Dong, Z. Zhao, S. Zhang, and Y. Huang, "Carbon capture with ionic liquids: Overview and progress," *Energy Environ. Sci.*, vol. 5, no. 5, pp. 6668–6681, 2012, doi: 10.1039/c2ee21152a.

[12] C. H. Yu, C. H. Huang, and C. S. Tan, "A review of CO2 capture by absorption and adsorption," *Aerosol Air Qual. Res.*, vol. 12, no. 5, pp. 745–769, 2012, doi: 10.4209/aaqr.2012.05.0132.

[13] F. Yang *et al.*, "Understanding CO2 capture kinetics and energetics by ionic liquids with molecular dynamics simulation," *RSC Adv.*, vol. 10, no. 24, pp. 13968–13974, 2020, doi: 10.1039/d0ra02221g.

[14] E. Torralba-Calleja, J. Skinner, and D. Gutiérrez-Tauste, "CO2 capture in ionic liquids: A review of solubilities and experimental methods," *J. Chem.*, vol. 2013, 2013, doi: 10.1155/2013/473584.

[15] J. H. Davis, E. D. Bates, and R. A. Dayton, "CO2 capture by a task-specific ionic liquid," *J. Am. Chem. Soc.*, vol. 124, pp. 926–927, 2002.

[16] R. V Barrulas, M. Zanatta, T. Casimiro, and M. C. Corvo, "Advanced Porous Materials from Poly(ionic liquid)s: Challenges, Applications and Opportunities," *Chem. Eng. J.*,

p. 128528, 2021, doi: 10.1016/j.cej.2021.128528.
[17] N. Hedin, L. Andersson, L. Bergström, and J. Yan, "Adsorbents for the post-combustion capture of CO2 using rapid temperature swing or vacuum swing adsorption," *Appl. Energy*, vol. 104, pp. 418–433, 2013, doi: 10.1016/j.apenergy.2012.11.034.
[18] F. P. Kinik, A. Uzun, and S. Keskin, "Ionic Liquid/Metal–Organic Framework Composites: From Synthesis to Applications," *ChemSusChem*, vol. 10, no. 14, pp. 2842–2863, 2017, doi: 10.1002/cssc.201700716.
[19] M. Li *et al.*, "Pebax-based composite membranes with high gas transport properties enhanced by ionic liquids for CO2 separation," *RSC Adv.*, vol. 7, no. 11, pp. 6422–6431, 2017, doi: 10.1039/c6ra27221e.
[20] D. Nikolaeva and P. Luis, "Top-down polyelectrolytes for membrane-based post-combustion CO2 capture," *Molecules*, vol. 25, no. 2, 2020, doi: 10.3390/molecules25020323.
[21] S. Y. Zhang *et al.*, "Poly(ionic liquid) composites," *Chem. Soc. Rev.*, vol. 49, no. 6, pp. 1726–1755, 2020, doi: 10.1039/c8cs00938d.
[22] J. Tang, H. Tang, W. Sun, M. Radosz, and Y. Shen, "Poly(ionic liquid)s as new materials for CO 2 absorption," *J. Polym. Sci. Part A Polym. Chem.*, vol. 43, no. 22, pp. 5477–5489, 2005, doi: 10.1002/pola.21031.
[23] J. Tang, H. Tang, W. Sun, M. Radosz, and Y. Shen, "Low-pressure CO2 sorption in ammonium-based poly(ionic liquid)s," *Polymer (Guildf).*, vol. 46, no. 26, pp. 12460–12467, 2005, doi: 10.1016/j.polymer.2005.10.082.
[24] Y. Shen, M. Radosz, J. Tang, and W. Sun, "Isothermal carbon dioxide sorption in poly(ionic liquid)s," *AIChE Annu. Meet. Conf. Proc.*, no. 30 mL, pp. 9113–9118, 2009.
[25] Y. B. Xiong, H. Wang, Y. J. Wang, and R. M. Wang, "Novel imidazolium-based poly(ionic liquid)s: Preparation, characterization, and absorption of CO 2," *Polym. Adv. Technol.*, vol. 23, no. 5, pp. 835–840, 2012, doi: 10.1002/pat.1973.
[26] J. Tang, H. Tang, W. Sun, H. Plancher, M. Radosz, and Y. Shen, "Poly(ionic liquid)s: A new material with enhanced and fast CO2 absorption," *Chem. Commun.*, no. 26, pp. 3325–3327, 2005, doi: 10.1039/b501940k.
[27] M. Sadeghpour, R. Yusoff, and M. K. Aroua, "Polymeric ionic liquids (PILs) for CO2 capture," *Rev. Chem. Eng.*, vol. 33, no. 2, pp. 183–200, 2017, doi: 10.1515/revce-2015-0070.
[28] A. Wilke, J. Yuan, M. Antonietti, and J. Weber, "Enhanced carbon dioxide adsorption by a mesoporous poly(ionic liquid)," *ACS Macro Lett.*, vol. 1, no. 8, pp. 1028–1031, 2012, doi: 10.1021/mz3003352.
[29] H. Lin, S. Zhang, J. K. Sun, M. Antonietti, and J. Yuan, "Poly(ionic liquid)s with engineered nanopores for energy and environmental applications," *Polymer (Guildf).*, vol. 202, no. April, p. 122640, 2020, doi: 10.1016/j.polymer.2020.122640.
[30] J. Yuan, D. Mecerreyes, and M. Antonietti, *Poly(ionic liquid)s: An update*, vol. 38, no. 7. Elsevier Ltd, 2013.
[31] D. M. Rodrigues, L. G. Hunter, F. L. Bernard, M. F. Rojas, F. Dalla Vecchia, and S. Einloft, "Harnessing CO 2 into Carbonates Using Heterogeneous Waste Derivative Cellulose-Based Poly(ionic liquids) as Catalysts," *Catal. Letters*, vol. 149, no. 3, pp. 733–743, 2019, doi: 10.1007/s10562-018-2637-4.
[32] P. P. Pescarmona and M. Taherimehr, "Challenges in the catalytic synthesis of cyclic and polymeric carbonates from epoxides and CO2," *Catal. Sci. Technol.*, vol. 2, no. 11, pp. 2169–2187, 2012, doi: 10.1039/c2cy20365k.
[33] S. C. Stouten, T. Noël, Q. Wang, and V. Hessel, "Catalyst retention in continuous flow

with supercritical carbon dioxide," *Chem. Eng. Process. Process Intensif.*, vol. 83, pp. 26–32, 2014, doi: 10.1016/j.cep.2014.03.017.

[34] X. Wang *et al.*, "Heterogeneous conversion of CO2 into cyclic carbonates at ambient pressure catalyzed by ionothermal-derived meso-macroporous hierarchical poly(ionic liquid)s," *Chem. Sci.*, vol. 6, no. 12, pp. 6916–6924, 2015, doi: 10.1039/c5sc02050f.

[35] J. Peng and Y. Deng, "Cycloaddition of carbon dioxide to propylene oxide catalyzed by ionic liquids," *New J. Chem.*, vol. 25, no. 4, pp. 639–641, 2001, doi: 10.1039/b008923k.

[36] M. F. Rojas *et al.*, "Poly(ionic liquid)s as efficient catalyst in transformation of CO 2 to cyclic carbonate," *J. Mol. Catal. A Chem.*, vol. 392, pp. 83–88, 2014, doi: 10.1016/j.molcata.2014.05.007.

[37] O. Martínez-Ferraté, G. Chacón, F. Bernardi, T. Grehl, P. Brüner, and J. Dupont, "Cycloaddition of carbon dioxide to epoxides catalysed by supported ionic liquids," *Catal. Sci. Technol.*, vol. 8, no. 12, pp. 3081–3089, 2018, doi: 10.1039/c8cy00749g.

[38] M. Taheri, M. Ghiaci, and A. Shchukarev, "Cross-linked chitosan with a dicationic ionic liquid as a recyclable biopolymer-supported catalyst for cycloaddition of carbon dioxide with epoxides into cyclic carbonates," *New J. Chem.*, vol. 42, no. 1, pp. 587–597, 2018, doi: 10.1039/c7nj03665e.

[39] S. Kumar, K. Prasad, J. M. Gil, A. J. F. N. Sobral, and J. Koh, "Mesoporous zeolite-chitosan composite for enhanced capture and catalytic activity in chemical fixation of CO2," *Carbohydr. Polym.*, vol. 198, pp. 401–406, 2018, doi: 10.1016/j.carbpol.2018.06.100.

[40] M. Lee, B. Y. Chen, and W. Den, "Chitosan as a natural polymer for heterogeneous catalysts support: A short review on its applications," *Appl. Sci.*, vol. 5, no. 4, pp. 1272–1283, 2015, doi: 10.3390/app5041272.

[41] M. Liu, X. Li, L. Liang, and J. Sun, "Protonated triethanolamine as multi-hydrogen bond donors catalyst for efficient cycloaddition of CO2 to epoxides under mild and cocatalyst-free conditions," *J. CO2 Util.*, vol. 16, pp. 384–390, 2016, doi: 10.1016/j.jcou.2016.10.004.

[42] K. Ito and H. J. Bernstein, "the Vibrational Spectra of the Formate, Acetate, and Oxalate Ions," *Can. J. Chem.*, vol. 34, no. 2, pp. 170–178, 1956, doi: 10.1139/v56-021.

[43] R. Ur Rehman *et al.*, "Development of ethanolamine-based ionic liquid membranes for efficient CO2/CH4 separation," *J. Appl. Polym. Sci.*, vol. 134, no. 44, pp. 1–11, 2017, doi: 10.1002/app.45395.

[44] A. Q. Wang and T. D. Golden, "Electrodeposition of Oriented Cerium Oxide Films," *Int. J. Electrochem.*, vol. 2013, pp. 1–10, 2013, doi: 10.1155/2013/482187.

[45] M. G. Voronkov *et al.*, "Tris(2-hydroxyethyl)ammonium salts: 2,8,9-Trihydroprotatranes," *Russ. J. Gen. Chem.*, vol. 79, no. 11, pp. 2339–2346, 2009, doi: 10.1134/S1070363209110097.

[46] V. S. Meka, M. K. G. Sing, M. R. Pichika, S. R. Nali, V. R. M. Kolapalli, and P. Kesharwani, "A comprehensive review on polyelectrolyte complexes," *Drug Discov. Today*, vol. 22, no. 11, pp. 1697–1706, 2017, doi: 10.1016/j.drudis.2017.06.008.

[47] B. P. Das and M. Tsianou, "From polyelectrolyte complexes to polyelectrolyte multilayers: Electrostatic assembly, nanostructure, dynamics, and functional properties," *Adv. Colloid Interface Sci.*, vol. 244, pp. 71–89, 2017, doi: 10.1016/j.cis.2016.12.004.

[48] J. van der Gucht, E. Spruijt, M. Lemmers, and M. A. Cohen Stuart, "Polyelectrolyte complexes: Bulk phases and colloidal systems," *J. Colloid Interface Sci.*, vol. 361, no. 2, pp. 407–422, 2011, doi: 10.1016/j.jcis.2011.05.080.

[49] I. Prigogine, *Advances in Chemical Physics*, vol. 5. 2007.
[50] L. Qian and H. Zhang, "Controlled freezing and freeze drying: A versatile route for porous and micro-/nano-structured materials," *J. Chem. Technol. Biotechnol.*, vol. 86, no. 2, pp. 172–184, 2011, doi: 10.1002/jctb.2495.
[51] D. Filion, M. Lavertu, and M. D. Buschmann, "Ionization and solubility of chitosan solutions related to thermosensitive chitosan/glycerol-phosphate systems," *Biomacromolecules*, vol. 8, no. 10, pp. 3224–3234, 2007, doi: 10.1021/bm700520m.
[52] H. V. Sæther, H. K. Holme, G. Maurstad, O. Smidsrød, and B. T. Stokke, "Polyelectrolyte complex formation using alginate and chitosan," *Carbohydr. Polym.*, vol. 74, no. 4, pp. 813–821, 2008, doi: 10.1016/j.carbpol.2008.04.048.
[53] V. Chavasit, C. Kienzle-Sterzer, and J. Antonio Torres, "Formation and characterization of an insoluble polyelectrolyte complex: Chitosan-polyacrylic acid," *Polym. Bull.*, vol. 19, no. 3, pp. 223–230, 1988, doi: 10.1007/BF00255376.
[54] A. D. Kulkarni *et al.*, "Polyelectrolyte complexes: mechanisms, critical experimental aspects, and applications," *Artif. Cells, Nanomedicine Biotechnol.*, vol. 44, no. 7, pp. 1615–1625, 2016, doi: 10.3109/21691401.2015.1129624.
[55] J. Koetz and S. Kosmella, *Polyelectrolytes and Nanoparticles*. 2007.
[56] B. Vishalakshi, S. Ghosh, and V. Kalpagam, "The effects of charge density and concentration on the composition of polyelectrolyte complexes," *Polymer (Guildf).*, vol. 34, no. 15, pp. 3270–3275, 1993, doi: 10.1016/0032-3861(93)90401-U.
[57] T. Takahashi, K. Takayama, Y. Machida, and T. Nagai, "Characteristics of polyion complexes of chitosan with sodium alginate and sodium polyacrylate," *Int. J. Pharm.*, vol. 61, no. 1–2, pp. 35–41, 1990, doi: 10.1016/0378-5173(90)90041-2.
[58] J. Berger, M. Reist, J. M. Mayer, O. Felt, N. A. Peppas, and R. Gurny, "Structure and interactions in covalently and ionically crosslinked chitosan hydrogels for biomedical applications," *Eur. J. Pharm. Biopharm.*, vol. 57, no. 1, pp. 19–34, 2004, doi: 10.1016/S0939-6411(03)00161-9.
[59] A. OU and I. BO, "Chitosan Hydrogels and their Glutaraldehyde-Crosslinked Counterparts as Potential Drug Release and Tissue Engineering Systems - Synthesis, Characterization, Swelling Kinetics and Mechanism," *J. Phys. Chem. Biophys.*, vol. 07, no. 03, 2017, doi: 10.4172/2161-0398.1000256.
[60] P. Smrdel, M. Bogataj, and A. Mrhar, "The influence of selected parameters on the size and shape of alginate beads prepared by ionotropic gelation," *Sci. Pharm.*, vol. 76, no. 1, pp. 77–89, 2008, doi: 10.3797/scipharm.0611-07.
[61] T. I. Klokk and J. E. Melvik, "Controlling the size of alginate gel beads by use of a high electrostatic potential," *J. Microencapsul.*, vol. 19, no. 4, pp. 415–424, 2002, doi: 10.1080/02652040210144234.
[62] T. Sakiyama, C. -H Chu, T. Fujii, and T. Yano, "Preparation of a polyelectrolyte complex gel from chitosan and κ-carrageenan and its pH-sensitive swelling," *J. Appl. Polym. Sci.*, vol. 50, no. 11, pp. 2021–2025, 1993, doi: 10.1002/app.1993.070501121.
[63] R. Subrahmanyam, P. Gurikov, P. Dieringer, M. Sun, and I. Smirnova, "On the Road to Biopolymer Aerogels—Dealing with the Solvent," *Gels*, vol. 1, no. 2, pp. 291–313, 2015, doi: 10.3390/gels1020291.
[64] D. H. Lee, M. J. Jo, S. W. Han, S. Yu, and H. Park, "Polyimide aerogel with controlled porosity: Solvent-induced synergistic pore development during solvent exchange process," *Polymer (Guildf).*, vol. 205, no. August, p. 122879, 2020, doi: 10.1016/j.polymer.2020.122879.

[65] S. Takeshita, A. Sadeghpour, D. Sivaraman, S. Zhao, and W. J. Malfait, "Solvents, CO2 and biopolymers: Structure formation in chitosan aerogel," *Carbohydr. Polym.*, vol. 247, no. May, p. 116680, 2020, doi: 10.1016/j.carbpol.2020.116680.

[66] C. Reichardt and T. Welton, *Solvents and Solvent Effects in Organic Chemistry*. Weinheim, Germany: Wiley-VCH Verlag GmbH & Co. KGaA, 2010.

[67] M. Prostredný, M. Abduljalil, P. Mulheran, and A. Fletcher, "Process Variable Optimization in the Manufacture of Resorcinol–Formaldehyde Gel Materials," *Gels*, vol. 4, no. 2, p. 36, 2018, doi: 10.3390/gels4020036.

[68] H. Tamon, H. Ishizaka, T. Yamamoto, and T. Suzuki, "Influence of freeze-drying conditions on the mesoporosity of organic gels as carbon precursors," *Carbon N. Y.*, vol. 38, no. 7, pp. 1099–1105, 2000, doi: 10.1016/S0008-6223(99)00235-3.

[69] C. Kunz, S. Schuldt-Lieb, and H. Gieseler, "Freeze-Drying From Organic Co-Solvent Systems, Part 2: Process Modifications to Reduce Residual Solvent Levels and Improve Product Quality Attributes," *J. Pharm. Sci.*, vol. 108, no. 1, pp. 399–415, 2019, doi: 10.1016/j.xphs.2018.07.002.

[70] K. C. S. Figueiredo, T. L. M. Alves, and C. P. Borges, "Poly(vinyl alcohol) films crosslinked by glutaraldehyde under mild conditions," *J. Appl. Polym. Sci.*, vol. 111, no. 6, pp. 3074–3080, Jan. 2009, doi: 10.1002/app.29263.

[71] G. Hoti *et al.*, "Effect of the cross-linking density on the swelling and rheological behavior of ester-bridged β-cyclodextrin nanosponges," *Materials (Basel).*, vol. 14, no. 3, pp. 1–20, 2021, doi: 10.3390/ma14030478.

[72] N. Islam, I. Dmour, and M. O. Taha, "Degradability of chitosan micro/nanoparticles for pulmonary drug delivery," *Heliyon*, vol. 5, no. 5, p. e01684, 2019, doi: 10.1016/j.heliyon.2019.e01684.

[73] M. Thommes *et al.*, "Physisorption of gases, with special reference to the evaluation of surface area and pore size distribution (IUPAC Technical Report)," *Pure Appl. Chem.*, vol. 87, no. 9–10, pp. 1051–1069, 2015, doi: 10.1515/pac-2014-1117.

[74] Z. A. Sutirman, M. M. Sanagi, K. J. Abd Karim, and W. A. Wan Ibrahim, "Preparation of methacrylamide-functionalized crosslinked chitosan by free radical polymerization for the removal of lead ions," *Carbohydr. Polym.*, vol. 151, no. July, pp. 1091–1099, 2016, doi: 10.1016/j.carbpol.2016.06.076.

[75] N. Islam, H. Wang, F. Maqbool, and V. Ferro, "In vitro enzymatic digestibility of glutaraldehyde-crosslinked chitosan nanoparticles in lysozyme solution and their applicability in pulmonary drug delivery," *Molecules*, vol. 24, no. 7, pp. 1–17, 2019, doi: 10.3390/molecules24071271.

[76] E. H. Mejía, H. Contreras, E. Delgado, and G. Quintana, "Effect of Experimental Parameters on the Formation of Hydrogels by Polyelectrolyte Complexation of Carboxymethylcellulose, Carboxymethyl Starch, and Alginic Acid with Chitosan," *Int. J. Chem. Eng.*, vol. 2019, 2019, doi: 10.1155/2019/3085691.

[77] B. Grabowska and M. Holtzer, "Structural examination of the cross-linking reaction mechanism of polyacrylate binding agents," *Arch. Metall. Mater.*, vol. 54, no. 2, pp. 427–437, 2009.

[78] H. Ortega-Ortiz, B. Gutiérrez-Rodríguez, G. Cadenas-Pliego, and L. I. Jimenez, "Antibacterial activity of chitosan and the interpolyelectrolyte complexes of poly(acrylic acid)-chitosan," *Brazilian Arch. Biol. Technol.*, vol. 53, no. 3, pp. 623–628, 2010, doi: 10.1590/S1516-89132010000300016.

[79] S. Cukrowicz *et al.*, "Organobentonites modified with poly(Acrylic acid) and its sodium

salt for foundry applications," *Materials (Basel).*, vol. 14, no. 8, pp. 1–18, 2021, doi: 10.3390/ma14081947.

[80] G. Richner and G. Puxty, "Assessing the chemical speciation during CO 2 absorption by aqueous amines using in situ FTIR," *Ind. Eng. Chem. Res.*, vol. 51, no. 44, pp. 14317–14324, 2012, doi: 10.1021/ie302056f.

[81] P. Jackson, K. Robinson, G. Puxty, and M. Atalla, "In situ Fourier Transform-Infrared (FT-IR) analysis of carbon dioxide absorption and desorption in amine solutions," *Energy Procedia*, vol. 1, pp. 985–994, 2009.

[82] C. F. Martins *et al.*, "Modelling CO2 absorption in aqueous solutions of cholinium lysinate ionic liquid," *Chem. Eng. J.*, vol. 421, p. 127875, 2021, doi: 10.1016/j.cej.2020.127875.

[83] Y. Mergler, R. Rumley-Van Gurp, P. Brasser, M. De Koning, and E. Goetheer, "Solvents for CO2 capture. Structure-activity relationships combined with vapour-liquid-equilibrium measurements," *Energy Procedia*, vol. 4, no. February 2015, pp. 259–266, 2011, doi: 10.1016/j.egypro.2011.01.050.

[84] W. Clegg, R. W. Harrington, M. North, and R. Pasquale, "Cyclic carbonate synthesis catalysed by bimetallic aluminium-salen complexes," *Chem. - A Eur. J.*, vol. 16, no. 23, pp. 6828–6843, 2010, doi: 10.1002/chem.201000030.

[85] A. Rehman, F. Saleem, F. Javed, A. Ikhlaq, S. W. Ahmad, and A. Harvey, "Recent advances in the synthesis of cyclic carbonates via CO2cycloaddition to epoxides," *J. Environ. Chem. Eng.*, vol. 9, no. 2, p. 105113, 2021, doi: 10.1016/j.jece.2021.105113.

[86] Y. Xiong, F. Bai, Z. Cui, N. Guo, and R. Wang, "Cycloaddition Reaction of Carbon Dioxide to Epoxides Catalyzed by Polymer-Supported Quaternary Phosphonium Salts," vol. 2013, 2013.

[87] A. I. Adeleye, "Heterogeneous Catalytic Conversion of Carbon Dioxide to Value Added Chemicals," 2015.

[88] K. Kiatkittipong *et al.*, "Green pathway in utilizing CO2 via cycloaddition reaction with epoxide-A mini review," *Processes*, vol. 8, no. 5, 2020, doi: 10.3390/PR8050548.

[89] P. B. Webb, M. F. Sellin, T. E. Kunene, S. Williamson, A. M. Z. Slawin, and D. J. Cole-Hamilton, "Continuous Flow Hydroformylation of Alkenes in Supercritical Fluid-Ionic Liquid Biphasic Systems," *J. Am. Chem. Soc.*, vol. 125, no. 50, pp. 15577–15588, 2003, doi: 10.1021/ja035967s.

[90] Y. Zhou, S. Hu, X. Ma, S. Liang, T. Jiang, and B. Han, "Synthesis of cyclic carbonates from carbon dioxide and epoxides over betaine-based catalysts," *J. Mol. Catal. A Chem.*, vol. 284, no. 1–2, pp. 52–57, 2008, doi: 10.1016/j.molcata.2008.01.010.

[91] X. Zhou, J. Weber, and J. Yuan, "Poly(ionic liquid)s: Platform for CO2 capture and catalysis," *Curr. Opin. Green Sustain. Chem.*, vol. 16, pp. 39–46, 2019, doi: 10.1016/j.cogsc.2018.11.014.

[92] F. Zhang, Y. Wang, X. Zhang, X. Zhang, H. Liu, and B. Han, "Recent advances in the coupling of CO2 and epoxides into cyclic carbonates under halogen-free condition," *Green Chem. Eng.*, vol. 1, no. 2, pp. 82–93, 2020, doi: 10.1016/j.gce.2020.09.008.

6. APPENDIX

A – Formation of beads

A1 – 1st Generation

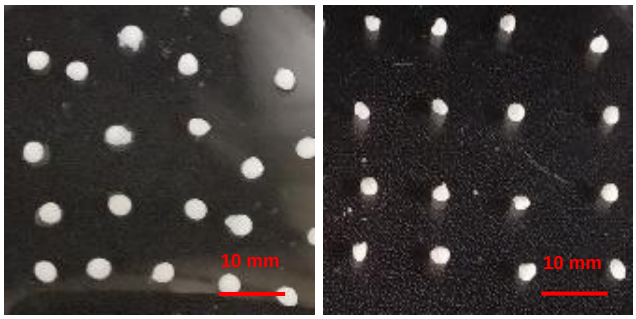

Figure A1.1 - Experiment G1 $_{1\text{-}1\text{-}Ø\text{-}0.32}$ (entry 1), hydrogel and alcohol gel, respectively

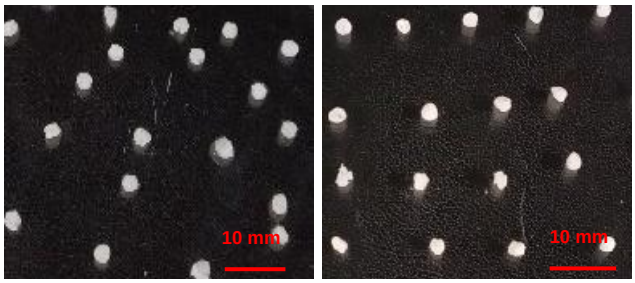

Figure A1.2 – Experiment G1$_{1\text{-}1\text{-}CHI\text{-}0.32}$ (entry 2), hydrogel and alcohol gel, respectively

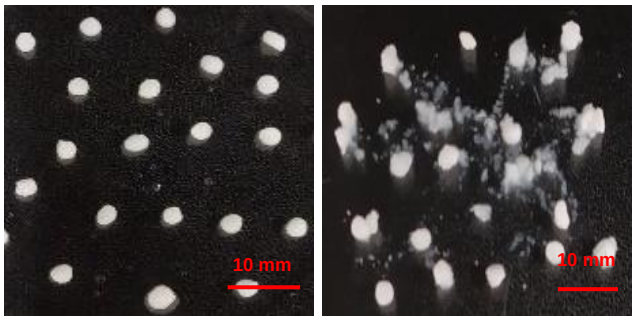

Figure A1.3 – Experiment G1$_{1\text{-}2\text{-}Ø\text{-}0.32}$ (entry 3), hydrogel and alcohol gel, respectively

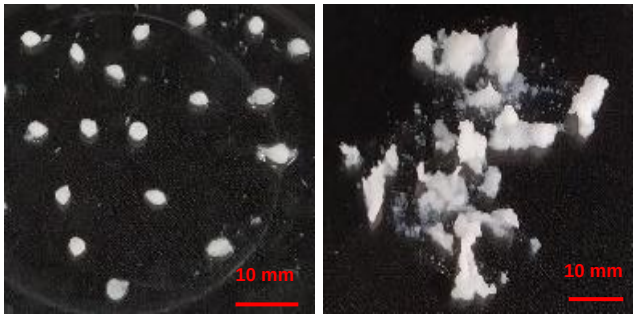

Figure A1.4 – Experiment G1$_{1\text{-}2\text{-}CHI\text{-}0.32}$ (entry 4), hydrogel and alcohol gel, respectively

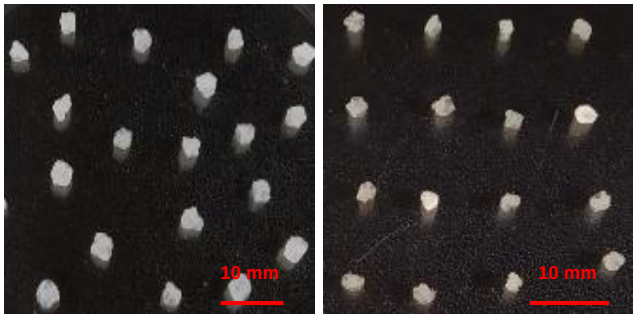

Figure A1.5 – Experiment $G1_{2.5\text{-}1\text{-}Ø\text{-}0.32}$ (entry 5), hydrogel and alcohol gel, respectively

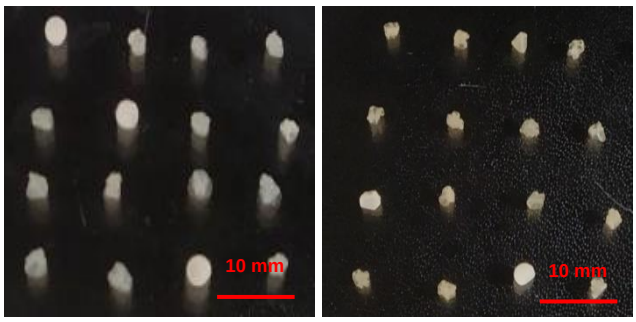

Figure A1.6 – Experiment $G1_{2.5\text{-}1\text{-}CHI\text{-}0.32}$ (entry 6), hydrogel and alcohol gel, respectively

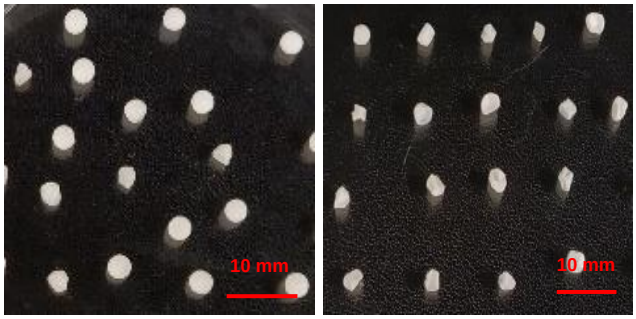

Figure A1.7 – Experiment $G1_{2.5\text{-}2\text{-}Ø\text{-}0.32}$ (entry 7), hydrogel and alcohol gel, respectively

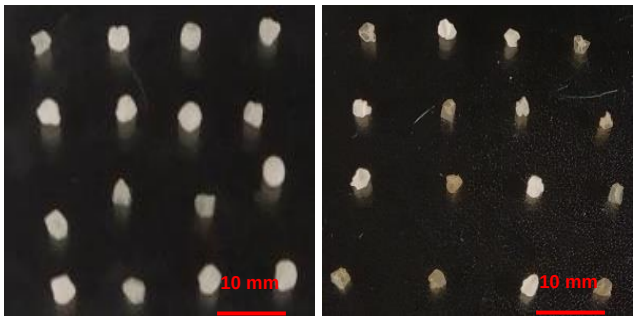

Figure A1.8 – Experiment $G1_{2.5\text{-}2\text{-}CHI\text{-}0.32}$ (entry 8), hydrogel and alcohol gel, respectively

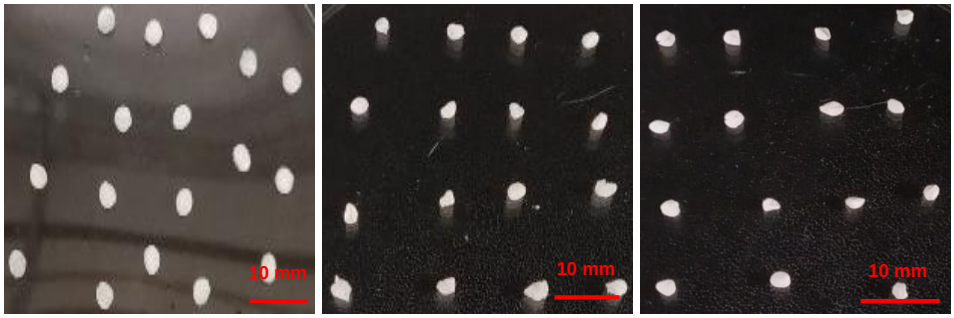

Figure A1.9 – Experiment $G1_{1\text{-}1\text{-}Ø\text{-}0.65}$ (entry 9), hydrogel, alcohol gel, and cryogel respectively

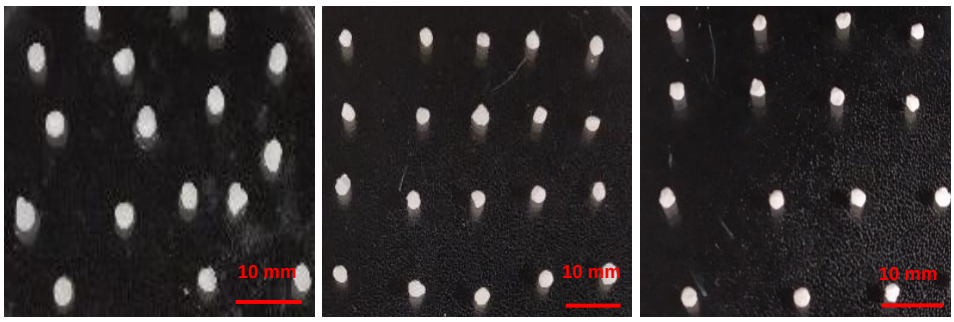

Figure A1.10 – Experiment $G1_{1\text{-}1\text{-}CHI\text{-}0.65}$ (entry 10), hydrogel, alcohol gel, and cryogel respectively

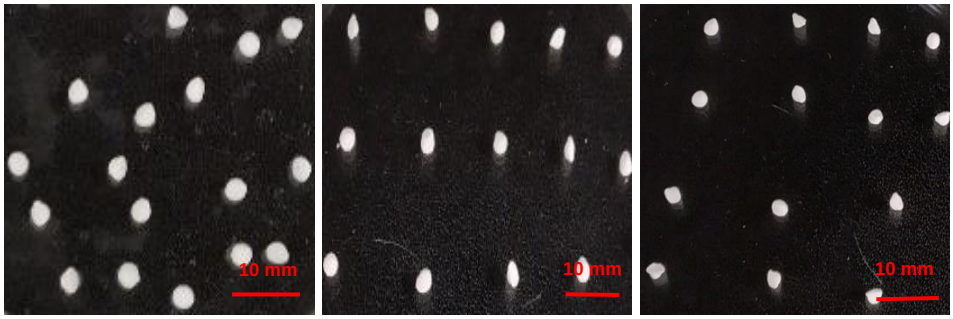

Figure A1.11 – Experiment $G1_{1\text{-}2\text{-}Ø\text{-}0.65}$ (entry 11), hydrogel, alcohol gel, and cryogel respectively

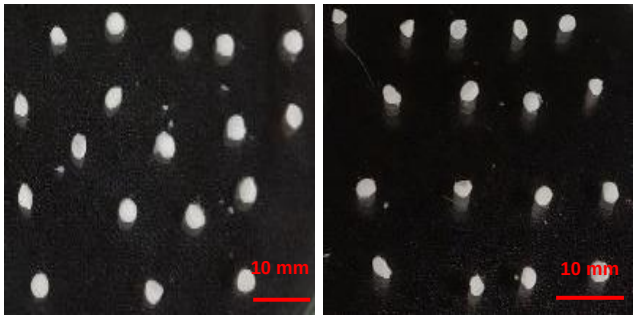

Figure A1.12 – Experiment $G1_{1\text{-}2\text{-}CHI\text{-}0.65}$ (entry 12), hydrogel and alcohol gel, respectively

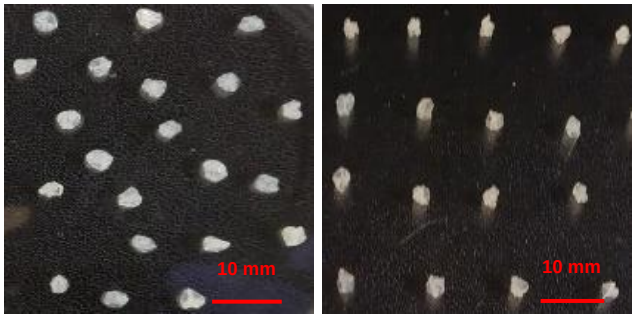

Figure A1.13 - Experiment $G1_{2.5\text{-}1\text{-}Ø\text{-}0.65}$ (entry 13), hydrogel and alcohol gel, respectively

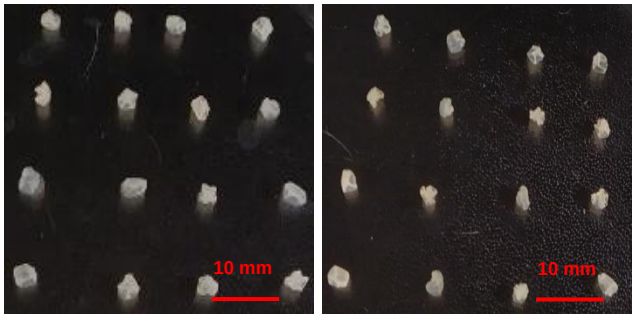

Figure A1.14 – Experiment $G_{12.5\text{-}1\text{-}CHI\text{-}0.65}$ (entry 14), hydrogel and alcohol gel, respectively

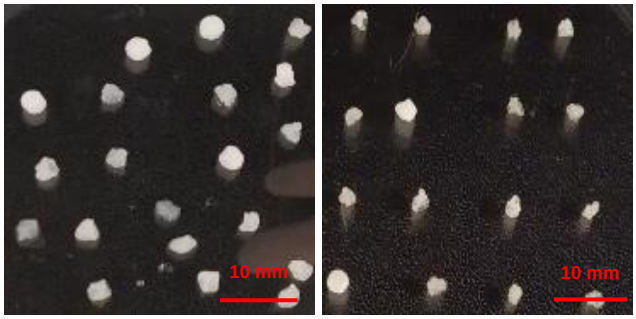

Figure A1.15 - Experiment $G1_{2.5\text{-}2\text{-}Ø\text{-}0.65}$ (entry 15), hydrogel and alcohol gel, respectively

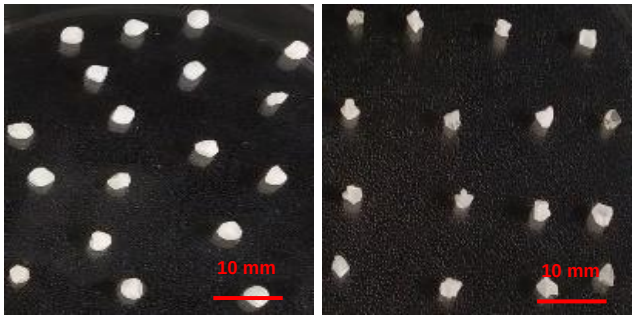

Figure A1.16 – Experiment $G1_{2.5\text{-}2\text{-}CHI\text{-}0.65}$ (entry 16), hydrogel and alcohol gel, respectively

A2 – 2nd Generation

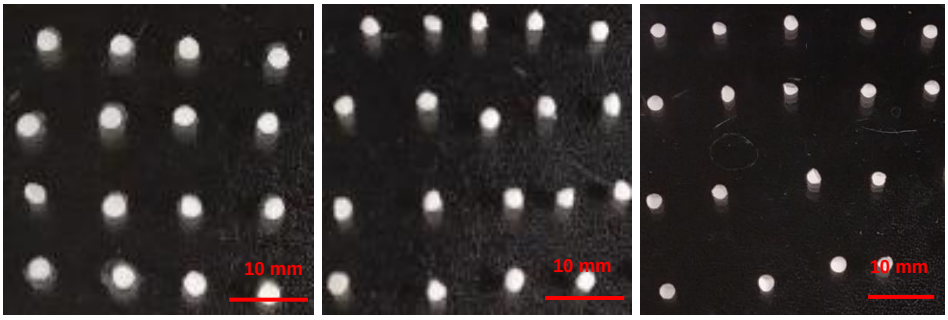

Figure A2.1 – Experiment $G_{2P1\text{-}4\text{-}0\text{-}Ø\text{-}t.but}$ (entry 17), hydrogel, alcohol gel, and cryogel respectively

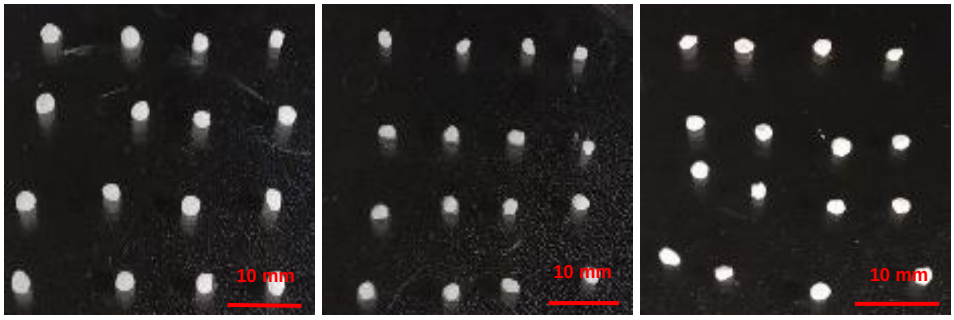

Figure A2.2 – Experiment $G2_{P1\text{-}1.2\text{-}0\text{-}Ø\text{-}t.but}$ (entry 18), hydrogel, alcohol gel, and cryogel respectively

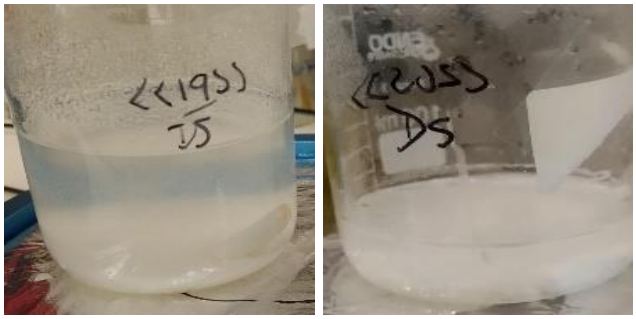

Figure A2.3 – Experiments $G2_{P1\text{-}1.2\text{-}0\text{-}SPA\text{-}xxx}$ (entry 19) and $G2_{P1\text{-}1.2\text{-}0\text{-}water\text{-}xxx}$ (entry 20), after polyelectrolyte complexation

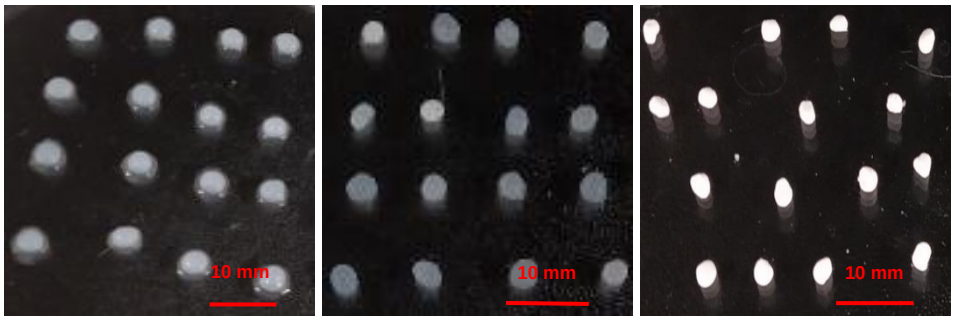

Figure A2.4 – Experiment $G2_{P1\text{-}1.2\text{-}0.1\text{-}Ø\text{-}t.but}$ (entry 21) hydrogel, alcohol gel, and cryogel respectively

A3 – 3rd Generation

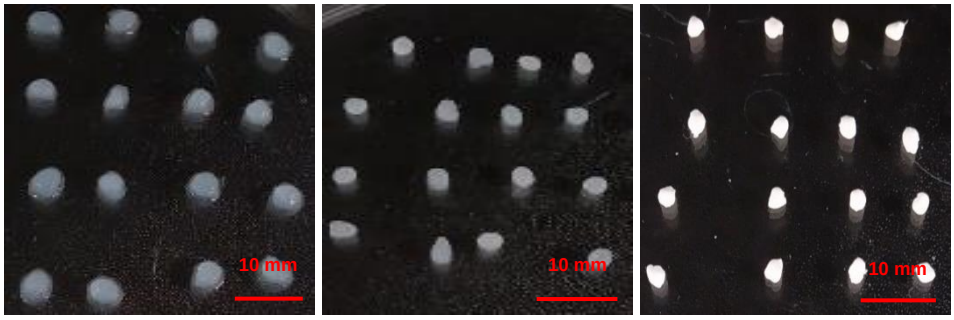

Figure A3.1 - Experiment $G3_{P2\text{-}0.13\text{-}GLU}$ (entry 22), hydrogel, alcohol gel, and cryogel respectively

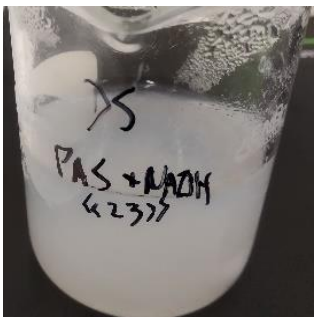

Figure A3.2 – Experiments $G3_{P2\text{-}0.26\text{-}GLU}$ (entry 23), after polyelectrolyte complexation

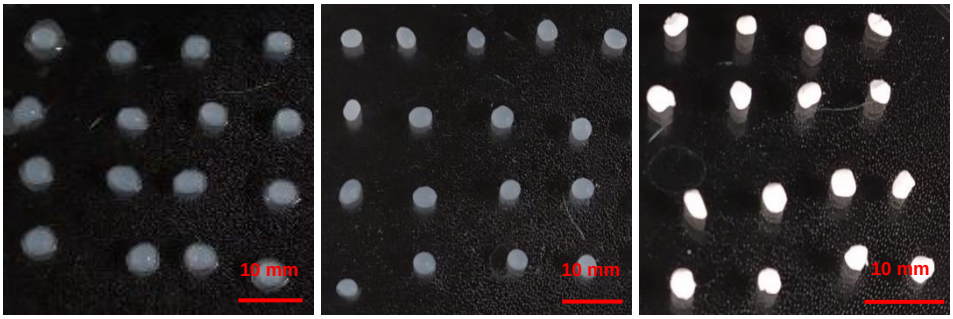

Figure A3.3 – Experiment $G3_{P2\text{-}0.13\text{-}TEA.OAc}$ (entry 24), hydrogel, alcohol gel, and cryogel respectively

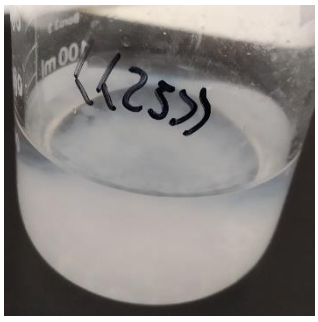

Figure A3.4 – Experiment $G3_{P2\text{-}0.26\text{-}TEA.OAc}$ (entry 25), after polyelectrolyte complexation

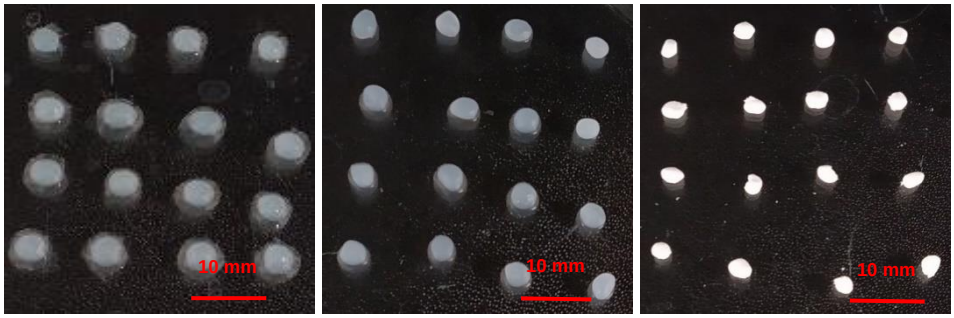

Figure A3.5 – Experiment $G_{3P2\text{-}0.13\text{-}THMAMS}$ (entry 26), hydrogel, alcohol gel, and cryogel respectively

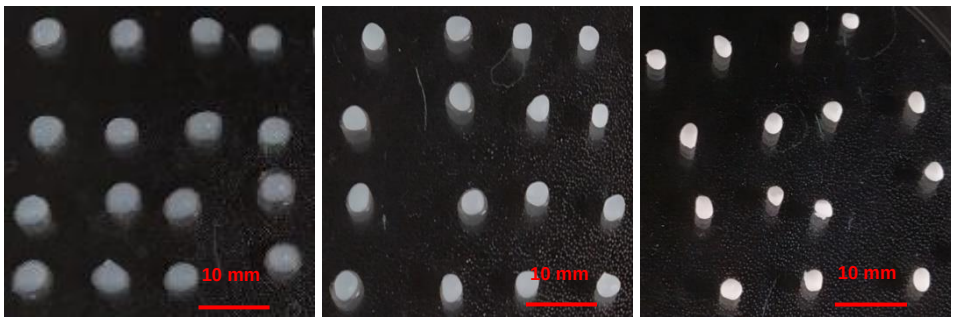

Figure A3.6 – Experiment $G3_{P2\text{-}0.26\text{-}THMAMS}$ (entry 27), hydrogel, alcohol gel, and cryogel respectively

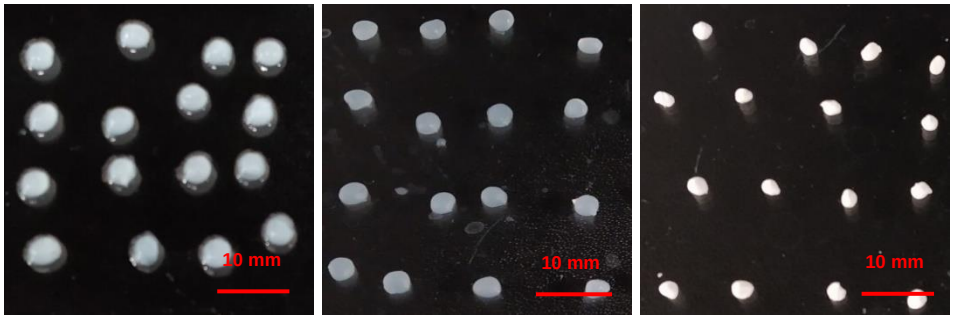

Figure A3.7 - Experiment $G3_{P2\text{-}0.13\text{-}TEA.Cl}$ (entry 28), hydrogel, alcohol gel, and cryogel respectively

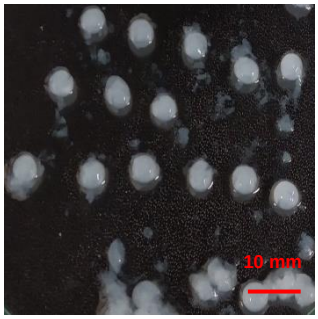

Figure A3.8 – Experiment $G_{3P2\text{-}0.26\text{-}TEA.Cl}$ (entry 29) hydrogel

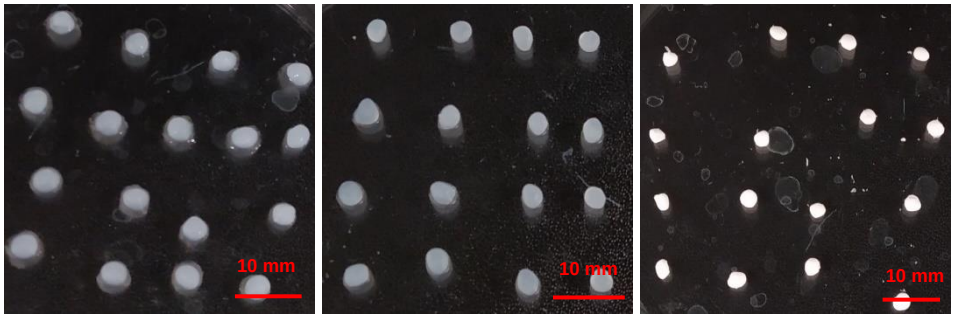

Figure A3.9 - Experiment $G3_{P2\text{-}0.13\text{-}THMAMS\text{-}60^{o}C}$ (entry 30), hydrogel, alcohol gel, and cryogel respectively

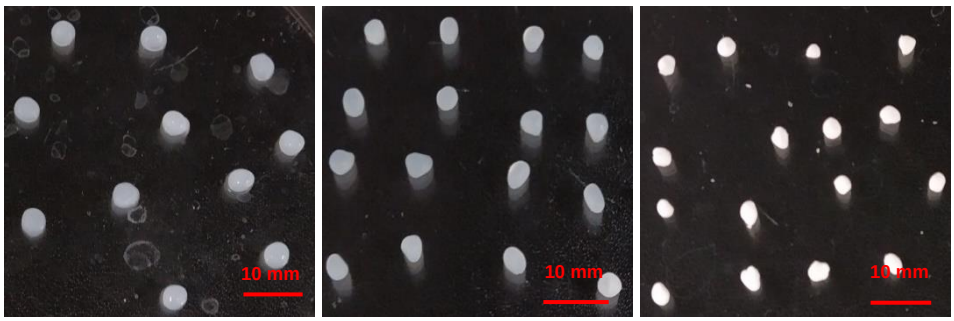

Figure A3.10- Experiment $G3_{P2\text{-}0.26\text{-}THMAMS\text{-}60^{o}C}$ (entry 31), hydrogel, alcohol gel, and cryogel respectively

B – SEM images of the cryogel beads

B1 – 1st Generation

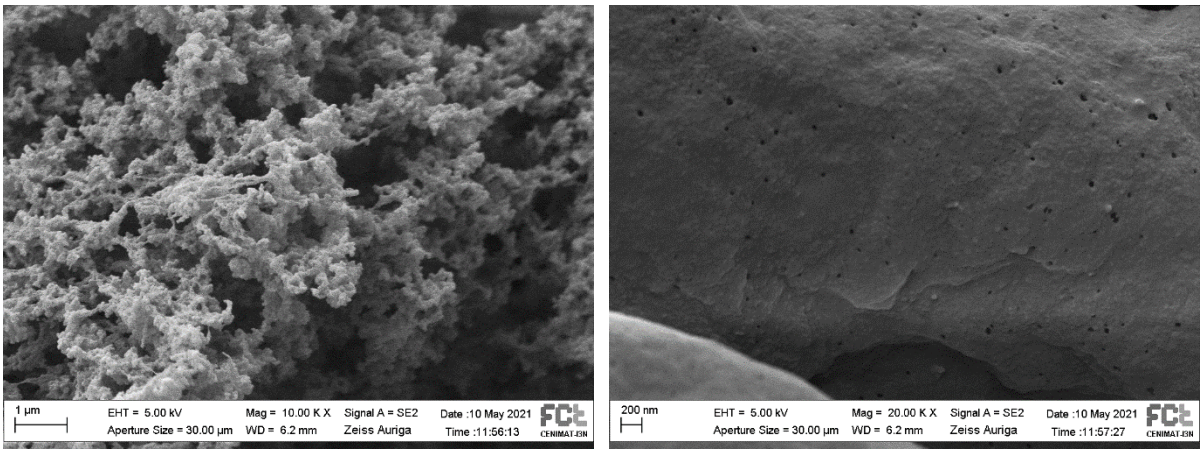

Figure B1.1 - Experiment $G1_{1\text{-}1\text{-}Ø\text{-}0.65}$ (entry 9), inner structure and outer surface of beads, respectively

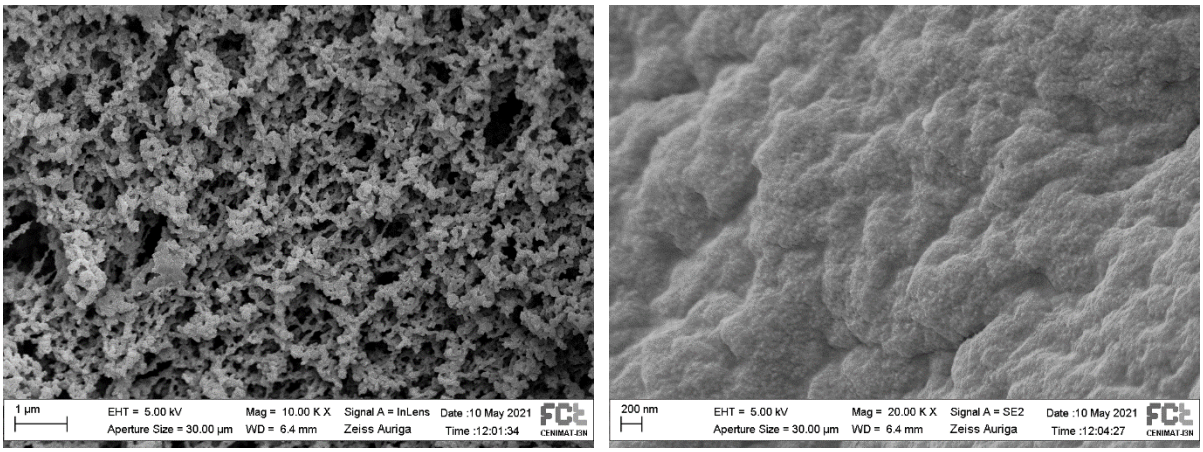

Figure B1.2 - Experiment $G1_{1\text{-}1\text{-}0.13\text{-}0.65}$ (entry 10), inner structure and outer surface of the beads, respectively

B2 – 2nd Generation

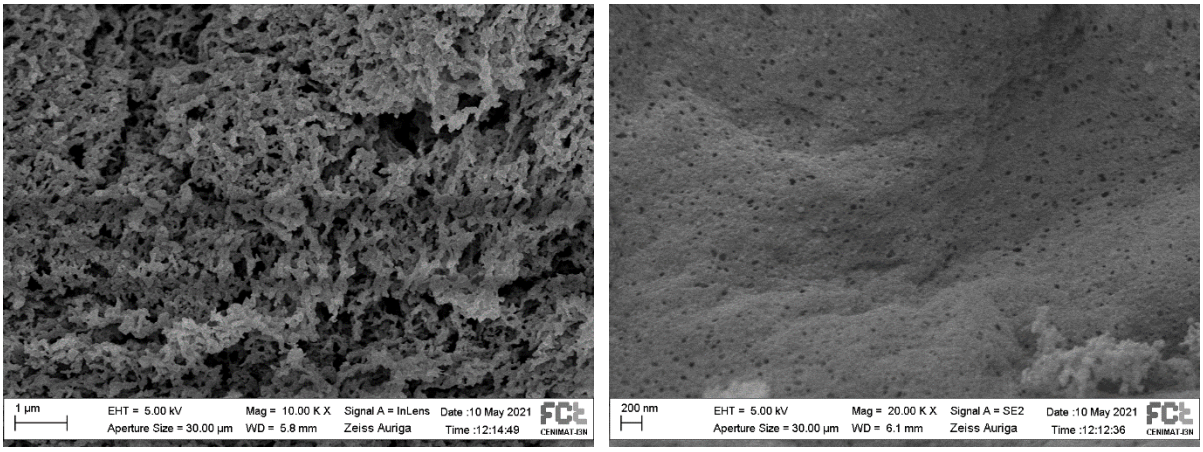

Figure B2.1 - Experiment $G2_{P1\text{-}4\text{-}0\text{-}Ø\text{-}t.but}$ (entry 17), inner structure and outer surface of the beads, respectively

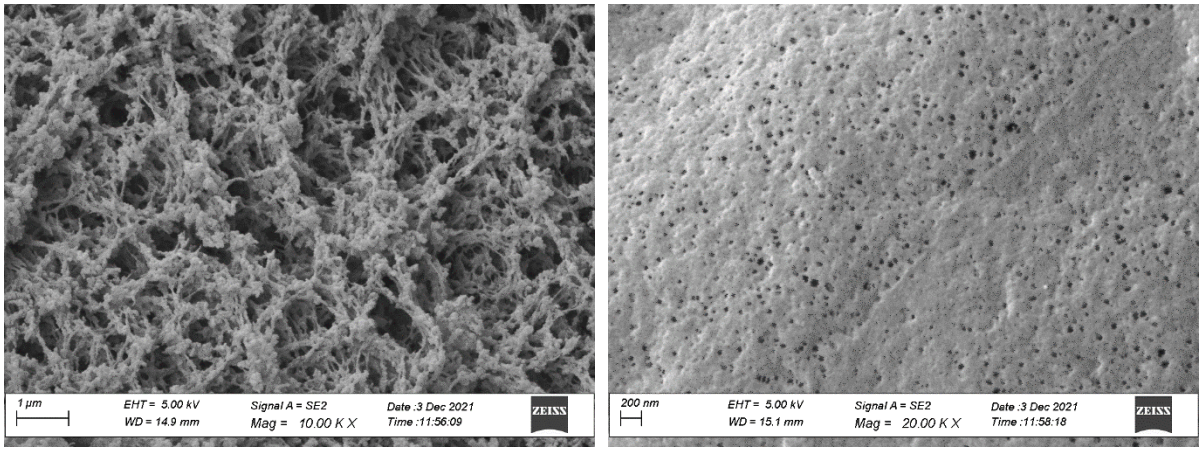

Figure B2.2 - Experiment $G2_{P1\text{-}1.2\text{-}0\text{-}Ø\text{-}t.but}$ (entry 18), inner structure and outer surface of the beads, respectively

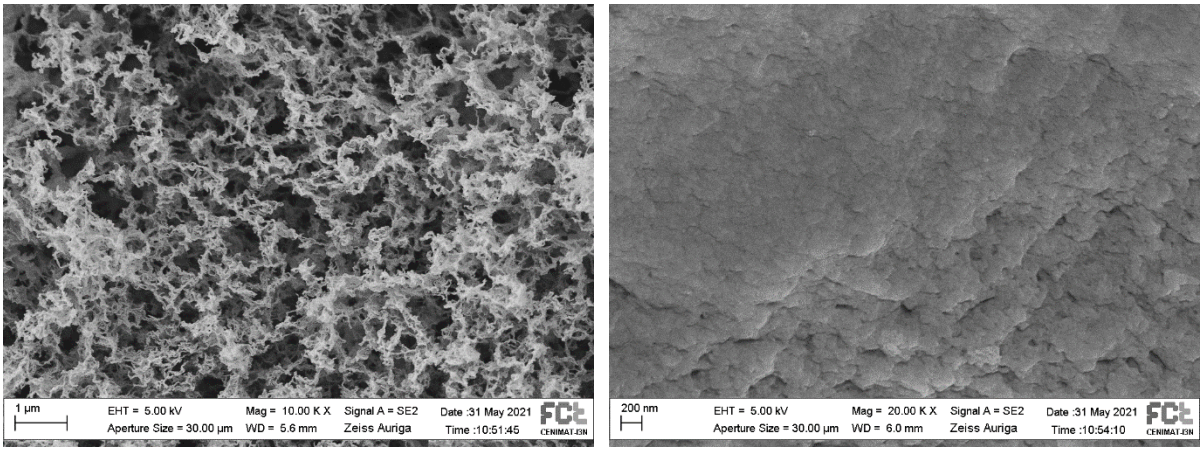

Figure B2.3 - Experiment – Experiment $G2_{P1\text{-}1.2\text{-}0.1\text{-}Ø\text{-}t.but}$ (entry 21), inner structure and outer surface of the beads, respectively

B3 – 3rd Generation

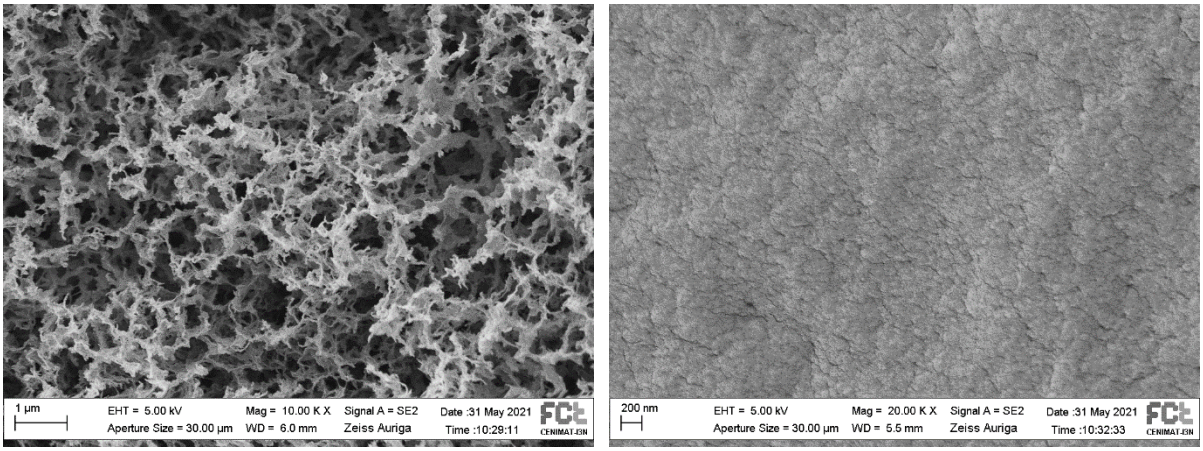

Figure B3.1 - Experiment $G3_{P2\text{-}0.13\text{-}GLU}$ (entry 22), inner structure and outer surface of the beads, respectively

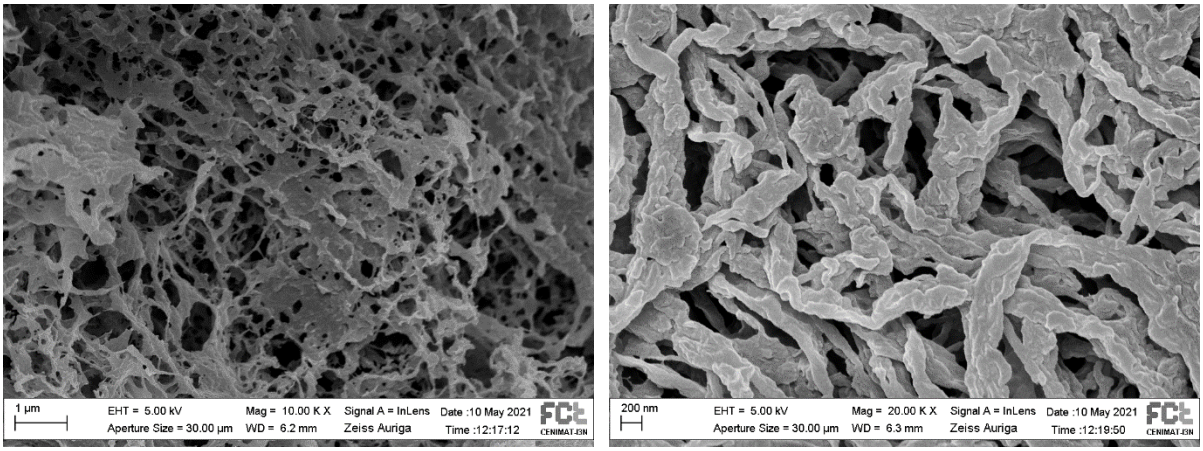

Figure B3.2 – Experiment $G3_{P2\text{-}0.13\text{-}TEA.OAc}$ (entry 24), inner structure and outer surface of the beads, respectively

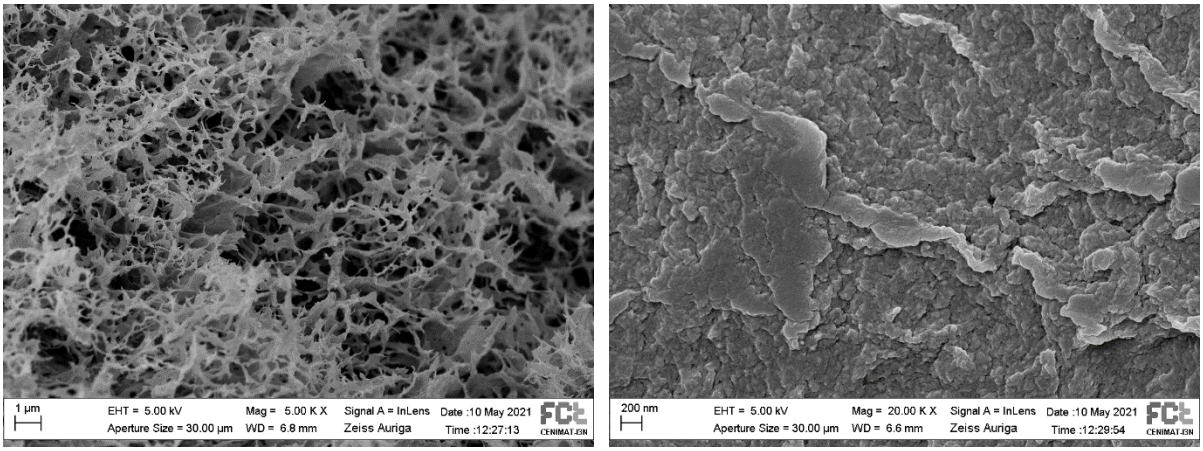

Figure B3.3 – Experiment $G3_{P2\text{-}0.13\text{-}THMAMS}$ (entry 26), inner structure and outer surface of the beads, respectively

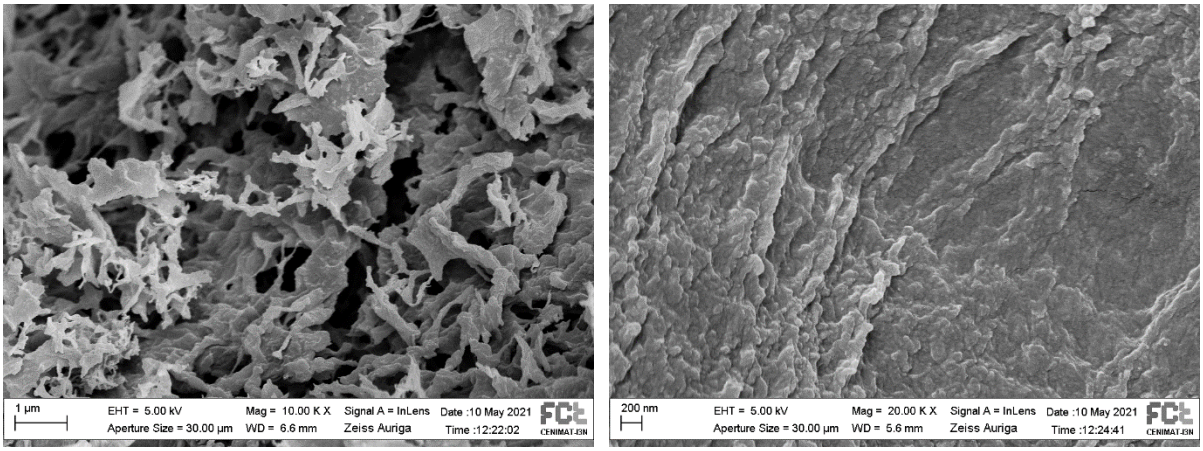

Figure B3.4 - Experiment $G3_{P2\text{-}0.26\text{-}THMAMS}$ (entry 27), inner structure and outer surface of the beads, respectively

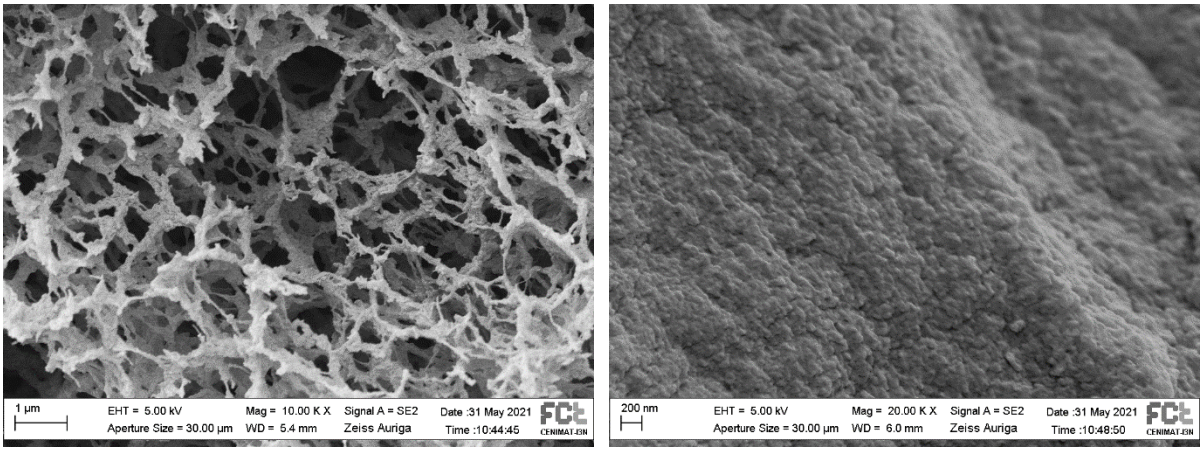

Figure B3.5 - Experiment $G3_{P2\text{-}0.13\text{-}TEA.Cl}$ (entry 28), inner structure and outer surface of the cryogel beads, respectively

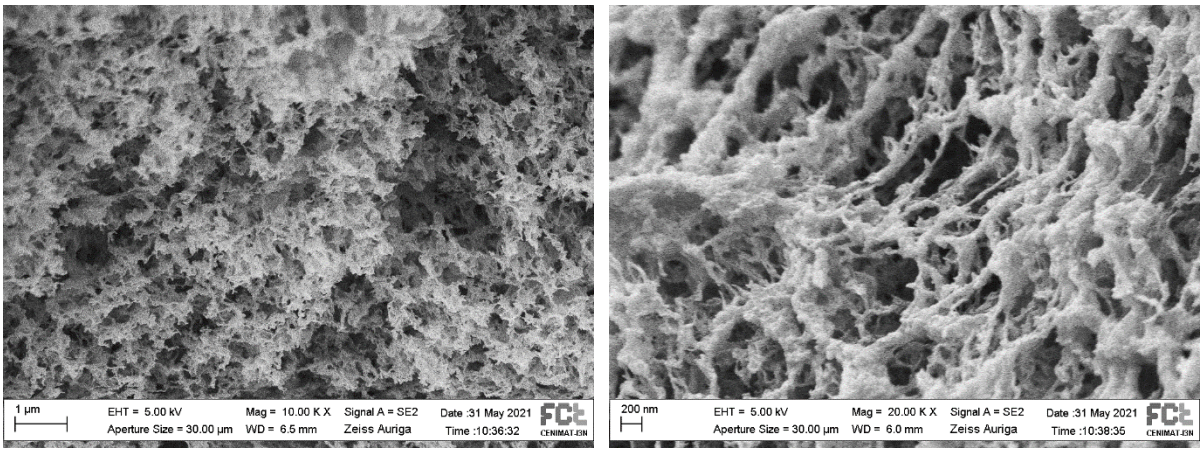

Figure B3.6 - Experiment $G3_{P2\text{-}0.13\text{-}THMAMS\text{-}60^{o}C}$ (entry 30), inner structure and outer surface of the cryogel beads, respectively

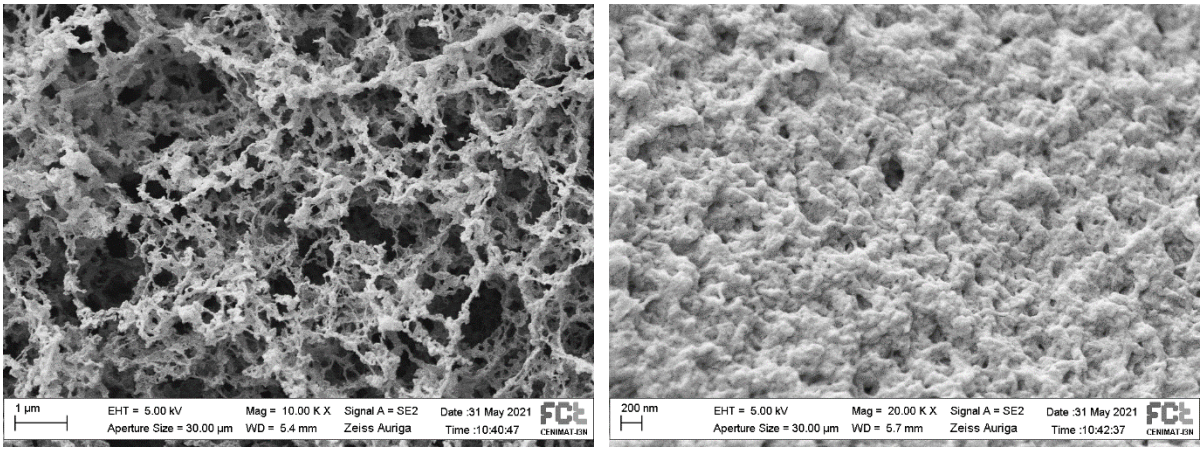

Figure B3.7 - Experiment $G3_{P2\text{-}0.26\text{-}THMAMS\text{-}60^{o}C}$ (entry 31), inner structure and outer surface of the cryogel beads, respectively

C – Dimensional analysis of the beads

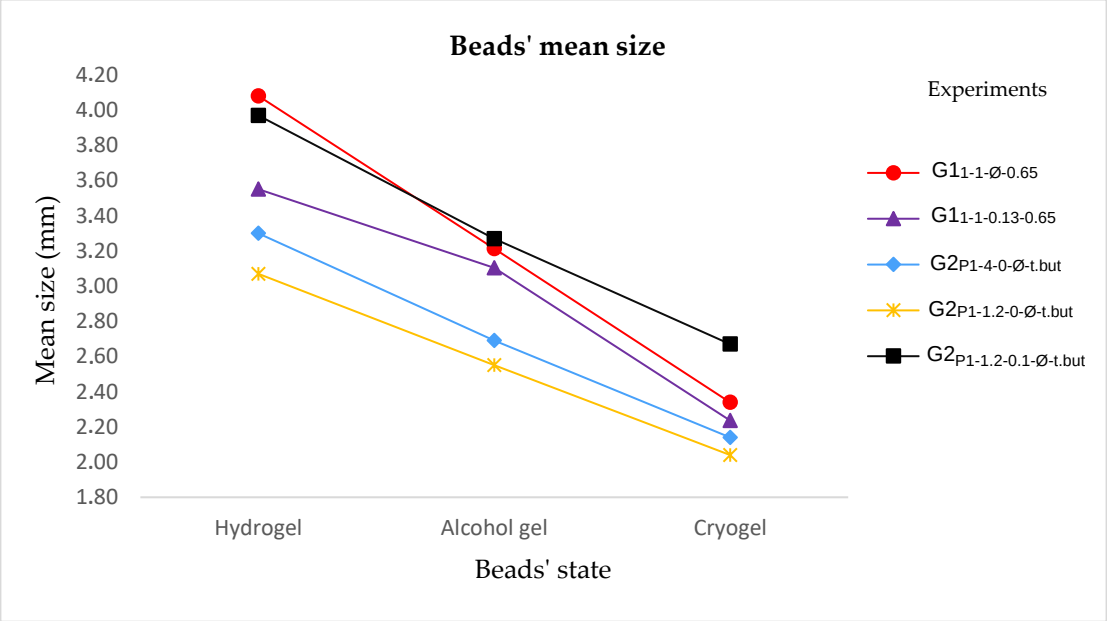

Figure C1.1 - 1st and 2nd generation of beads' mean size

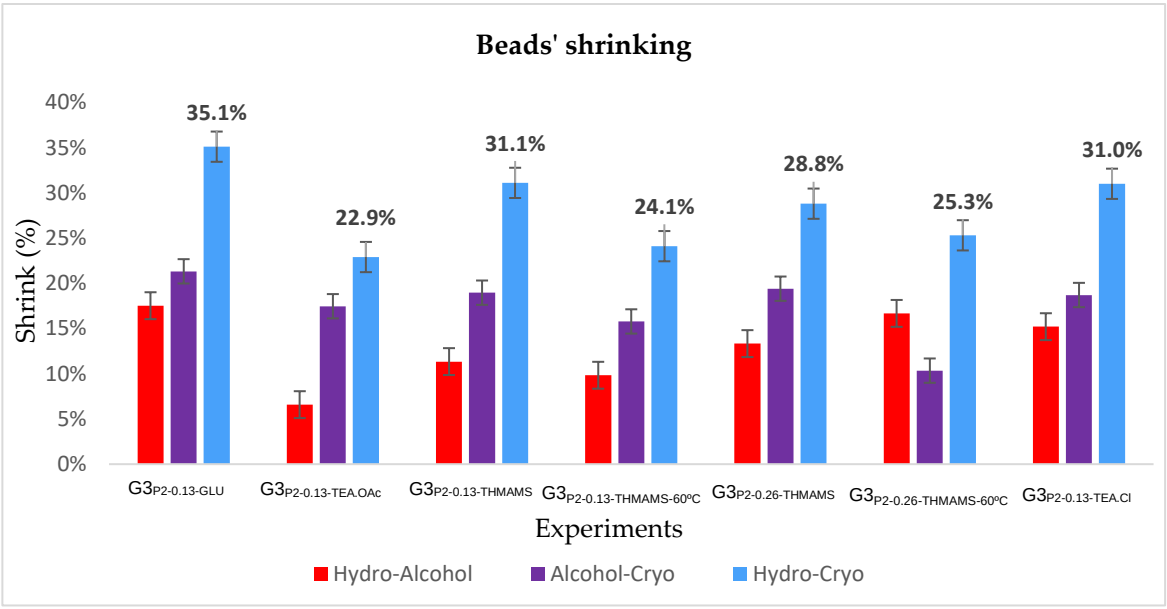

Figure C1.2 - Percentual shrinking of the 3rd generation of beads in hydrogel to alcohol gel (red), alcohol gel to cryogel (purple), and hydrogel to cryogel (blue)

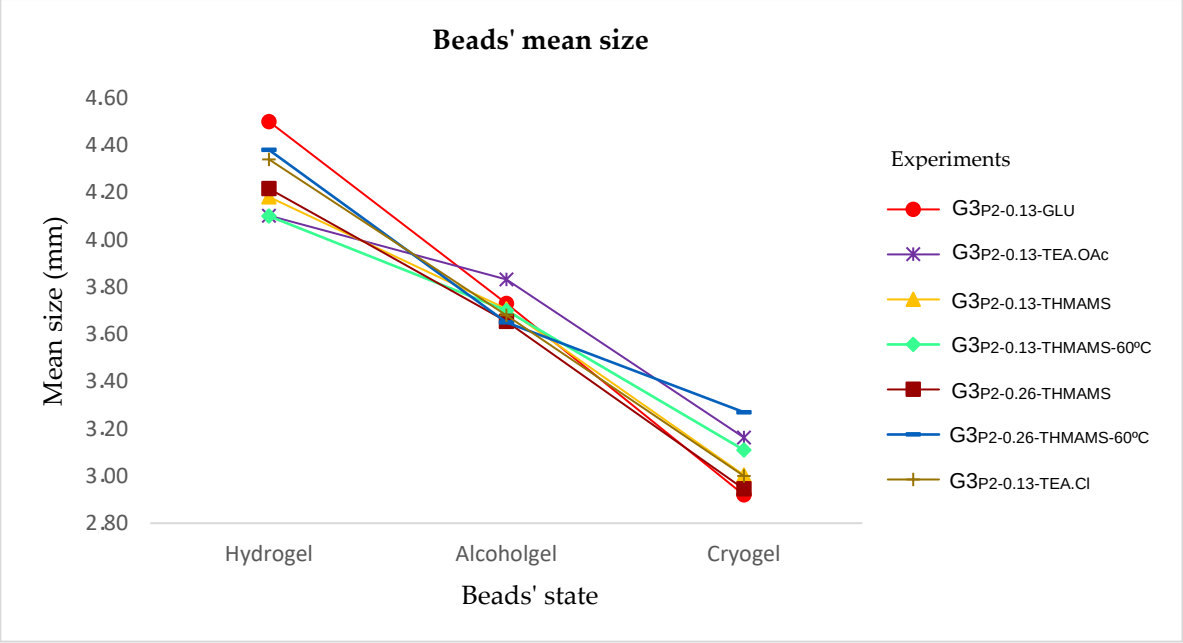

Figure C1.3 - 3rd generation of beads' mean size

D - N_2 Adsorption

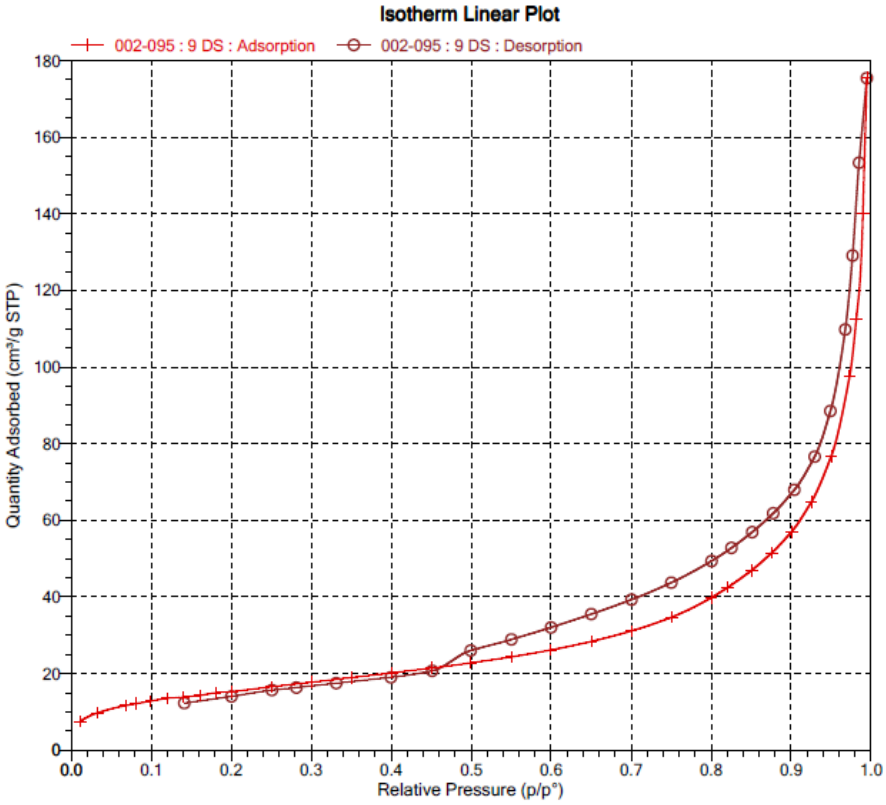

Figura D1 - Experiment $G1_{1\text{-}1\text{-}Ø\text{-}0.65}$ (entry 9), isotherm linear plot

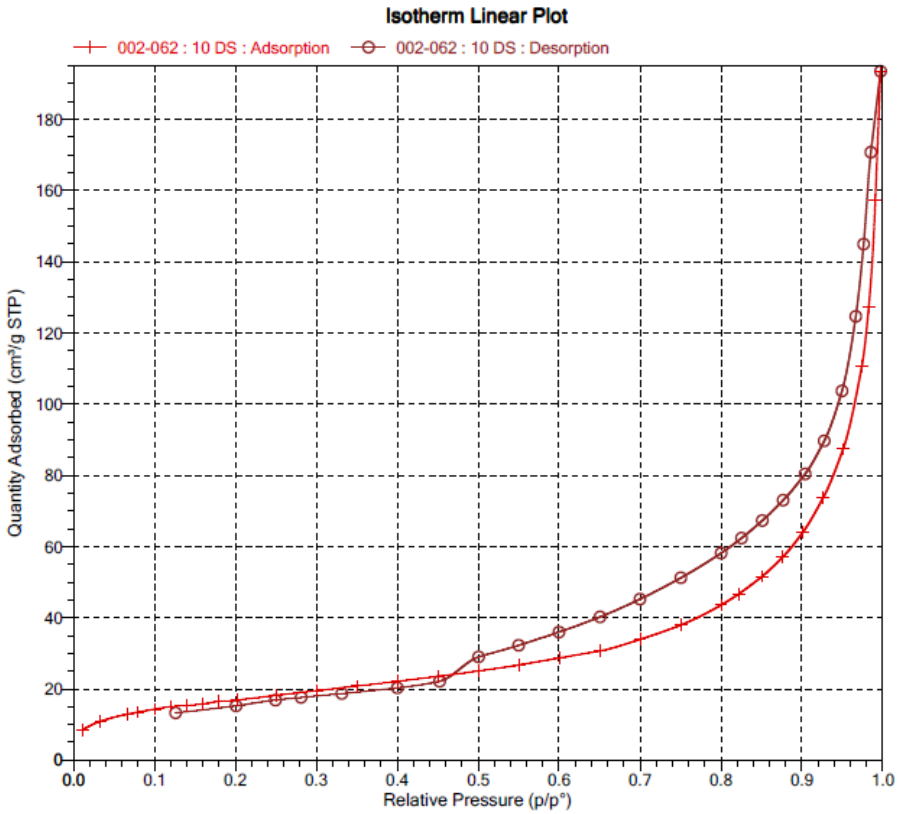

Figure D2 - Experiment $G1_{1\text{-}1\text{-}CHI\text{-}0.65}$ (entry 10), isotherm linear plot

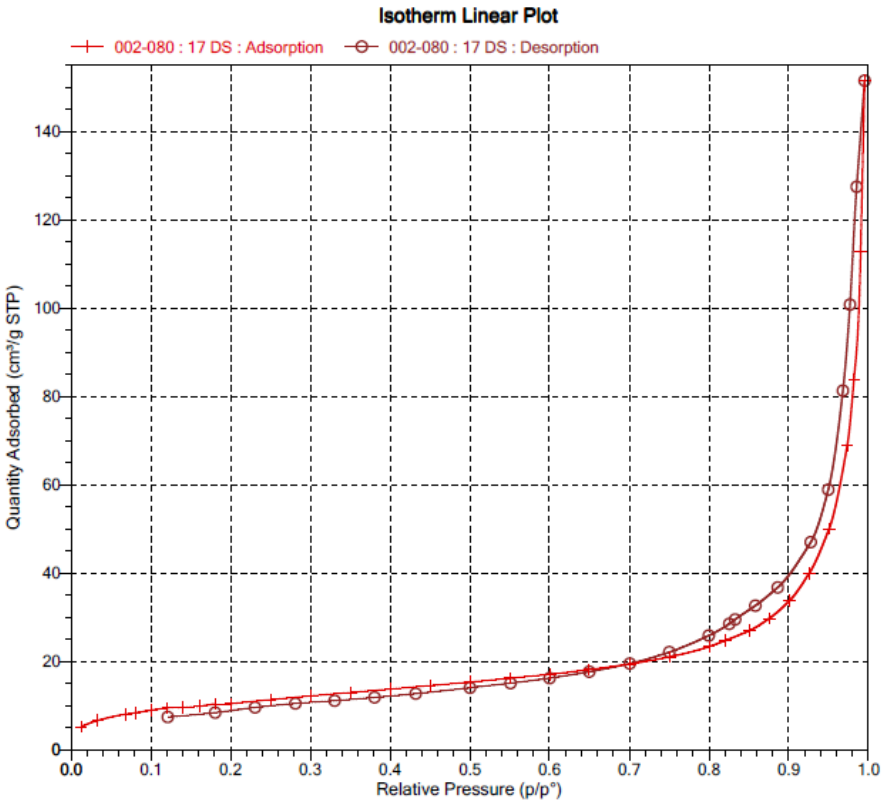

Figure D3 - Experiment G2$_{P1\text{-}4\text{-}0\text{-}Ø\text{-}t.but}$ (entry 17), isotherm linear plot

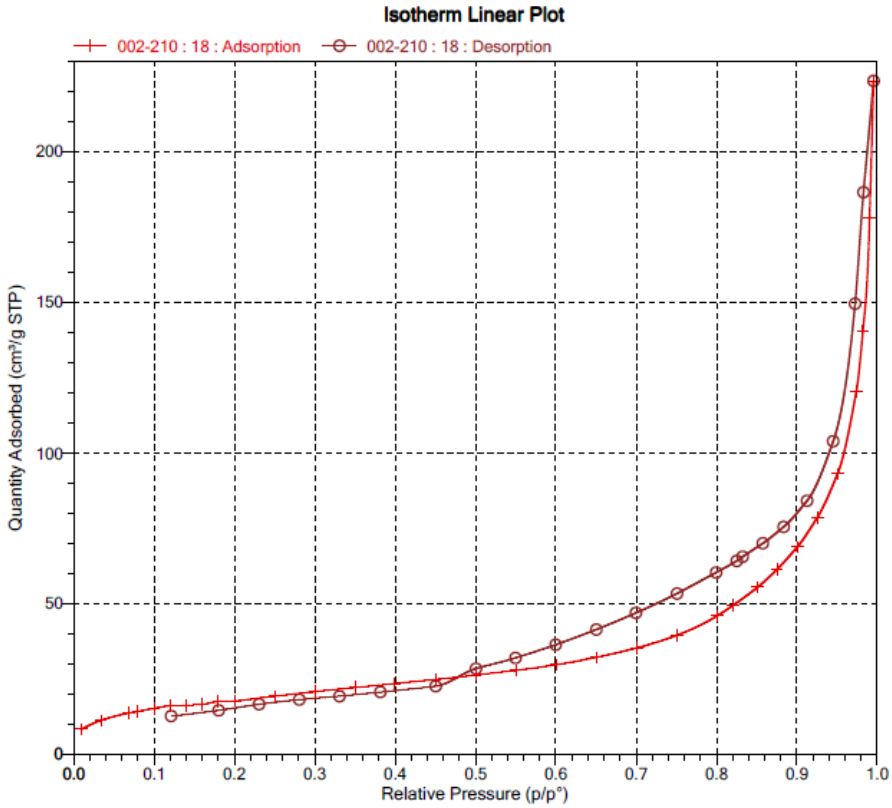

Figure D4 - Experiment G2$_{P1\text{-}1.2\text{-}0\text{-}Ø\text{-}t.but}$ (entry 18), isotherm linear plot

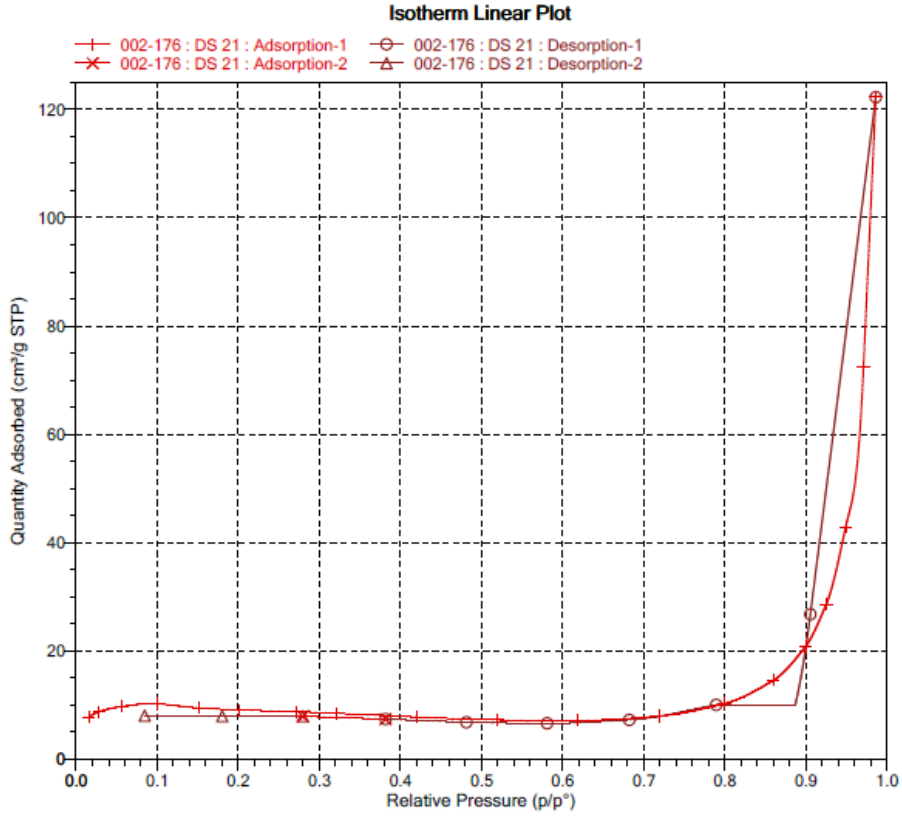

Figure D5 - Experiment G2$_{P1\text{-}1.2\text{-}0.1\text{-}Ø\text{-}t.but}$ (entry 21), isotherm linear plot

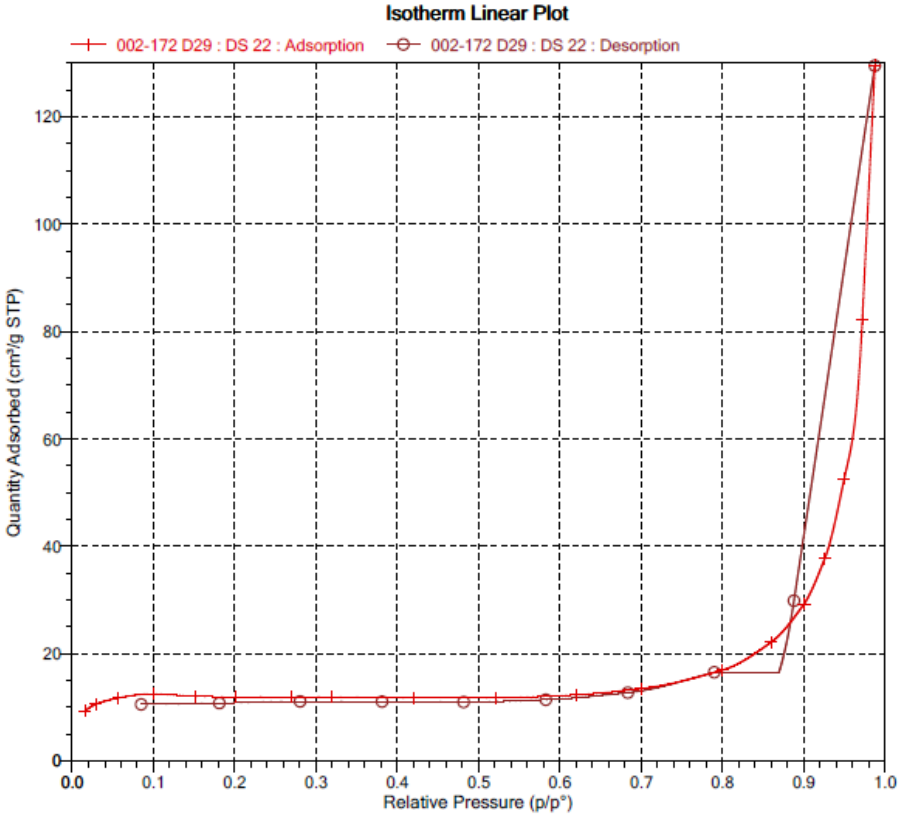

Figure D6 - Experiment G3$_{P2\text{-}0.13\text{-}GLU}$ (entry 22), isotherm linear plot

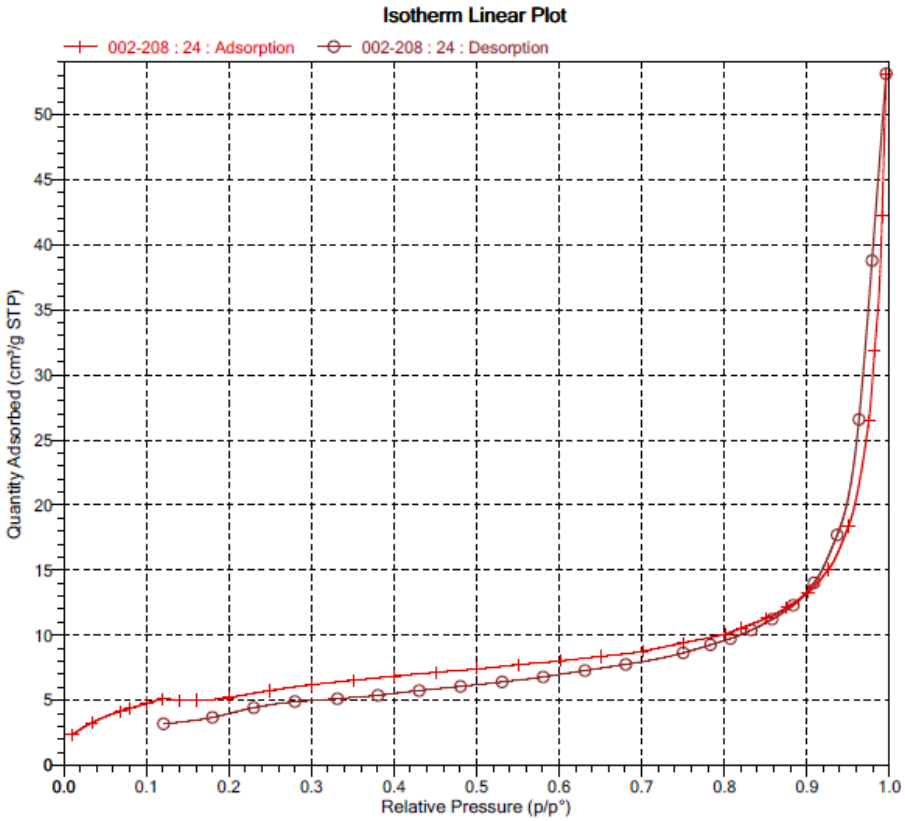

Figure D7 - Experience G3$_{P2\text{-}0.13\text{-}TEA.OAc}$ (entry 24), isotherm linear plot

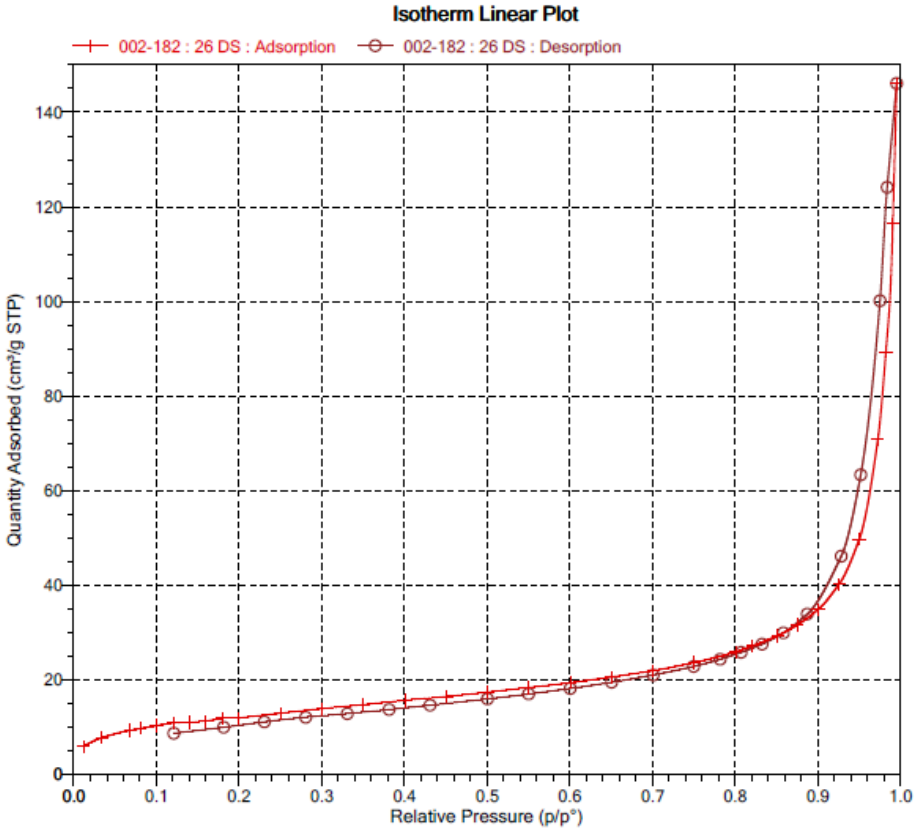

Figure D8 - Experiment G3$_{P2\text{-}0.13\text{-}THMAMS}$ (entry 26), isotherm linear plot

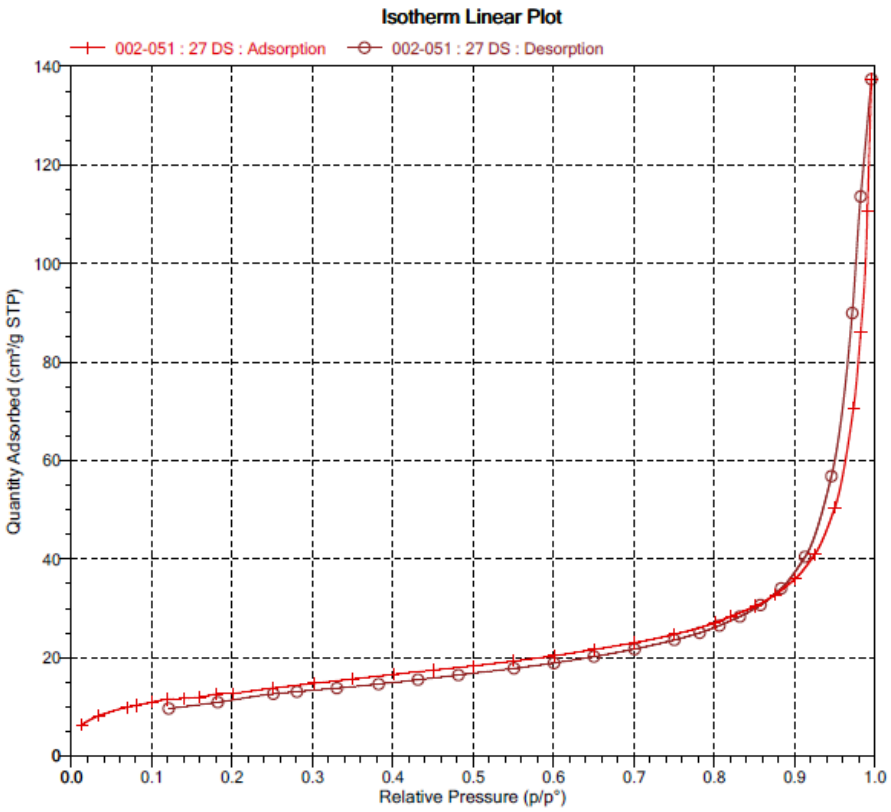

Figure D9 - Experiment G3$_{P2\text{-}0.26\text{-}THMAMS}$ (entry 27), isotherm linear plot

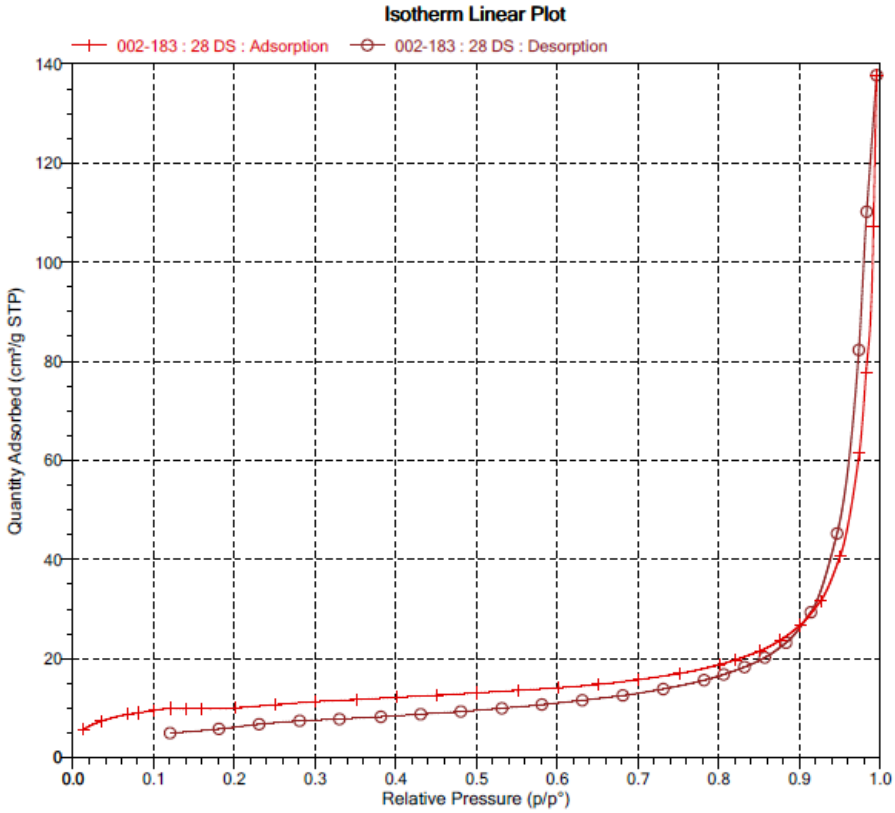

Figure D10 - Experiment G3$_{P2\text{-}0.26\text{-}TEA.Cl}$ (entry 28), isotherm linear plot

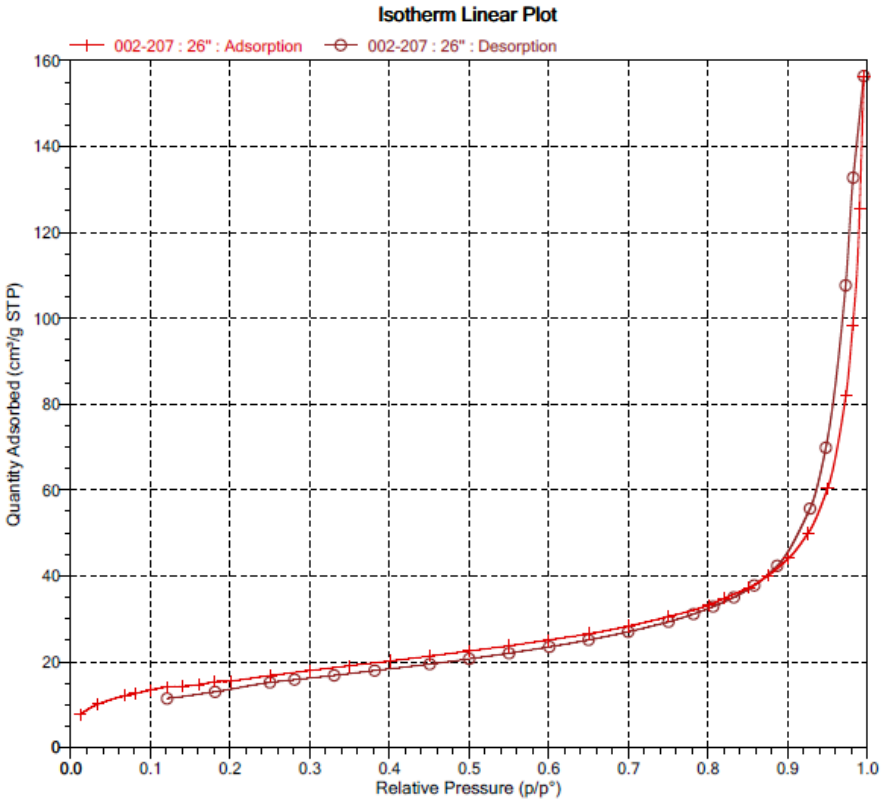

Figure D11 - Experiment G3$_{\text{P2-0.13-THMAMS-60°C}}$ (entry 30), isotherm linear plot

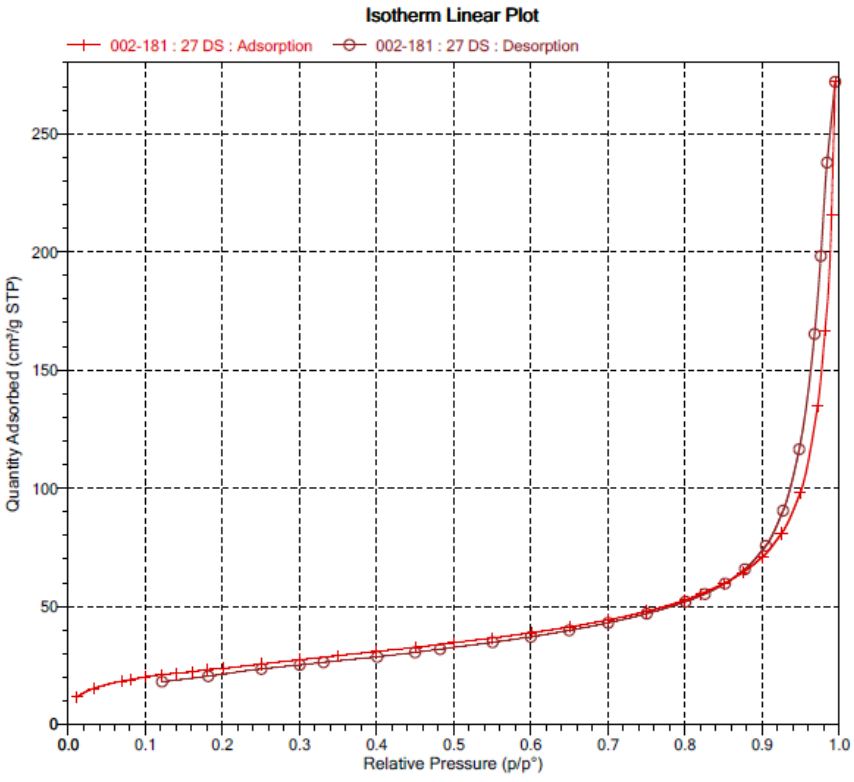

Figure D12 - Experiment G3$_{\text{P2-0.26-THMAMS-60°C}}$ (entry 31), isotherm linear plot

E - FTIR

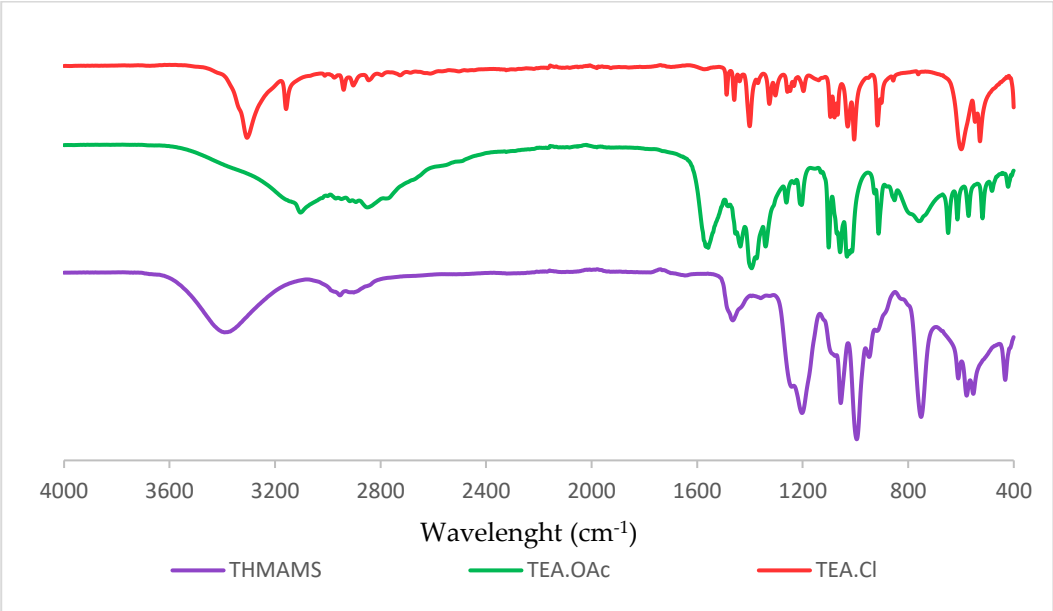

Figure E1 - FTIR spectra of THMAMS (purple), TEA.OAc (green) and TEA.Cl (red)

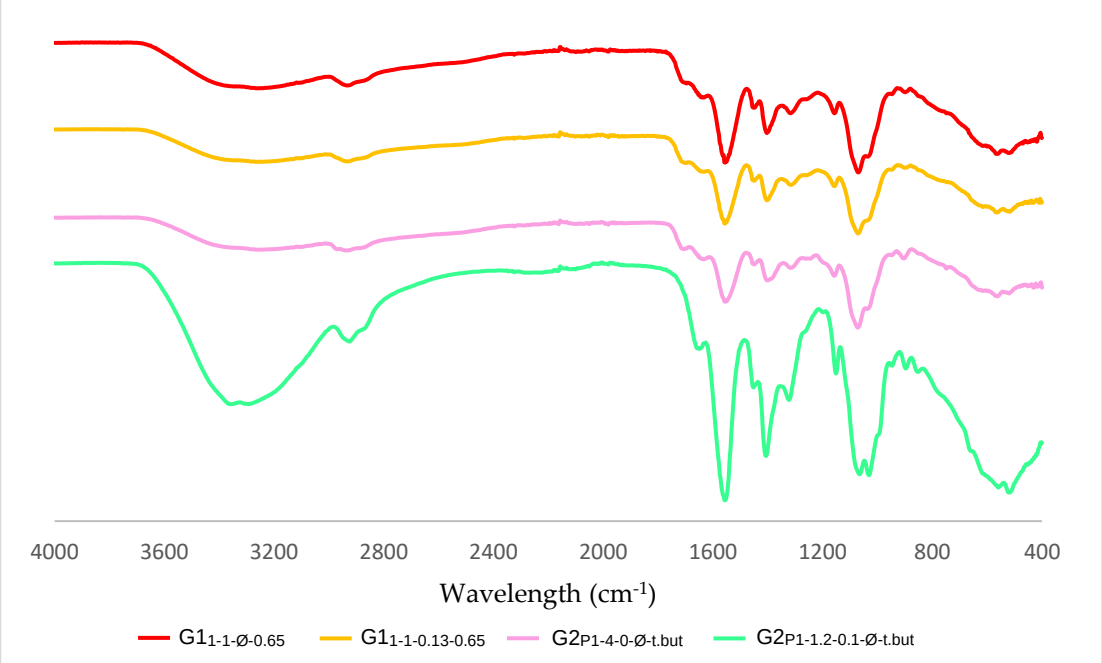

Figure E2 - FTIR spectra of 1st and 2nd Generation

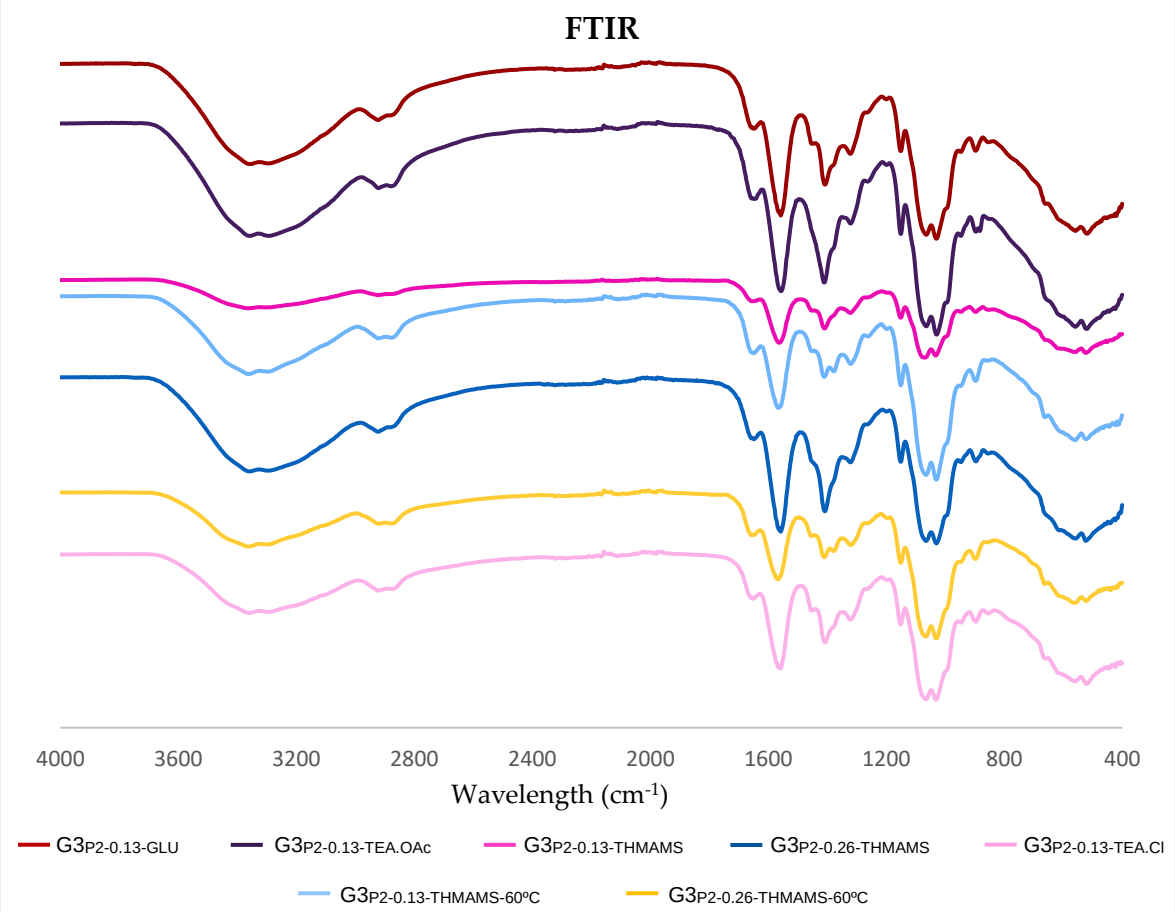

Figure E3 - FTIR spectra of 3rd Generation

F – CO_2 Capture

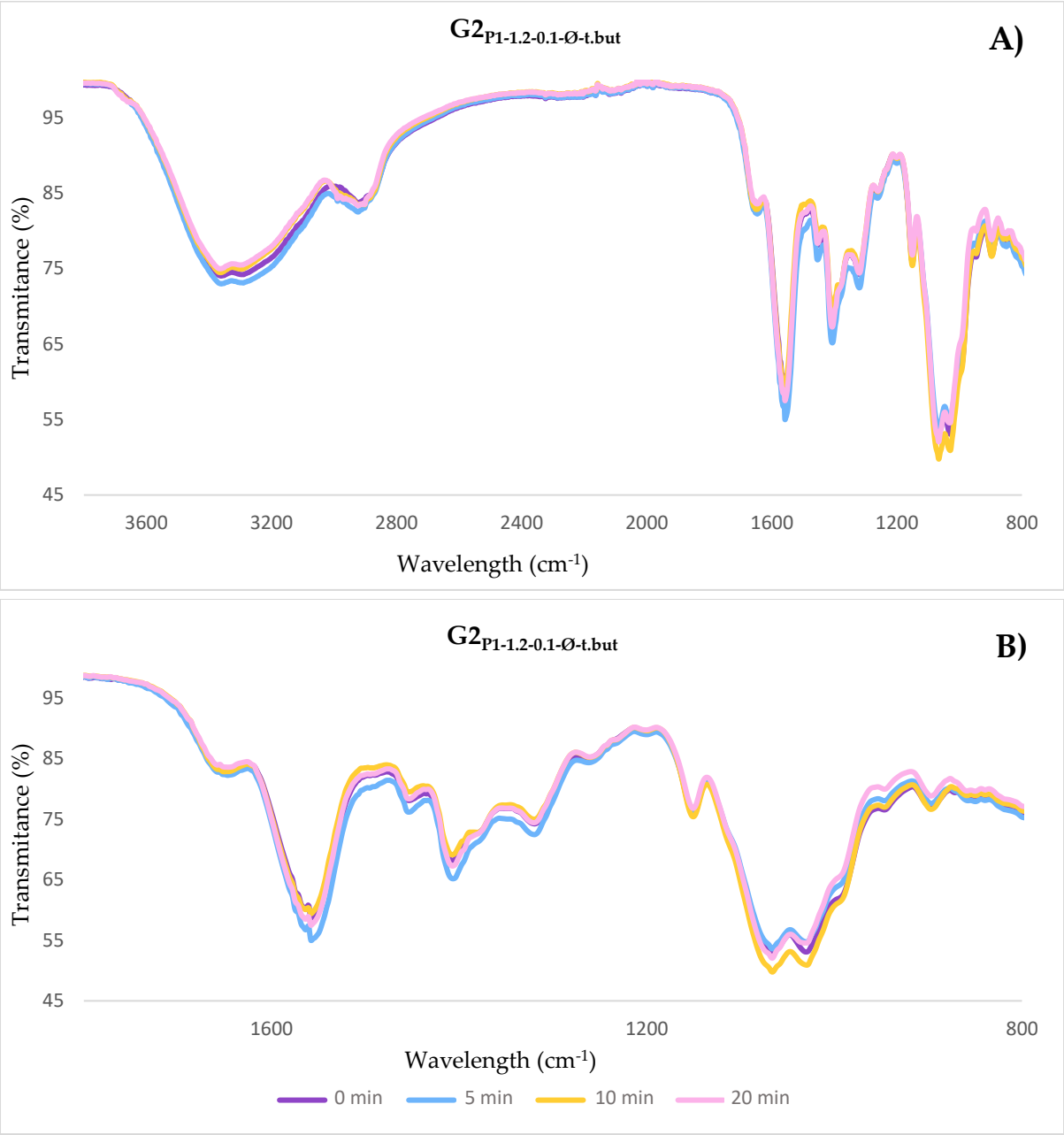

Figure F1- FTIR spectra of experiment $G2_{P1\text{-}1.2\text{-}0.1\text{-}Ø\text{-}t.but}$ after 0, 5, 10, and 20 min of CO_2 flux time. A) 3800-800 cm^{-1} range; B) 1800-800 cm^{-1} range

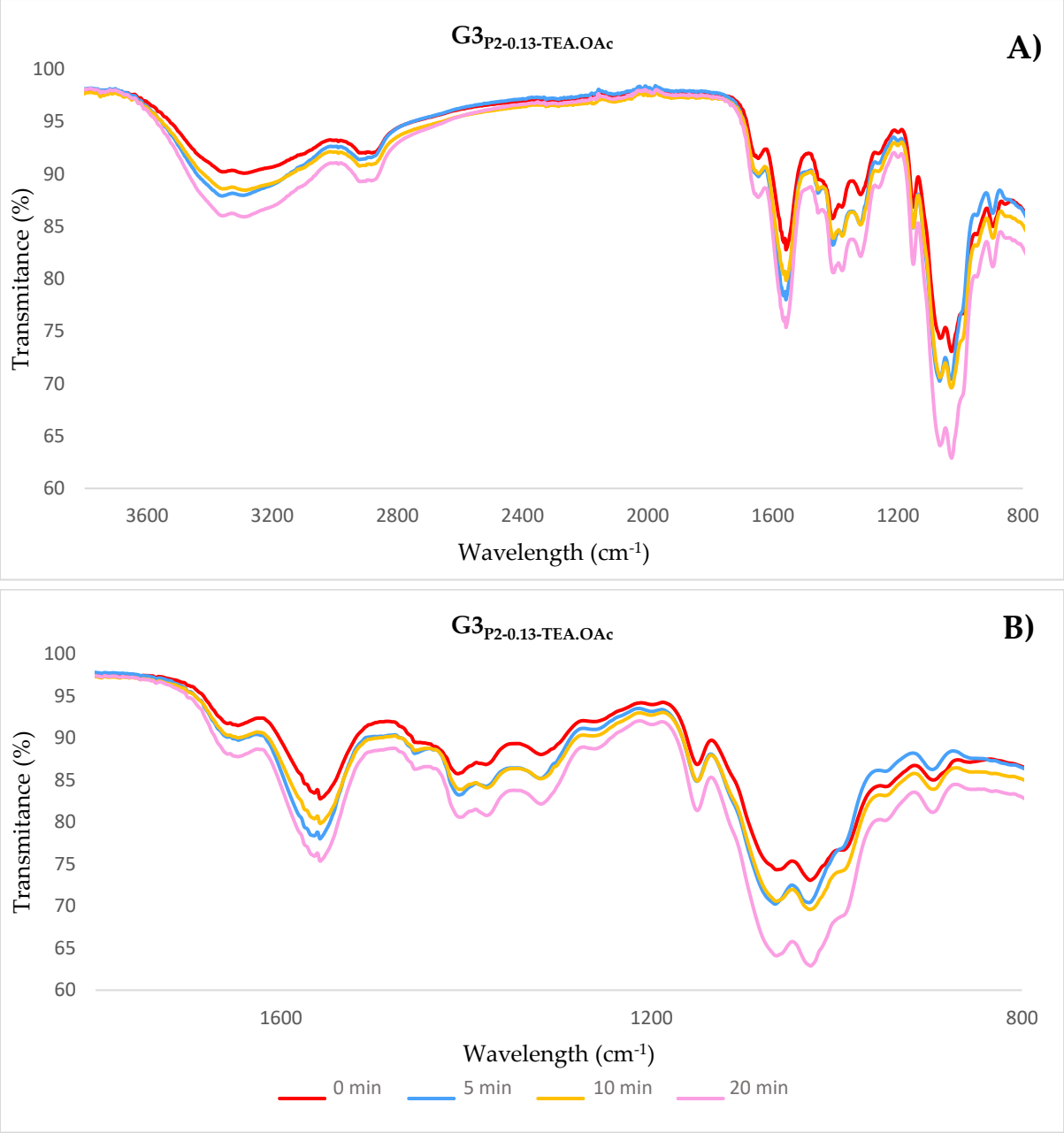

Figure F2 - FTIR spectra of experiment $G3_{P2\text{-}0.13\text{-}TEA.OAc}$ after 0, 5, 10, and 20 min of CO_2 flux time. A) 3800-800 cm^{-1} range; B) 1800-800 cm^{-1} range

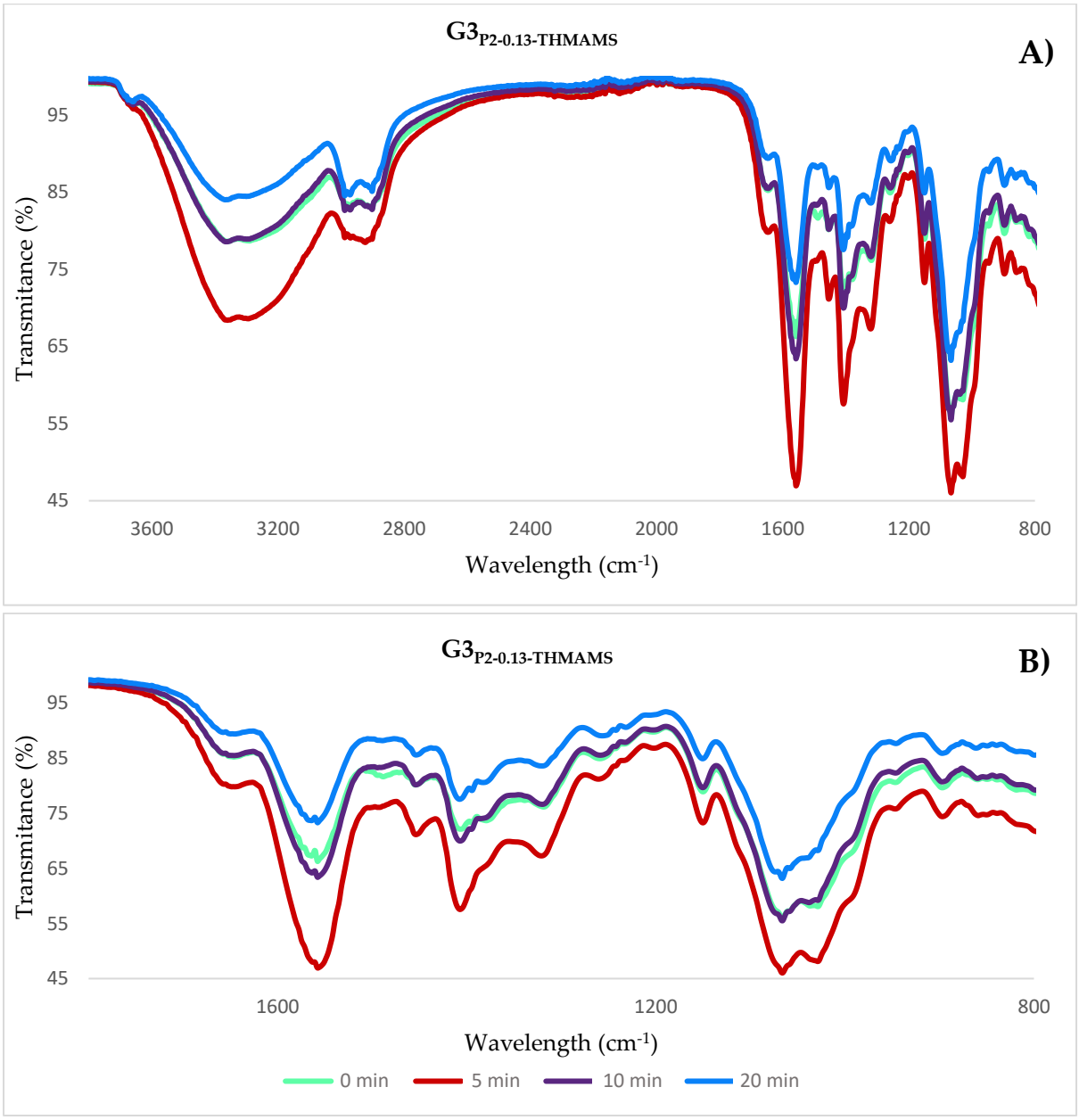

Figure F3 - FTIR spectra of experiment $G3_{P2\text{-}0.13\text{-}THMAMS}$ after 0, 5, 10, and 20 min of CO_2 flux time. A) 3800-800 cm^{-1} range; B) 1800-800 cm^{-1} range

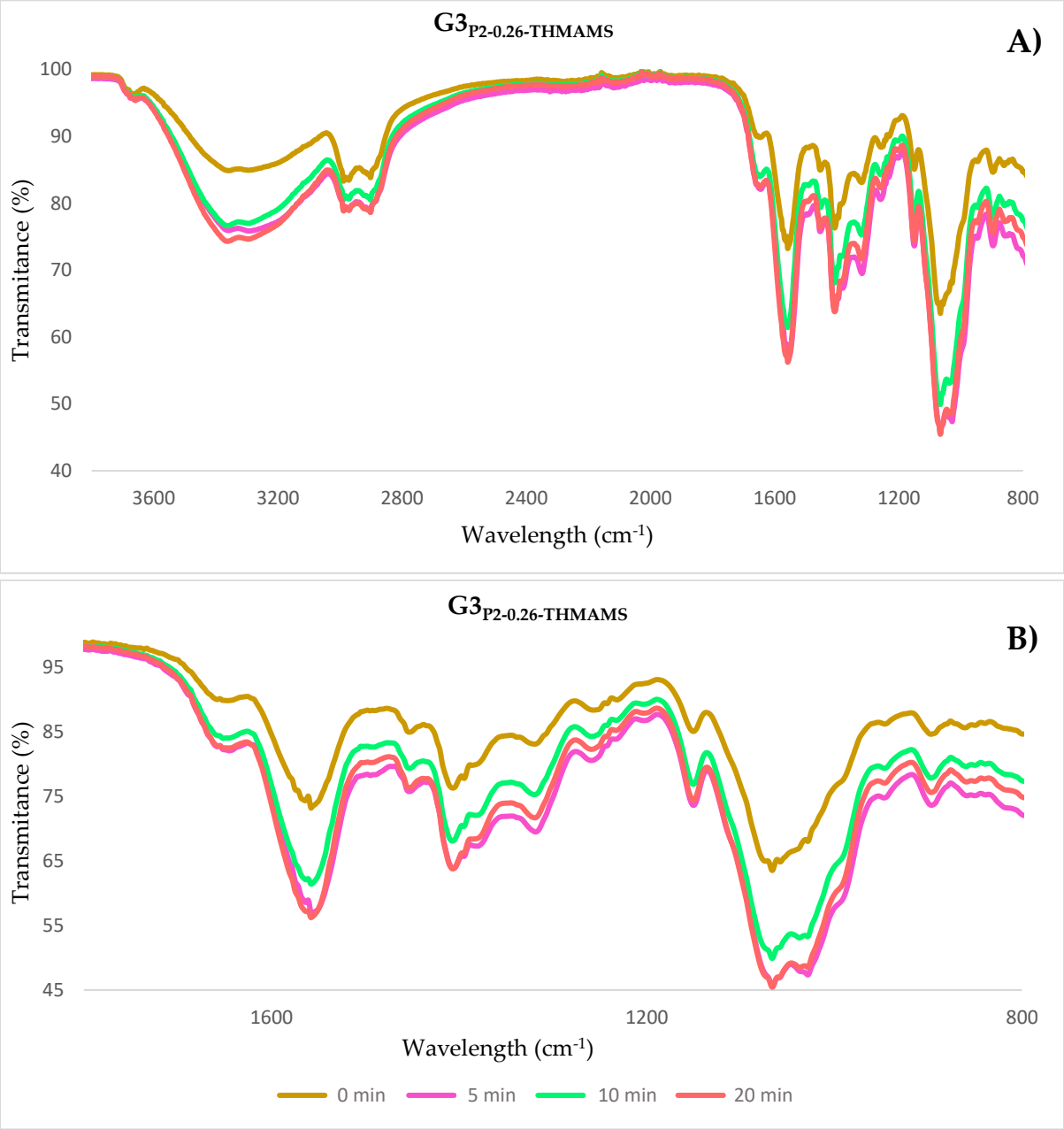

Figure F4 - FTIR spectra of experiment $G3_{P2\text{-}0.26\text{-}THMAMS}$ after 0, 5, 10, and 20 min of CO_2 flux time. A) 3800-800 cm^{-1} range; B) 1800-800 cm^{-1} range

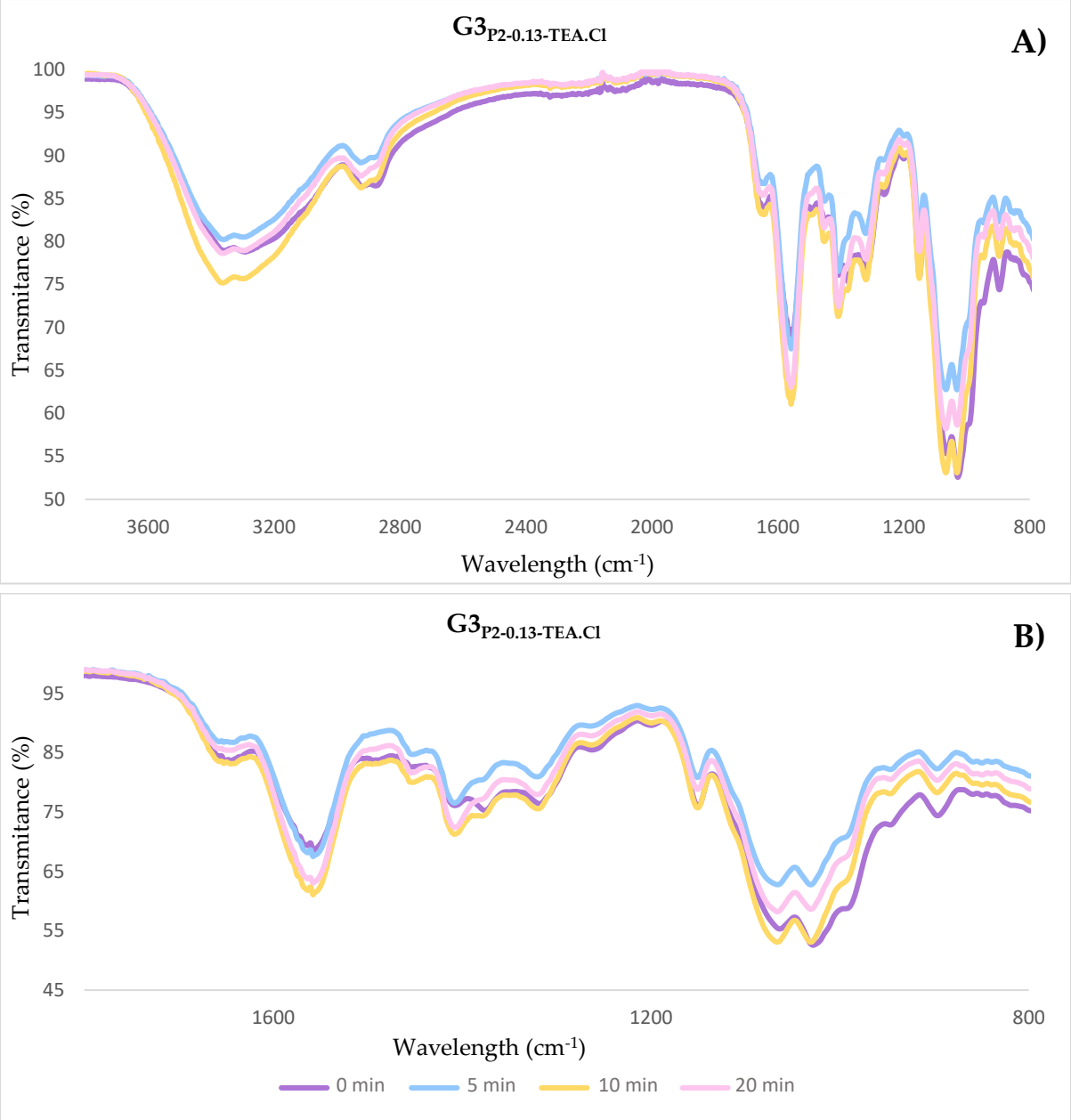

Figure F5 - FTIR spectra of experiment $G3_{P2\text{-}0.13\text{-}TEA.Cl}$ after 0, 5, 10, and 20 min of CO_2 flux time. A) 3800-800 cm^{-1} range; B) 1800-800 cm^{-1} range

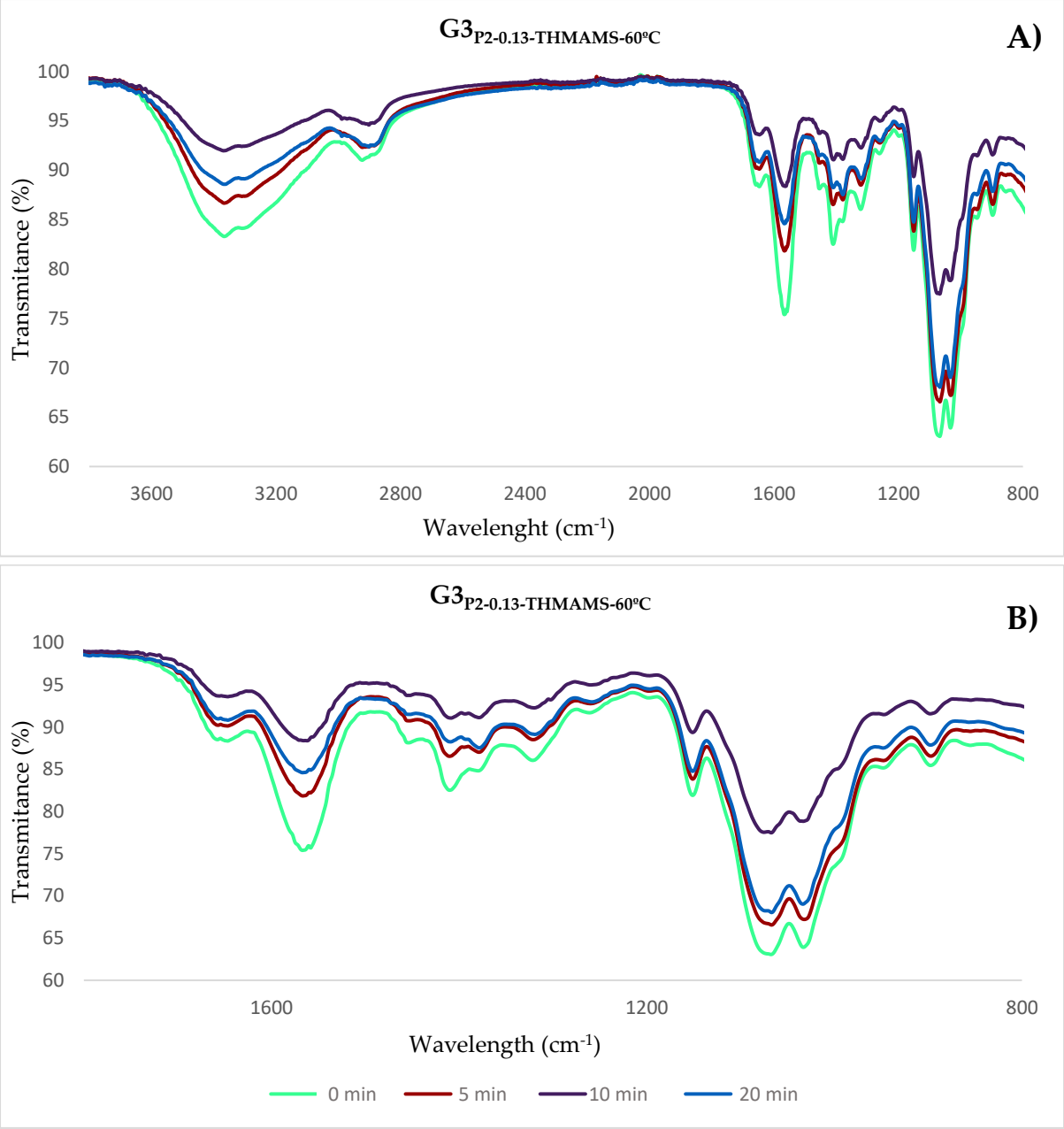

Figure F6 - Experiment $G3_{P2\text{-}0.13\text{-}THMAMS\text{-}60ºC}$ FTIR after 0, 5, 10, and 20 min of CO_2 flux time. A) 3800-800 cm^{-1} range; B) 1800-800 cm^{-1} range

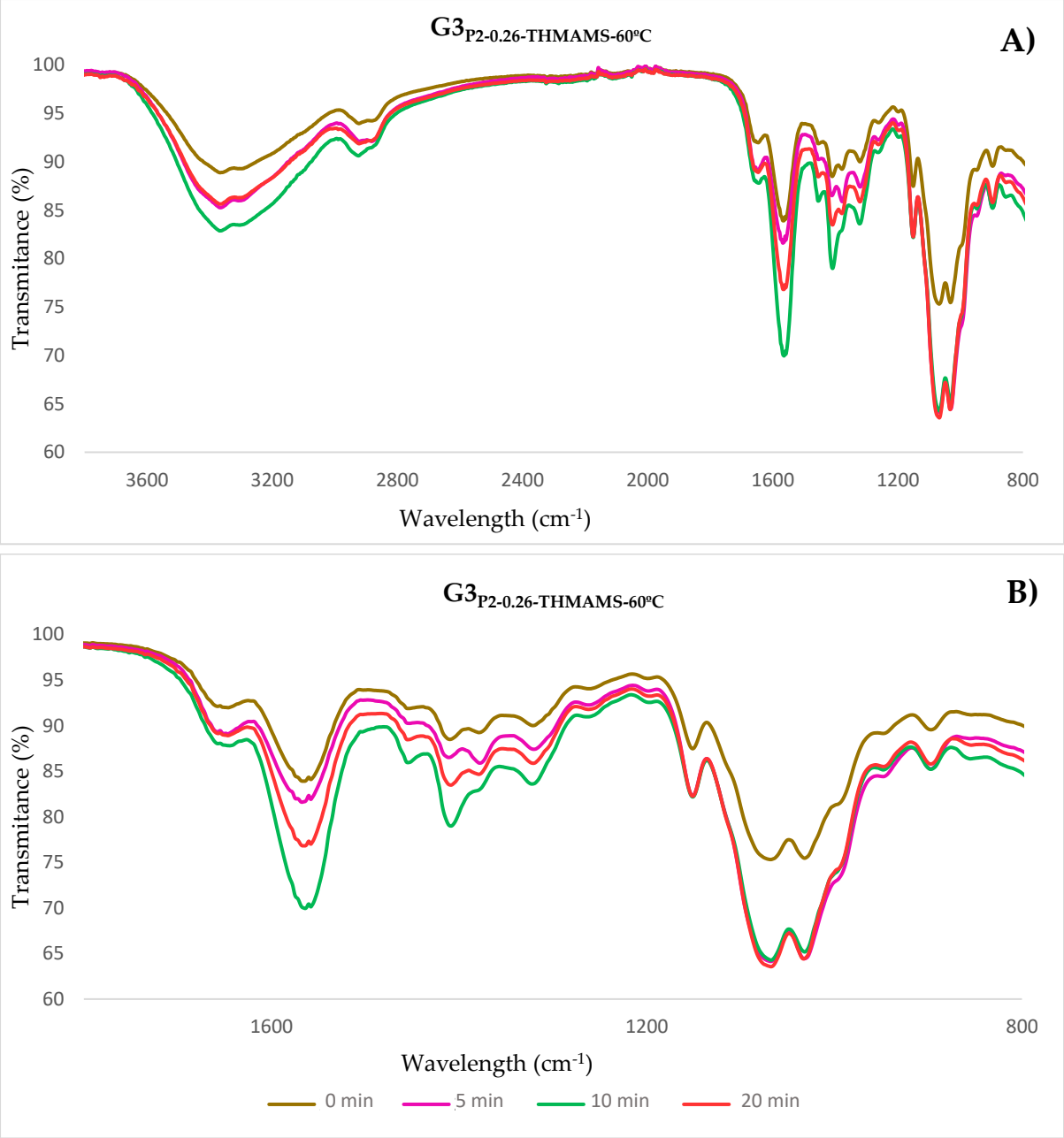

Figure F7 - Experiment $G3_{P2\text{-}0.26\text{-}THMAMS\text{-}60ºC}$ FTIR after 0, 5, 10, and 20 min of CO_2 flux time.
A) 3800-800 cm^{-1} range; B) 1800-800 cm^{-1} range

G – NMR

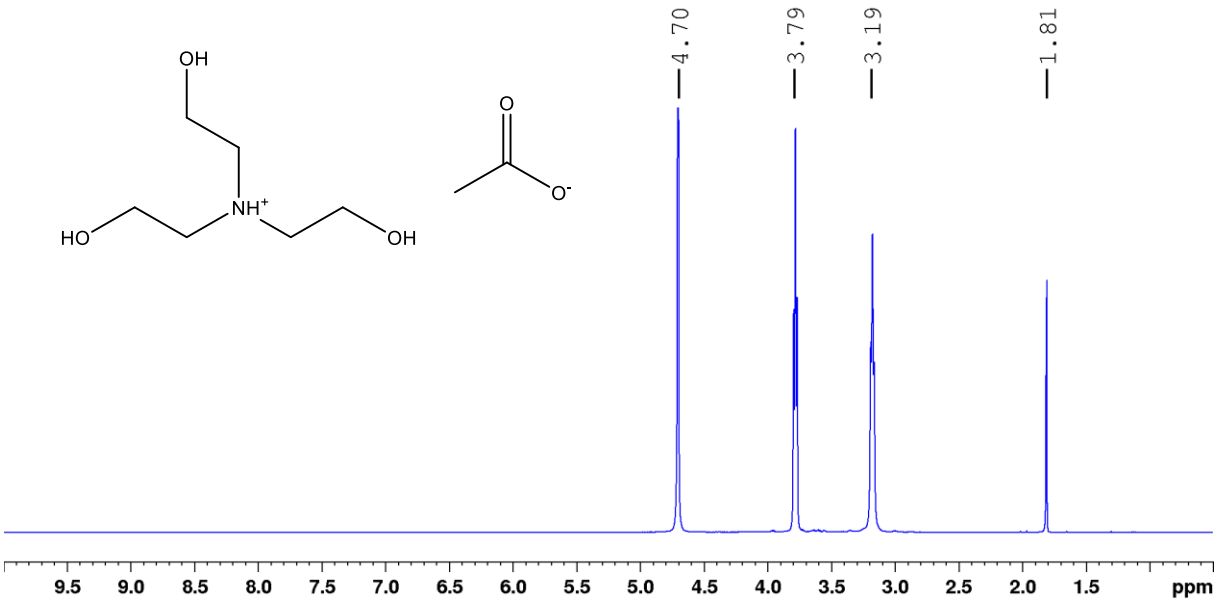

Figure G1 - ^{1}H NMR spectra of TEA.OAc in D_2O

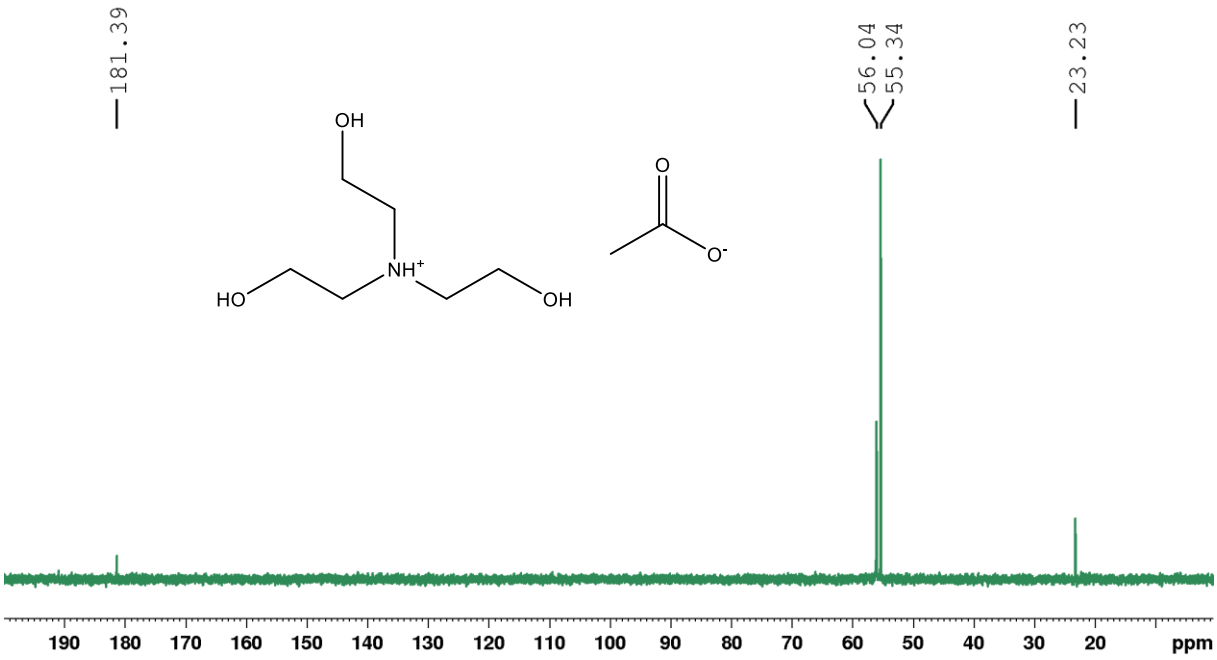

Figure G2 - ^{13}C NMR spectra of TEA.OAc in D_2O

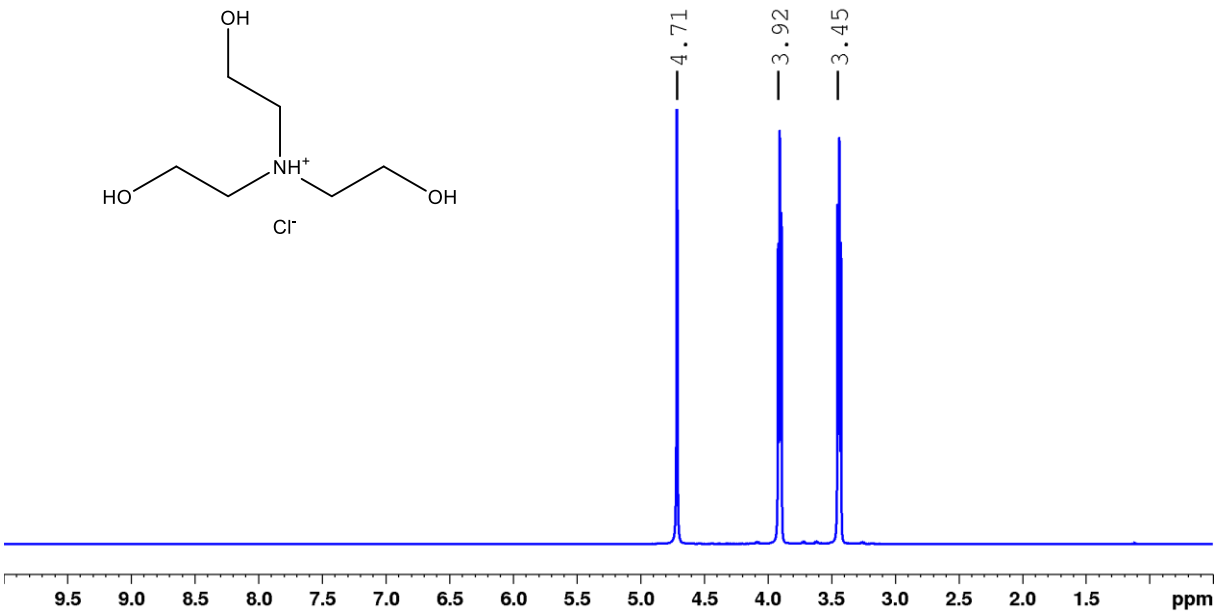

Figure G3 - ^{1}H NMR spectra of TEA.Cl in D_2O

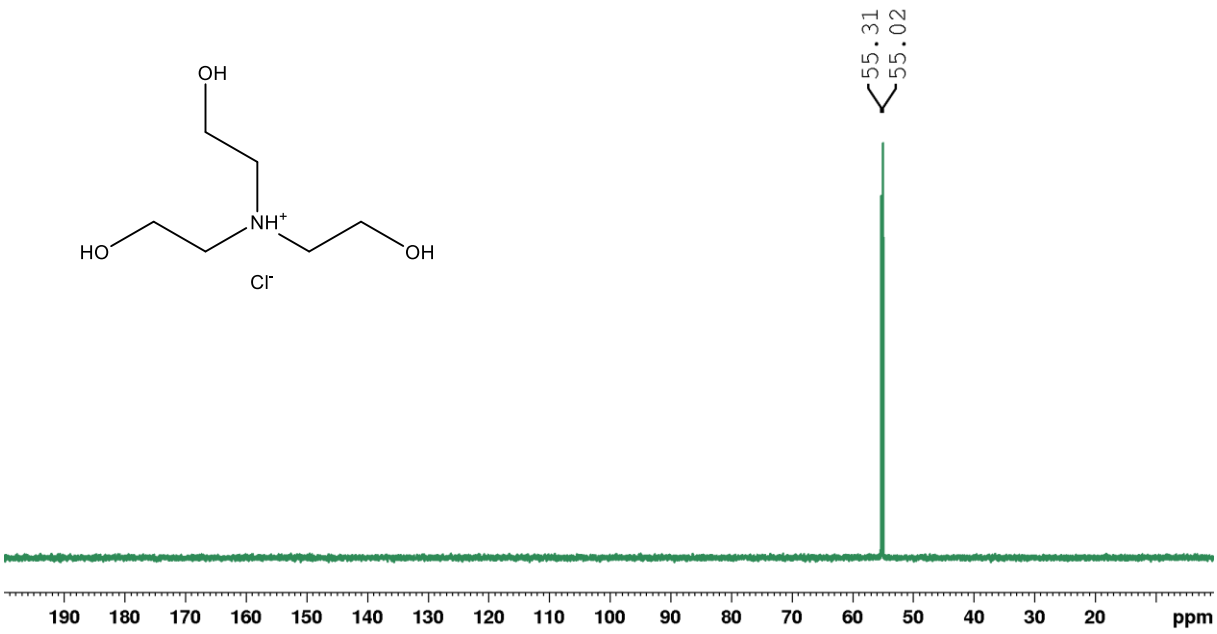

Figure G4 - ^{13}C NMR spectra of TEA.Cl D_2O

H – Catalysis

H.1 - i) T = 80 °C; P = 1 bar; R_{time}= 72h

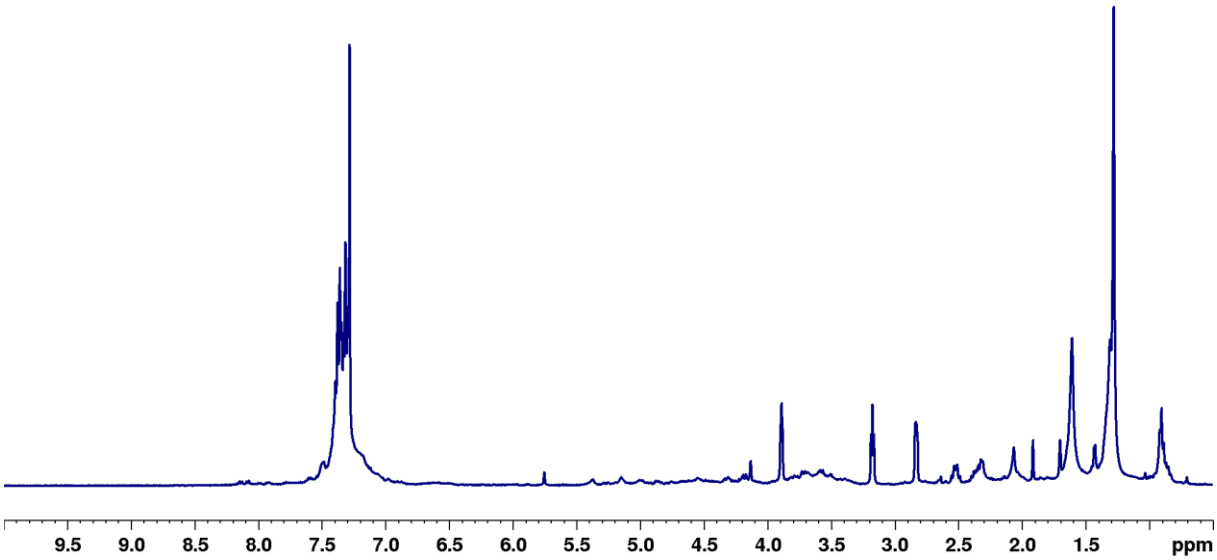

Figure H1.1 - ^{1}H NMR spectra of experiment $G3_{P2\text{-}0.13\text{-}TEA.OAc}$ (entry 24) as catalyst and no co-catalyst, using $CDCl_3$ as solvent

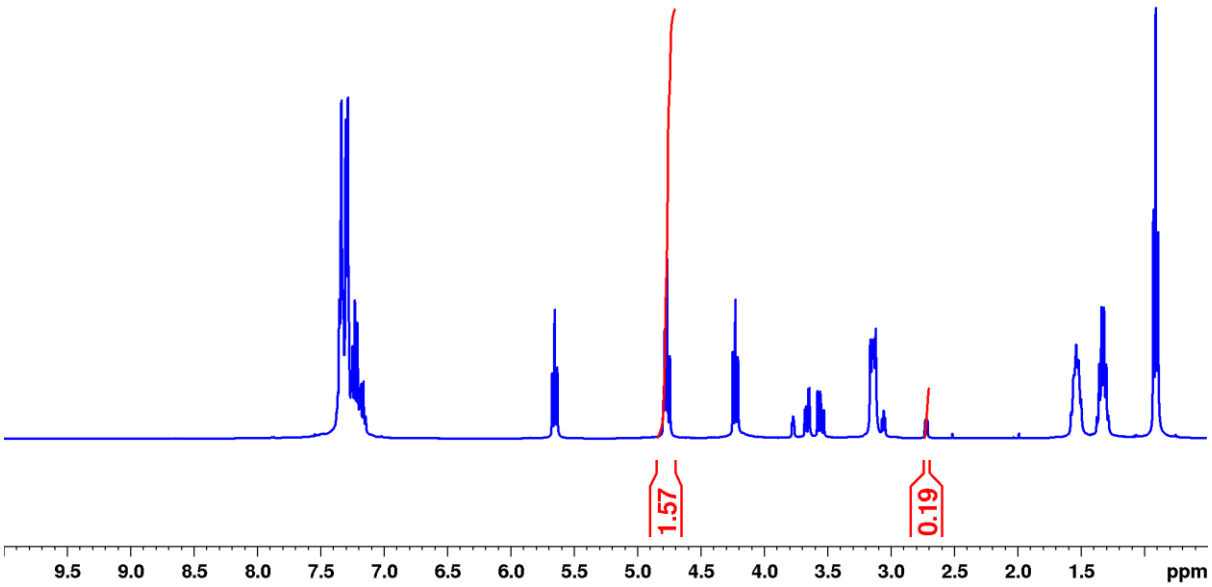

Figure H1.2 - ^{1}H NMR spectra of experiment $G3_{P2\text{-}0.13\text{-}TEA.OAc}$ (entry 24) as catalyst and TBA.Br as co-catalyst, using $CDCl_3$ as solvent

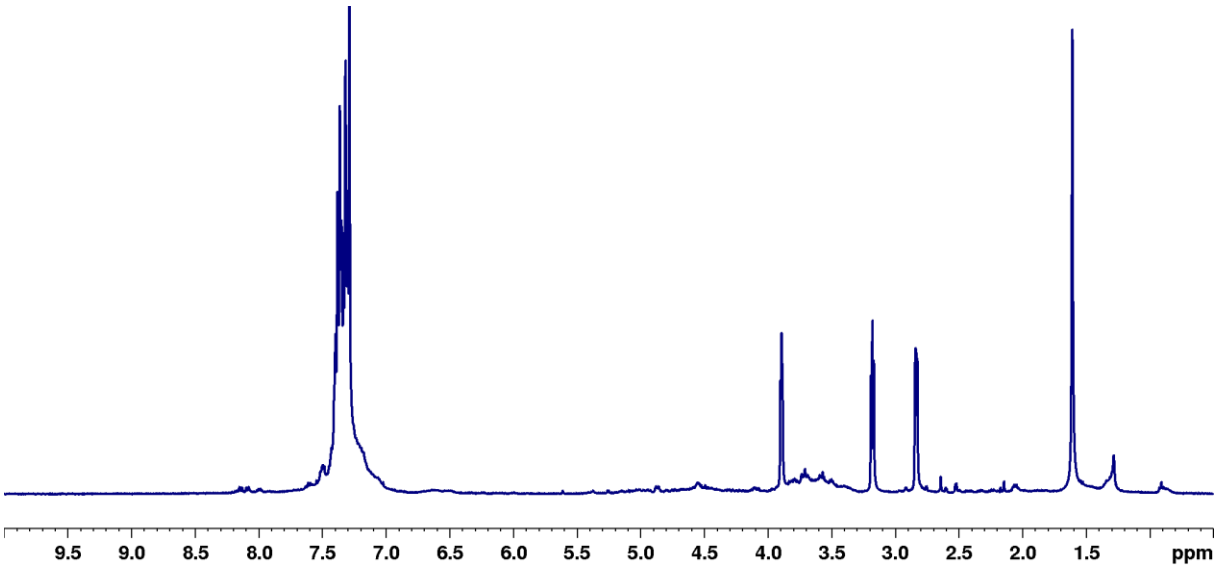

Figure H1.3 - ^{1}H NMR of experiment $G3_{P2\text{-}0.26\text{-}THMAMS}$ (entry 27) as catalyst and no co-catalyst, using $CDCl_3$ as solvent

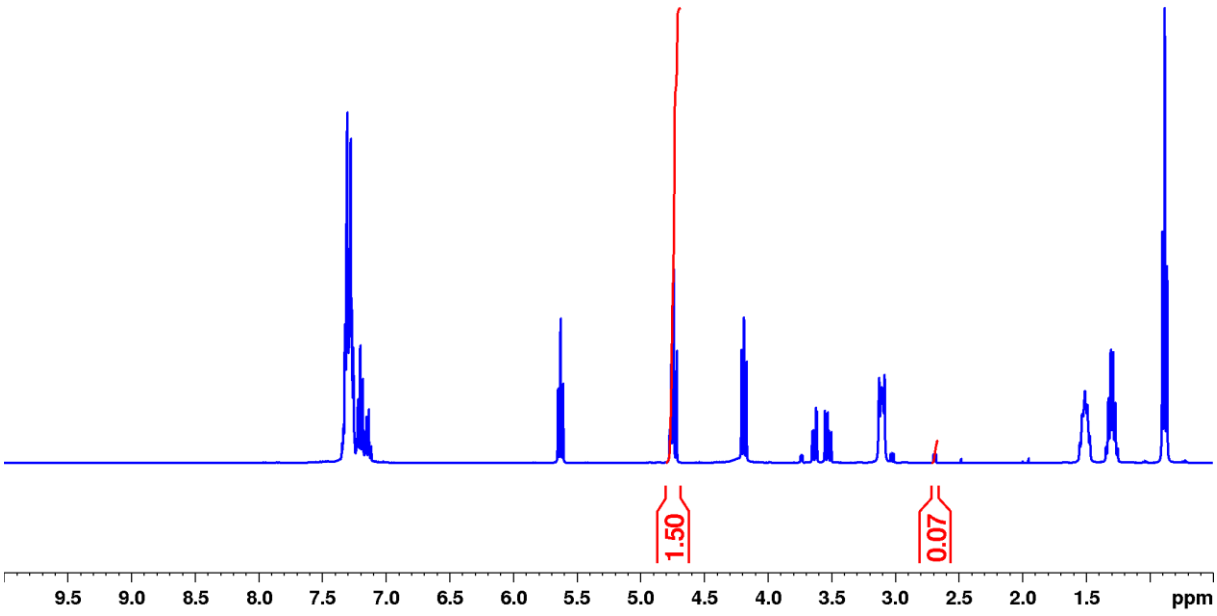

Figure H1.4 - ^{1}H NMR spectra of experiment $G3_{P2\text{-}0.26\text{-}THMAMS}$ (entry 27) as catalyst and TBA.Br as co-catalyst, using $CDCl_3$ as solvent

H.2 - ii) T = 80 °C; P = 5 bar; R_{time}= 4h

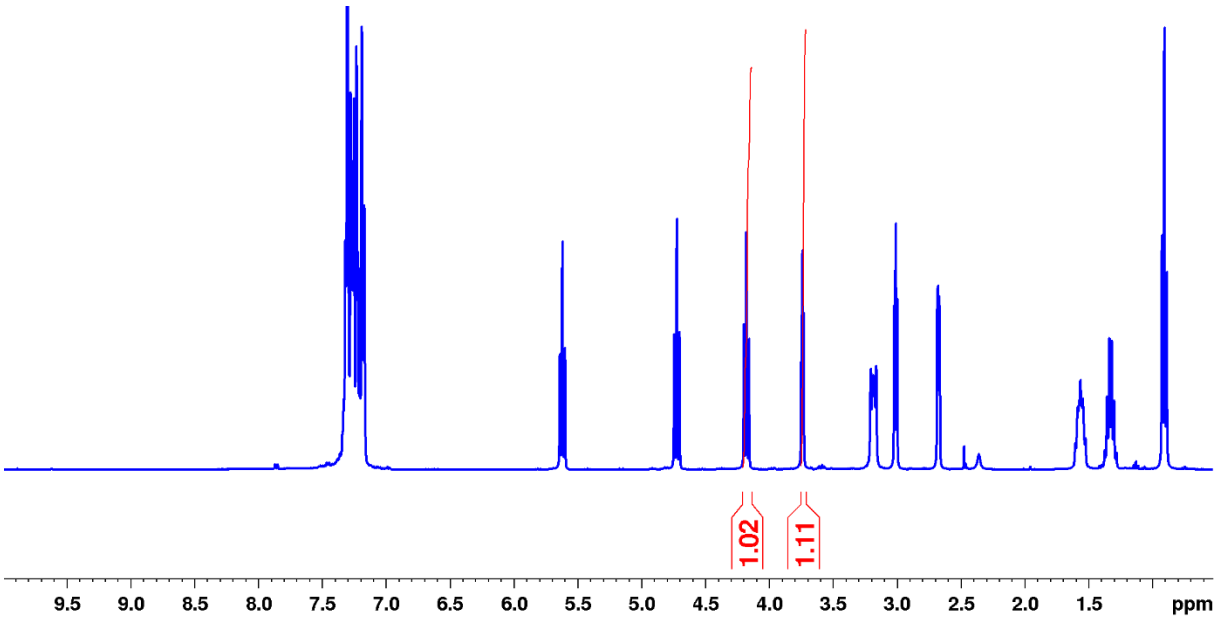

Figure H2.1 - ^{1}H NMR spectra of experiment $G2_{P1\text{-}1.2\text{-}0.1\text{-}Ø\text{-}t.but}$ (entry 21) as catalyst and TBA.Br as co-catalyst, using $CDCl_3$ as solvent

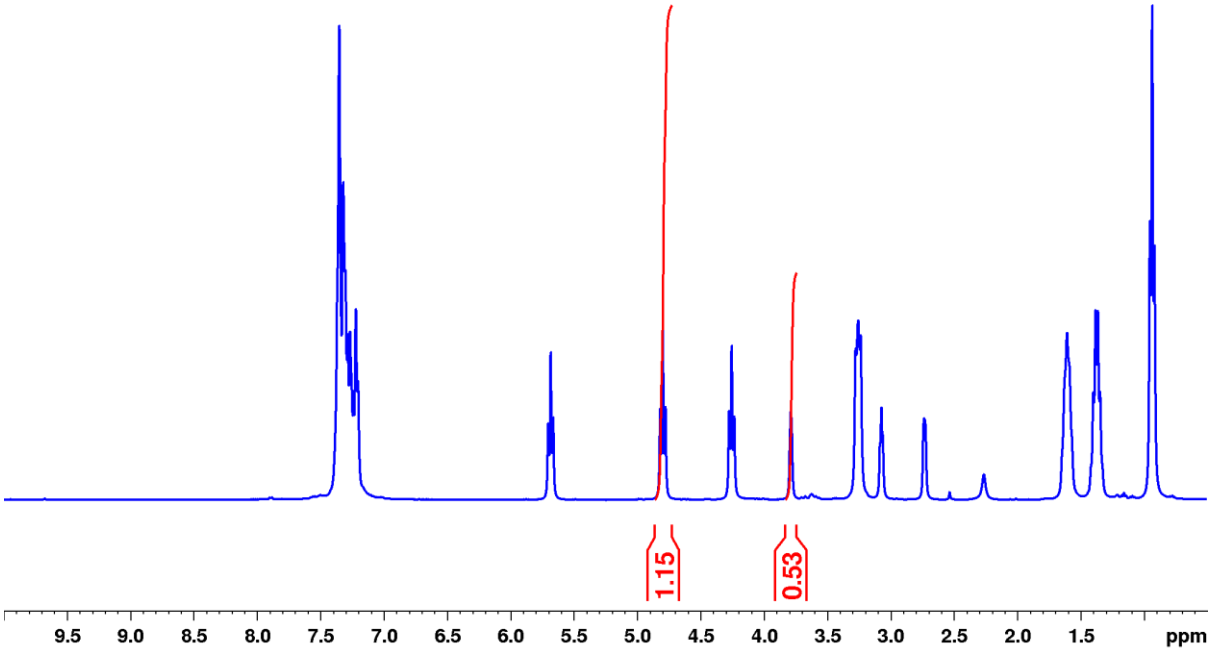

Figure H2.2 - ^{1}H NMR spectra of experiment $G3_{P2\text{-}0.13\text{-}TEA.OAc}$ (entry 24) as catalyst and TBA.Br as co-catalyst, using $CDCl_3$ as solvent

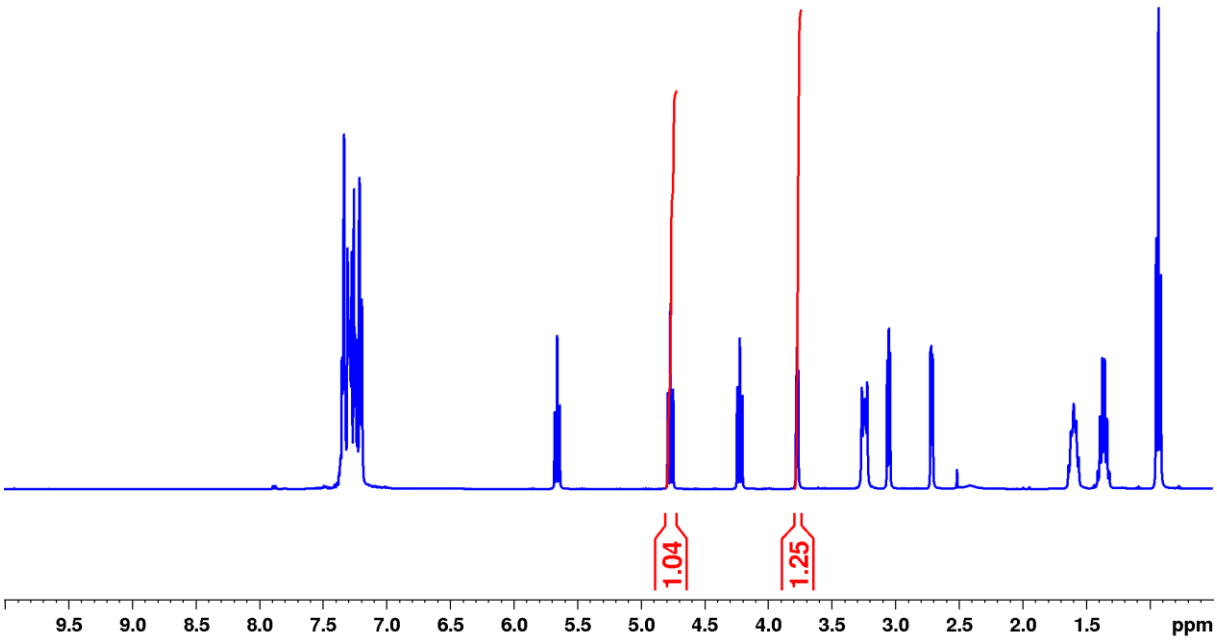

Figure H2.3 - ^{1}H NMR spectra of experiment $G3_{P2\text{-}0.13\text{-}THMAMS}$ (entry 26) as catalyst and TBA.Br as co-catalyst, using $CDCl_3$ as solvent

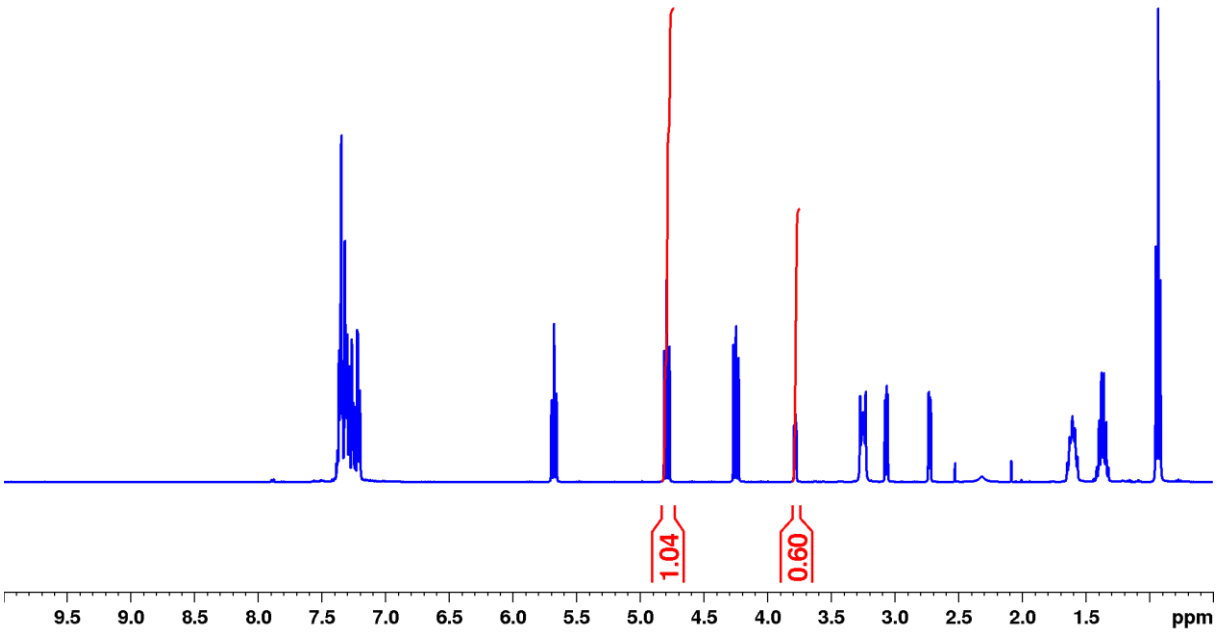

Figure H2.4 - ^{1}H NMR spectra of experiment $G3_{P2\text{-}0.26\text{-}THMAMS}$ (entry 27) as catalyst and TBA.Br as co-catalyst, using $CDCl_3$ as solvent

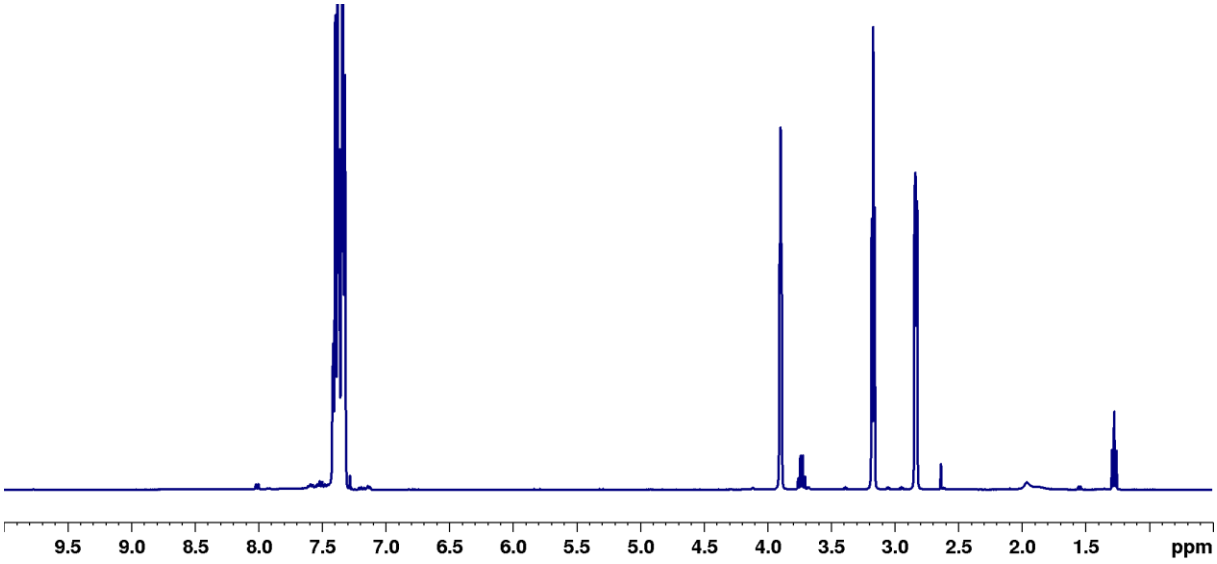

Figure H2.5 - ^{1}H NMR spectra of experiment $G3_{P2\text{-}0.26\text{-}THMAMS}$ (entry 27) as catalyst and no co-catalyst, using $CDCl_3$ as solvent

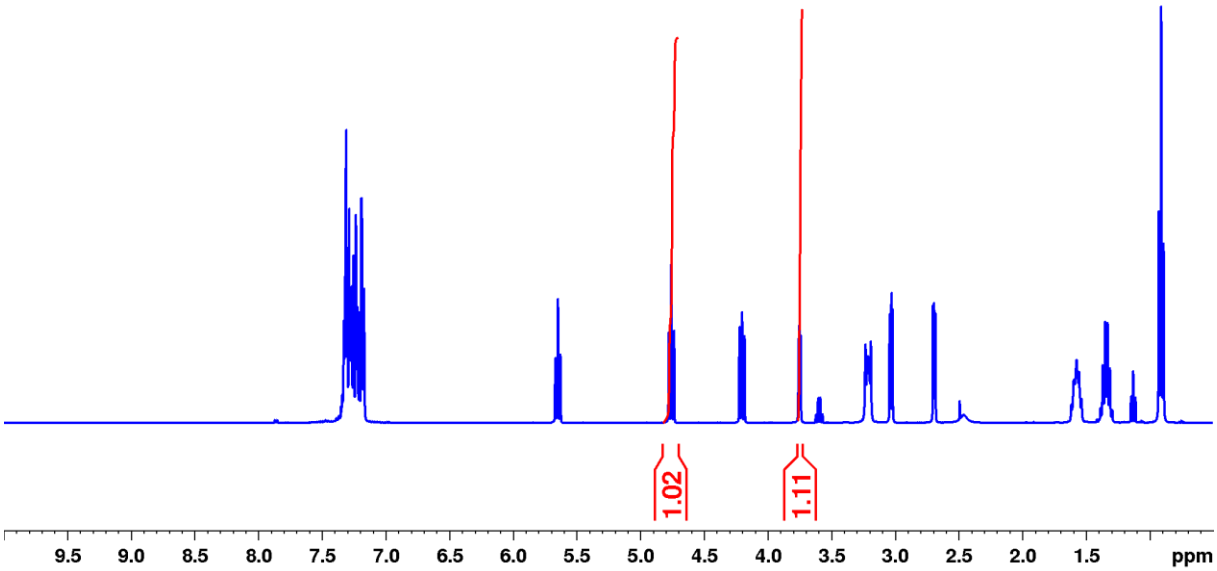

Figure H2.6 - ^{1}H NMR spectra of experiment $G3_{P2\text{-}0.13\text{-}TEA.Cl}$ (entry 28) as catalyst and TBA.Br as co-catalyst, using $CDCl_3$ as solvent

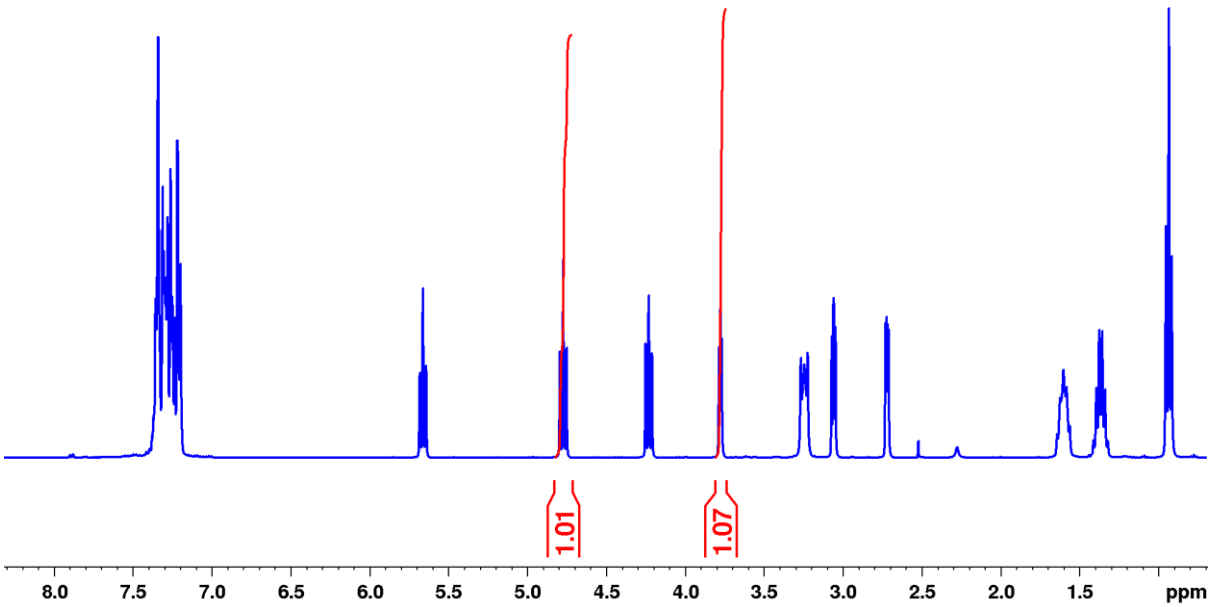

Figure H2.7 - ^{1}H NMR spectra of experiment $G3_{P2\text{-}0.13\text{-}THMAMS\text{-}60^{o}C}$ (entry 30) as catalyst and TBA.Br as co-catalyst, using $CDCl_3$ as solvent

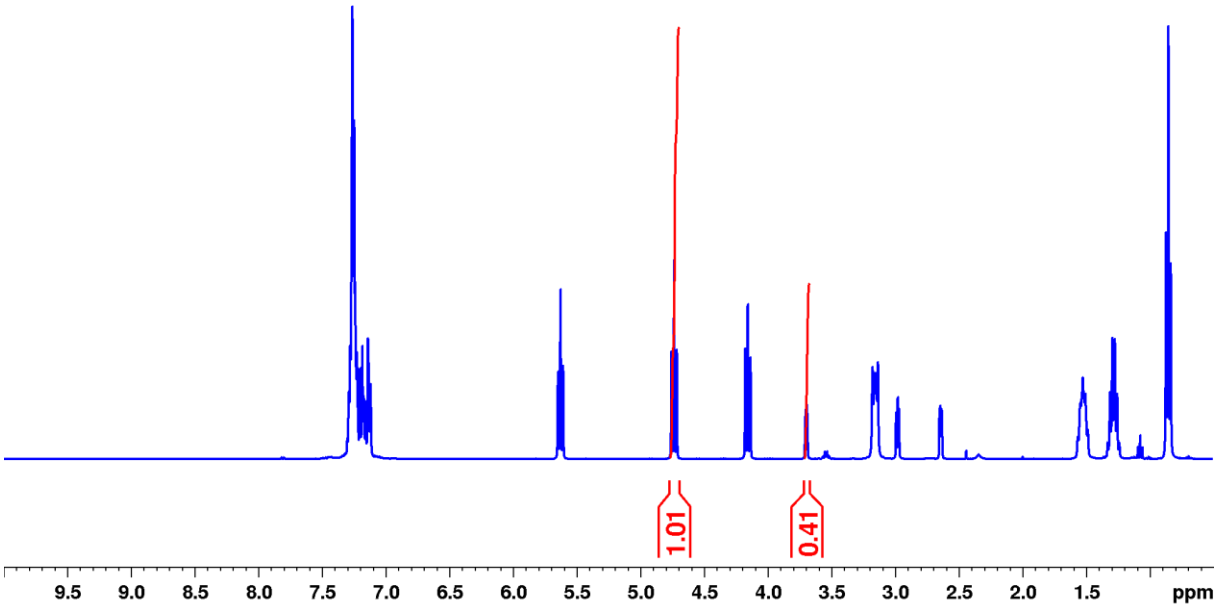

Figure H2.8 - ^{1}H NMR spectra of experiment $G3_{P2\text{-}0.26\text{-}THMAMS\text{-}60^{o}C}$ (entry 31) as catalyst and TBA.Br as co-catalyst, using $CDCl_3$ as solvent

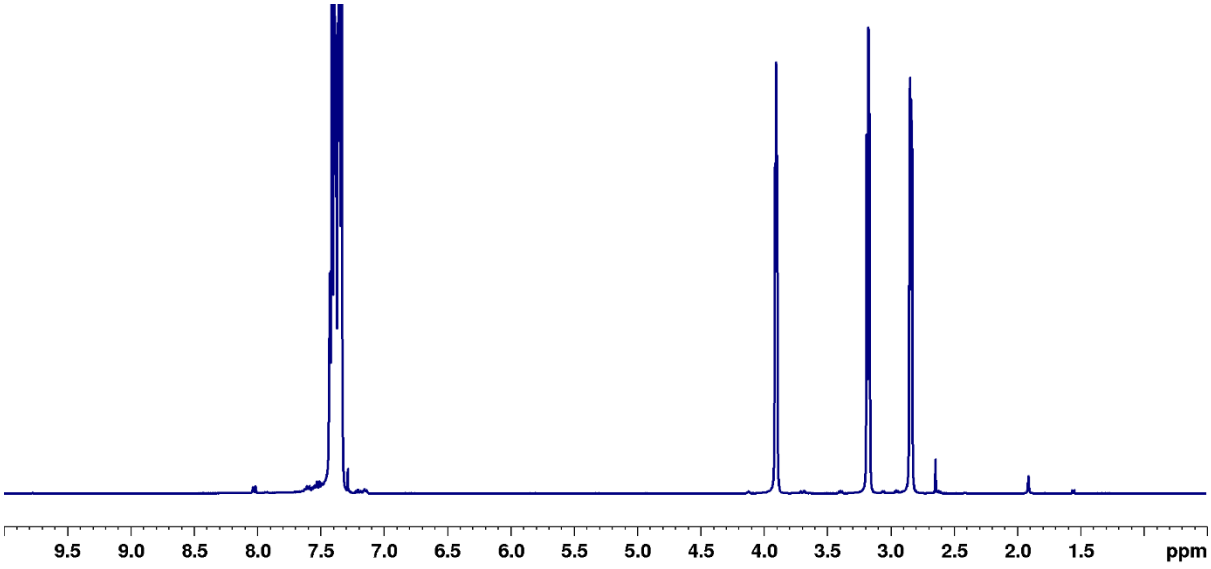

Figure H2.9 - ^{1}H NMR spectra of experiment $G3_{P2\text{-}0.26\text{-}THMAMS\text{-}60^{o}C}$ (entry 31) as catalyst and no co-catalyst, using $CDCl_3$ as solvent

I – Complementary Information of Beads' Characterization

Table I.1 - Batches used for the several characterization tests

Entry	Experiment	SEM	FTIR	BET	CO_2 Capture	Catalysis
1	G1$_{1\text{-}1\text{-}Ø\text{-}0.65}$	Batch 2	Batch 1	Batch 1	----------	----------
2	G1$_{1\text{-}1\text{-}CHI\text{-}0.65}$	Batch 2	Batch 1	Batch 1	----------	----------
3	G2$_{P1\text{-}4\text{-}0\text{-}Ø\text{-}t.but}$	Batch 1	Batch 1	Batch 1	----------	----------
4	G2$_{P1\text{-}1.2\text{-}0\text{-}Ø\text{-}t.but}$	Batch 1	Batch 1	Batch 1	----------	----------
5	G2$_{P1\text{-}1.2\text{-}0.1\text{-}Ø\text{-}t.but}$	Batch 1	Batch 1	Batch 1	----------	----------
6	G3$_{P2\text{-}0.13\text{-}GLU}$	Batch 1	Batch 1	Batch 1	----------	----------
7	G3$_{P2\text{-}0.13\text{-}TEA.OAc}$	Batch 1	Batch 1	Batch 2	Batch 1	Batch 1
8	G3$_{P2\text{-}0.13\text{-}THMAMS}$	Batch 1	Batch 1	Batch 1	Batch 1	Batch 1
9	G3$_{P2\text{-}0.13\text{-}THMAMS\text{-}60ºC}$	Batch 1	Batch 1	Batch 1	Batch 1	Batch 1
10	G3$_{P2\text{-}0.26\text{-}THMAMS}$	Batch 1	Batch 1	Batch 1	Batch 1	Batch 1
11	G3$_{P2\text{-}0.26\text{-}THMAMS\text{-}60ºC}$	Batch 1	Batch 1	Batch 1	Batch 1	Batch 1
12	G3$_{P2\text{-}0.13\text{-}TEA.Cl}$	Batch 1	Batch 1	Batch 1	Batch 1	Batch 1

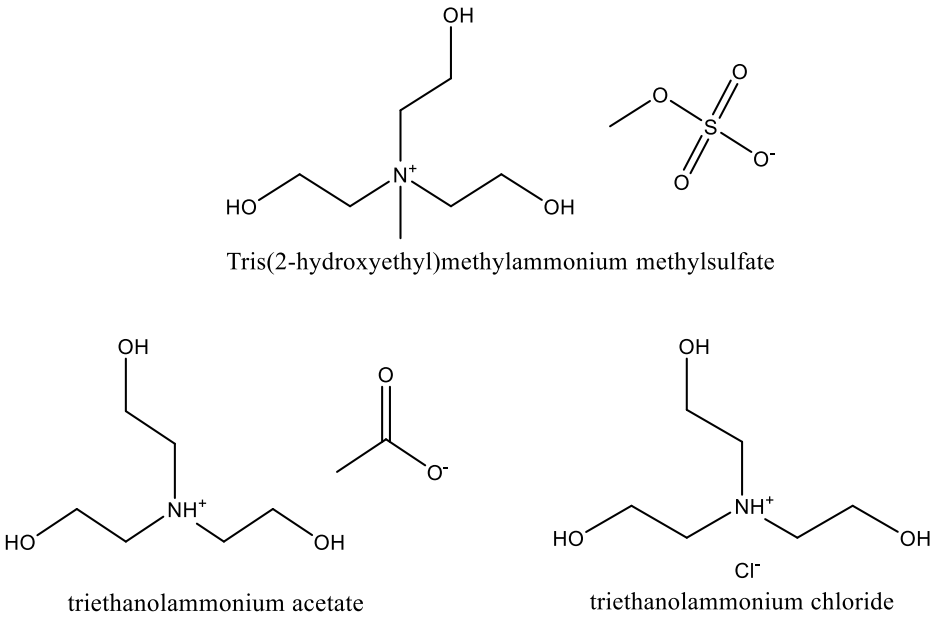

Figure I1 - IL-derivatives used as crosslinkers

2021

DUARTE NUNO BOTELHO DOS SANTOS

DEVELOPMENT OF NEW MATERIALS FOR CO_2 CAPTURE: EVALUATION OF MATERIAL'S MORPHOLOGY